

**Characterization of Regenerator Geometries through Modelling and  
Experimentation**

by

**Kimberley J. Caudle**  
**B.Sc., Queen's University, 1994**

A Thesis Submitted in Partial Fulfillment of the Requirements for the  
Degree of

**MASTER OF APPLIED SCIENCE**


In the Department of Mechanical Engineering

We accept this thesis as conforming to the required standard



---

**Dr. John A. Barclay, Supervisor (Department of Mechanical Engineering)**



---

**Dr. Colin Bradley, Departmental Member (Department of Mechanical Engineering)**



---

**Dr. Maarten Van Emden, Outside Member (Department of Computer Science)**



---

**Dr. Bowie Keefer, External Examiner (Highquest Engineering Inc.)**

© Kimberley J. Caudle, 1997

University of Victoria

All rights reserved. This thesis may not be reproduced in whole or in part, by photocopy  
or other means without the permission of the author.

## Abstract

---

The Cryofuel Systems Group (CFS) is working towards the development of refuelling systems for the distribution of both compressed and liquified natural gas to vehicles. A key component of the refuelling station is the liquefier. CFS has identified magnetic refrigeration as having the potential to provide a high efficiency, low cost liquefier. For an efficient liquefier, a highly effective regenerator is necessary. A regenerator consists of a matrix of porous material that acts as a thermal storage device. Heat is transferred to and from the solid by the fluid in one cycle of operation. Any ineffectiveness in the regenerator seriously impacts the cooling power of the liquefier.

This thesis describes the development of three different regenerator beds constructed using spheres, flakes and wires respectively. A computer model developed to simulate regenerator performance is also discussed. Finally, the details of a differential test apparatus used to characterize the performance of the three regenerators are presented.

---

**Dr. John A. Barclay, Supervisor (Department of Mechanical Engineering)**

---

**Dr. Colin Bradley, Departmental Member (Department of Mechanical Engineering)**

---

**Dr. Martin VanEmden, Outside Member (Department of Computer Science)**

---

**Dr. Bowie Keefer, External Examiner (Highquest Engineering Inc.)**

# Table of Contents

---

Abstract.....	ii
Table of Contents .....	iii
List of Tables .....	viii
List of Figures .....	viii
Nomenclature.....	xiii
Acknowledgements.....	xv
1. Introduction.....	1
1.1 Motivation.....	1
1.2 Objectives.....	4
2. Regenerator Design Theory .....	5
2.1 Thermal Design Methods.....	9
2.1.1 $\epsilon$ -Ntu Method.....	9
2.1.2 $\lambda$ - $\pi$ Method.....	12
2.1.3 2 <sup>nd</sup> Law of Thermodynamics Method .....	14
3. Relevant Porous Media Research.....	17
3.1 Predictions for the Performance of Packed Beds .....	17
3.1.1 Heat Transfer Coefficient.....	19
3.1.2 Pressure Drop .....	21

3.1.3 Longitudinal Conduction.....	23
3.1.3.1 Thermal Conductivity of the Solid Matrix .....	24
3.1.3.2 Fluid Thermal Conductivity including Eddy Diffusivity Effects .....	28
3.2 Correlations for Wire Bundles .....	29
3.2.1 Pressure Drop .....	30
3.2.2 Heat Transfer Coefficient .....	31
3.2.3 Axial Conduction.....	32
4. Regenerator Testing Methods .....	34
4.1 Integral Method .....	34
4.2 Actual Refrigerators .....	35
4.3 Differential Method .....	36
4.3.1 Temperature Change Generation.....	38
4.3.2 Analysis Techniques .....	38
4.3.2.1 Maximum Slope Method.....	39
4.3.2.2 Average Slope Matching Method .....	39
4.3.2.3 Full Curve Matching Method .....	41
5. Regenerator Modeling Program.....	41
5.1 System to be Modelled.....	41
5.1.1 Assumptions .....	42
5.1.2 Input Variables.....	43
5.1.3 Output Variables.....	44
5.2 Solution Techniques .....	44
5.2.1 Discretization of Solid Equation.....	44
5.2.1.1 Fully Implicit Finite Volume Technique.....	45
5.2.2 Discretization of Fluid Equations .....	48
5.2.2.1 Upwind Scheme .....	48
5.3 Model Validation.....	49

6. Experimental Apparatus .....	51
6.1 Regenerator Housing .....	52
6.2 Flow System.....	53
6.3 Temperature Control.....	56
6.4 Instrumentation.....	59
6.4.1 Mass Flow Meter .....	59
6.4.2 Pressure Transducer .....	59
6.4.3 Temperature Sensors.....	60
6.4.4 Data Acquisition System.....	62
6.5 Regenerator Bed Fabrication.....	64
6.5.1 Spheres .....	64
6.5.2 Flakes .....	65
6.5.3 Wires .....	66
7. Test Results: Analysis and Discussion .....	70
7.1 Spherical Particle Bed.....	72
7.1.1 Pressure Drop across Sphere Bed .....	72
7.1.2 Heat Transfer Coefficient in Sphere Bed .....	74
7.1.3 Thermal Conductivity of the Spheres .....	76
7.1.4 Fluid Thermal Conductivity in the Sphere Bed.....	77
7.2 Flake Bed .....	77
7.2.1 Pressure Drop across the Flake Bed.....	77
7.2.2 Heat Transfer Coefficient in the Flake Bed.....	79
7.2.3 Thermal Conductivity of the Flakes.....	79
7.2.4 Fluid Thermal Conductivity in the Flake Bed.....	80
7.3 Wire Bed .....	81
7.3.1 Pressure Drop across the Wire Bed .....	81
7.3.2 Heat Transfer Coefficient in the Wire Bed.....	82

7.3.3 Thermal Conductivity of the Wires .....	83
7.3.4 Fluid Thermal Conductivity in the Wire Bed.....	83
7.4 Comparison of the Performance of the Different Geometries .....	84
8. Conclusions and Recommendations.....	91
8.1 Conclusions .....	91
8.2 Recommendations .....	92
9. References.....	94
Appendix A	
Computer Program to Model Regenerator Thermal Performance .....	100

## List of Tables

---

Table 2.1: Regenerator effectiveness as a function of $C_m$ and $Ntu$ with $C_R=1$ [8] .....	11
Table 2.2: Regenerator effectiveness as a function of $\pi$ and $\lambda$ for a symmetric and balanced regenerator.....	13
Table 3.1: Shape factors for Nonspherical Particles [18].....	18
Table 3.2: Gamson's shape factors for non-spherical particles [19].....	19
Table 4.1: Maximum slope as a function of $Ntu$ and $\lambda$ .....	40
Table 5.1: Comparison of model results with previous works [62].....	50
Table 7.1: Summary of Test Results .....	84

## List of Figures

---

Figure 1.1: Schematic of an LNG/CNG refuelling station.....	2
Figure 1.2: The effect of regenerator performance in a Phillips/Stirling refrigerator.....	3
Figure 2.1: Schematic of counter-flow recuperative heat exchanger.....	5
Figure 2.2: Temperature gradients in an ideal regenerator at steady state .....	6
Figure 2.3: Temperature gradients in a real regenerator at steady state.....	7
Figure 2.4: Energy balance around an element of the solid matrix.....	7
Figure 3.1: Comparison of experimental data with the Ergun equation.....	22
Figure 3.2: Results of effective thermal conduction correlations as a function of porosity .....	27
Figure 3.3: Comparison of effective thermal conductivity correlations.....	28
Figure 3.4: Orientation of wires in regenerator bed .....	30
Figure 4.1: Schematic of integral test method .....	35
Figure 4.2: Schematic of differential test apparatus.....	36
Figure 4.3: Temperature profile in ideal regenerator .....	37

Figure 4.4: Temperature profile in a real regenerator .....	37
Figure 5.1: Nodes and corresponding control volumes along regenerator bed .....	45
Figure 5.2: Heat flux at boundary node.....	47
Figure 6.1: Photograph of completed test apparatus.....	51
Figure 6.2: Process instrumentation diagram.....	52
Figure 6.3: Front and side views of the titanium regenerator housing.....	52
Figure 6.4: The maximum possible flow rate from the pressure regulator at various delivery pressures .....	54
Figure 6.5: cv factor as a function of the number of turns of the metering valve.....	55
Figure 6.6: Schematic of the front and side views of the fast response heater.....	56
Figure 6.7: Heater response time at various mass flow rates.....	58
Figure 6.8: Schematic of data acquisition system.....	62
Figure 6.9: Ball mill for producing metallic flakes.....	65
Figure 6.10: Possible configurations for cross-section of wire bed: a) box wire configuration b) triangle wire configuration.....	67

Figure 6.11: Stainless steel mould for casting plastic tube.....	67
Figure 6.12: Arrangement of wire sections and spacers in wire regenerator bed.....	69
Figure 7.1: Example of heat transfer data analysis .....	71
Figure 7.2: Comparison of experimental results with the Ergun-Macdonald equation for the pressure drop across a bed of stainless steel spheres .....	73
Figure 7.3: Comparison of the Ergun-Macdonald equation with experimental results for the pressure drop across a bed of copper spheres.....	73
Figure 7.4: Comparison of Kays and London correlation [21] with experimental data for stainless steel spheres.....	75
Figure 7.5: Comparison of Kays and London correlation with experimental results for copper spheres.....	76
Figure 7.6: Comparison of the Ergun-Macdonald equation with the experimental results for the pressure drop across a bed of flakes. ....	78
Figure 7.7: Comparison of experimental and theoretical heat transfer coefficient in flake regenerator bed.....	79
Figure 7.8: Thermal conduction in the flake bed .....	80
Figure 7.9: Comparison of theoretical predictions with experimental results for the pressure drop across a bed of wires. ....	81

Figure 7.10: Comparison of theoretical prediction with experimental results for the heat transfer coefficient in a wire bed .....	82
Figure 7.11: Comparison of the pressure drop across different geometries .....	85
Figure 7.12: Comparison of the pressure drop across different geometries the surface area set to $1.5 \text{ m}^2$ .....	86
Figure 7.13: Comparison of the pressure drop across different geometries with a surface area of $1.5 \text{ m}^2$ and a porosity of 0.355 .....	87
Figure 7.14: Comparison of the heat transfer coefficient measured in the different geometries .....	88
Figure 7.15: Comparison of the predicted heat transfer coefficient in the different beds with a surface area of $1.5 \text{ m}^2$ .....	88
Figure 7.16: Comparison of the Ntu predicted if all the geometries had a surface area of $1.5 \text{ m}^2$ .....	89
Figure 7.17: Comparison of the fluid and solid conductivity for the different geometries .....	90

## Nomenclature

---

$A_c$	cross-sectional area ( $m^2$ )
$A_s$	surface area ( $m^2$ )
$C$	capacity rate (W/K)
$C_m$	matrix capacity rate (W/K)
$C_R$	capacity rate ratio
$c_p$	specific heat (J/kgK)
$D$	diameter (m), mass diffusivity ( $m^2/s$ )
$D_h$	hydraulic diameter (m)
$f$	friction factor
$G$	mass flow per unit area ( $kg/m^2s$ )
$h$	convective heat transfer coefficient ( $W/m^2K$ )
$j$	Colburn j number
$k$	thermal conductivity (W/mK)
$L$	length (m)
$m$	mass (kg)
$\dot{m}$	mass flow rate (kg/s)
$N$	number of sections in wire bed
$N_{tu}$	number of heat transfer units
$Nu$	Nusselt number
$P$	period (s), pressure (kPa)
$\Delta P$	pressure difference (kPa)
$Pe$	Peclet number
$Pr$	Prandtl number
$\dot{Q}$	heat transfer (W)
$Re$	Reynolds number
$S$	source term

$\dot{S}$	rate of entropy production (W/K)
$s$	spacing between sections in wire bed (m)
$T$	temperature (K)
$t$	time (s), section thickness in wire bed
$\Delta t$	time step (s)
$u$	velocity (m/s)
$V$	volume (m <sup>3</sup> )
$v$	velocity (m/s)
$v_o$	superficial velocity (m/s)
$\dot{W}$	work (W)
$\Delta x$	increment of length (m)

#### Subscripts

$c$	cold
$e$	east, effective
$eq$	equivalent
$f$	fluid
$h$	hot
$in$	inlet
$m$	mean
$out$	outlet
$p$	particle
$s$	solid
$w$	wire

#### Greek Symbols

$\alpha$	porosity
$\varepsilon$	regenerator effectiveness
$\phi_s$	shape factor

$\varphi$	thermal diffusivity ( $\text{m}^2/\text{s}$ )
$\lambda$	reduced length, ratio of fluid to solid thermal conductivity
$\mu$	fluid viscosity ( $\text{Pa}\cdot\text{s}$ )
$\pi$	reduced period
$\rho$	density ( $\text{kg}/\text{m}^3$ )

## Acknowledgements

---

I would like to thank my supervisor, Dr. John Barclay for his help, support and encouragement over the course of my thesis. He created and continues to encourage an atmosphere that makes for an enjoyable working environment. I would also like to thank all of the IESVic staff and students, both past and present, for their friendship and support. They have made this experience much more than just a few more years of school. A special thank-you goes to Frank Havig for all his help and patience in the lab and for always being up for a good debate.

Thank-you to my family and friends for their constant love and tolerance, especially to my parents for always encouraging the belief that I could be anything I wanted.

I am grateful to the Natural Sciences and Engineering Research Council of Canada, Centra Gas Inc. and Natural Resources, Canada for the financial support that made this work possible.

# 1. Introduction

---

## 1.1 Motivation

The Institute for Integrated Energy Systems at the University of Victoria (IESVic) recognizes the need for new energy systems that meet all of the following criteria:

- offer a foundation for economic growth and industrial diversification,
- cause minimal environmental intrusion, and especially, reduce climate destabilizing emissions,
- provide flexibility and resilience in response to technical, geopolitical and environmental change [1].

To fill this need IESVic groups are working towards increasing the use of natural gas (NG) as a low emission vehicle fuel and, ultimately, introducing hydrogen as a zero emission vehicle fuel. The major barrier to the widespread use of natural gas as a vehicle fuel is economics [2]. The environmental impact alone will not be sufficient to drive a switch to natural gas from conventional fuels such as gasoline and diesel. It must also be competitive in terms of both performance and economics. The Cryofuel Systems Group (CFS), one of the three IESVic groups, has chosen to concentrate its research efforts in the development of fleet-sized refuelling systems for the distribution of both compressed natural gas (CNG) and liquefied natural gas (LNG).

One of the problems in matching the performance of gasoline and diesel with natural gas for vehicular applications is onboard storage. Because it exists as a gas at standard temperature and pressure (STP), the energy density of natural gas is lower than that of gasoline or diesel fuel. Therefore, it must be stored as either CNG or LNG to provide a comparable range. For CNG, the gas is compressed to approximately 20 MPa (3000 psig) but the energy density is still 4.3 times lower than that of diesel. By liquefying the

gas and storing it as LNG, the energy density can be increased by a factor of 2.5 over CNG (1.7 times less than diesel). With its shorter range, CNG is practical for use in light-duty vehicles that consume a low amount of fuel. The higher energy density of LNG makes it more practical for medium to heavy-duty vehicles. CFS has developed a design for a refuelling station, shown in Figure 1.1, to provide both CNG and LNG.

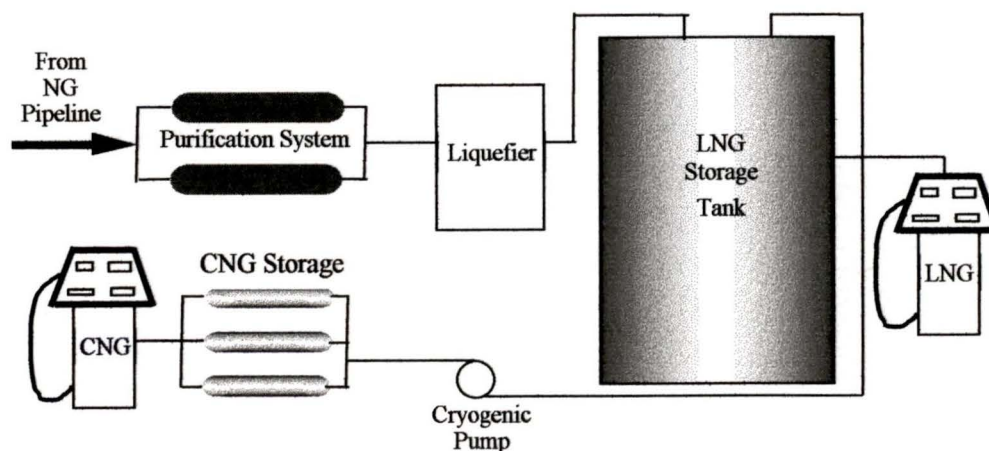


**Figure 1.1: Schematic of an LNG/CNG refuelling station**

The natural gas is supplied through an existing pipeline. On arrival at the refuelling station, the NG is first purified and then liquefied. It can then be dispensed as LNG or passed through a cryogenic pump and provided to the user as CNG.

There are many benefits to liquefying on site using existing NG pipelines rather than trucking in LNG [3]. However, about 30% of the capital cost for the refuelling station comes in the liquefier. It is necessary to have a liquefier with low capital and operating costs for the refuelling station to be economically viable. After researching several liquefying technologies, CFS identified magnetic refrigeration as having the potential to provide a high efficiency, low cost liquefier [4][5].

The principle behind magnetic refrigeration is the magnetocaloric effect (MCE). This effect causes certain materials to heat up upon the adiabatic application of a magnetic

field and to cool down again when the field is removed. The MCE is combined with a regenerative cycle to span the large temperature difference from room temperature to 112K; the temperature needed to liquefy NG at 101.3 kPa. For more information on the magnetocaloric effect and magnetic refrigeration, see references [6][7] and references therein.

A key component of the magnetic liquefier is the regenerator. This is also true for a number of other refrigeration/liquefaction cycles such as Phillips/Stirling, Gifford-McMahon and Orifice Pulse Tube. For more information on regenerative refrigeration cycles, see references [8] and [24]. A regenerator consists of a matrix of porous material that acts as a thermal storage device. Heat is transferred to and from the solid by the fluid in one cycle of operation. Any ineffectiveness in the regenerator seriously impacts the cooling power of the liquefier. If the fluid in a refrigeration cycle leaves the regenerator at a higher temperature than the ideal, some of the energy that could have been absorbed from the low temperature source is wasted in cooling the heat transfer fluid.

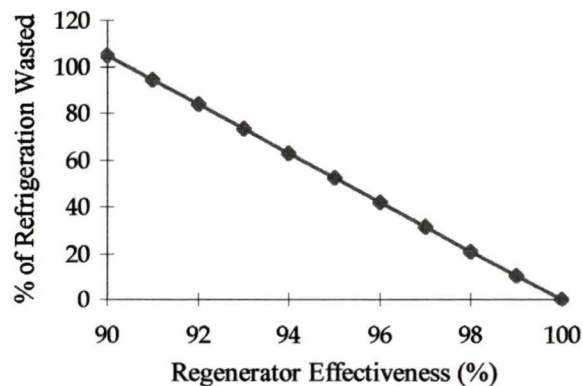


**Figure 1.2: The effect of regenerator performance in a Phillips/Stirling refrigerator**

Figure 1.2 shows the amount of refrigeration which is lost due to regenerator ineffectiveness in a Phillips/Stirling refrigerator working between 300 and 78 K [8].

Note that a 90% effective regenerator results in a 100% loss of refrigeration. The different methods for calculating regenerator effectiveness are discussed in detail in Chapter 2.

One of the research goals of CFS is to improve regenerator performance. The geometry chosen for the regenerator matrix plays a key role in the amount of heat transfer achieved as well as in the overall effectiveness of the regenerator. This role will be discussed further in Chapter 2. Some of the different geometries which have been examined in previous work are wire screens [9][10][11], spherical particles, perforated plates [12][13], and wire mesh [14]. CFS has identified a number of other geometries as having the potential to make highly effective regenerator beds.

## **1.2 Objectives**

The objective of this thesis was to build, test, and model several regenerator geometries to characterize and compare their performance. The evaluation not only examined the heat transfer achieved in the bed but also included the effects of longitudinal conduction and pressure drop on the regenerator effectiveness.

Three different geometries were investigated.

- spherical particles,
- wires, and
- flakes

## 2. Regenerator Design Theory

---

Heat exchangers can be divided into two categories: recuperative or regenerative. Recuperative heat exchangers are the more commonly known type, consisting of two or more steady flow fluid streams. An example of a recuperative heat exchanger is shown in Figure 2.1

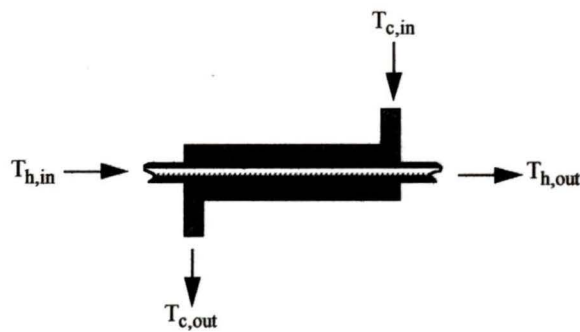


**Figure 2.1: Schematic of counter-flow recuperative heat exchanger**

Heat is transferred from the hot to cold stream usually through a conducting wall. There are many different configurations that are discussed in detail in references [8] and [15].

Regenerative heat exchangers differ from recuperative heat exchangers in two main ways. First, regenerators consist of a bed of porous material through which the heat transfer fluid flows. Second, regenerators operate in a periodic, not steady, manner. As a hot fluid flows through the porous solid of the regenerator bed, heat is transferred from the fluid to the solid. This heat is stored in the solid until the flow is reversed and the heat transferred back to the fluid. These two heat transfer stages are referred to as the hot blow and cold blow respectively.

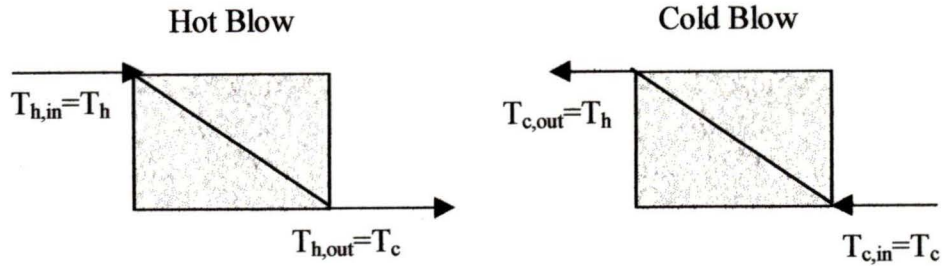


**Figure 2.2: Temperature gradients in an ideal regenerator at steady state**

In the hot blow of the ideal case (Figure 2.2), fluid enters the regenerator at  $T_h$  and is cooled by the solid matrix to  $T_c$ . In the cold blow, the fluid enters the cold end of the regenerator at  $T_c$ , is warmed by the solid matrix, and exits at  $T_h$ . The temperature gradient of the solid matrix remains constant throughout this process. The requirements necessary for an ideal regenerator are:

- zero longitudinal conduction,
- zero pressure drop,
- infinite thermal mass, and
- infinite heat transfer area.

In a real regenerator, longitudinal conduction, pressure drop, finite thermal mass, and finite heat transfer are all unavoidable and will adversely affect the regenerator performance.

Figure 2.3 shows that during the hot blow of a real regenerator the fluid enters at  $T_h$  and is cooled by the solid matrix. Due to finite heat transfer between the fluid and the solid, the fluid exits the bed at a temperature slightly higher than  $T_c$ . This temperature difference is denoted as  $\Delta T_{f,c}$ . Also, because the thermal mass of the solid matrix is finite, the average bed temperature will rise slightly. This temperature increase is denoted by  $\Delta T_{s,h}$ . Similarly, in the cold blow, the fluid enters at  $T_c$  but exits the bed at a temperature slightly less than  $T_h$  and the temperature of the solid decreases by  $\Delta T_{s,c}$ . In a balanced and symmetrical regenerator with identical heat transfer rates and blow times

and constant heat capacities,  $\Delta T_{s,h} = \Delta T_{s,c}$ . Therefore the temperature gradient of the solid matrix will be the same at the start of each cycle.

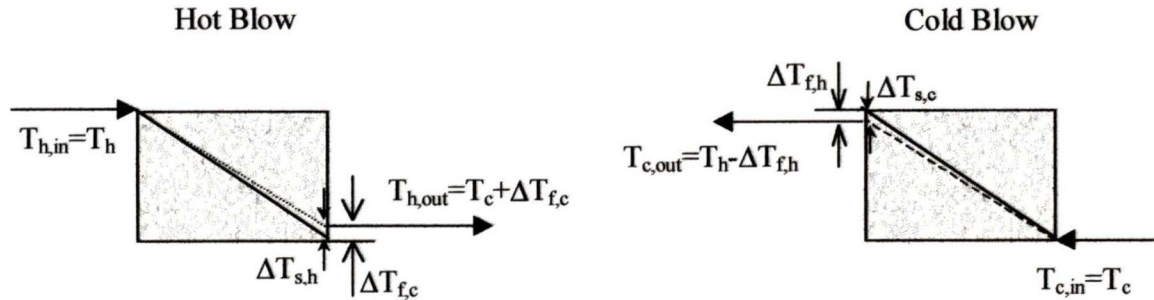


**Figure 2.3: Temperature gradients in a real regenerator at steady state**

Due to the periodic nature of regenerators, the temperature at any location along the bed is time dependent. This requires a more complicated analysis than is necessary for a steady-flow recuperative device. First, consider the first-law energy balance on a differential element of the solid undergoing a hot blow, as illustrated in Figure 2.4.

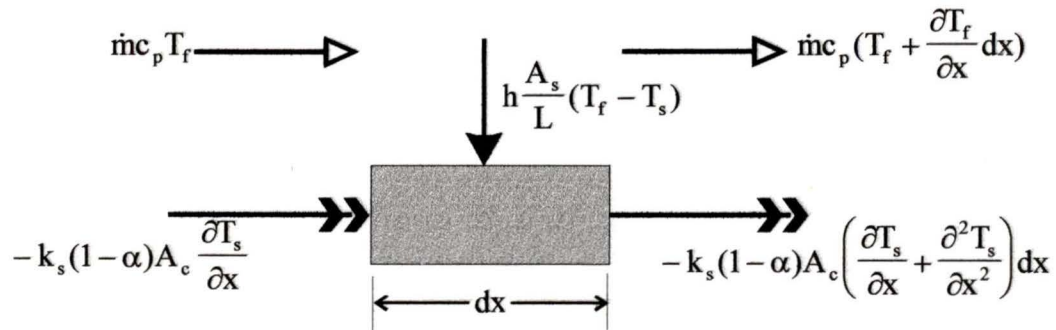


**Figure 2.4: Energy balance around an element of the solid matrix**

The energy transfer mechanisms are as follows:

- Energy absorbed by the solid:  $\left(\frac{m_s}{L}\right) c_{ps} \left(\frac{\partial T_s}{\partial t}\right) dx$  (2.1)

where  $m_s$  is the mass of the solid,  $c_{ps}$  is the specific heat of the solid and  $L$  is the length of the regenerator bed.

- Heat transferred to the solid by convection:  $h\left(\frac{A_s}{L}\right)(T_f - T_s)dx$  (2.1a)

where  $h$  is the heat transfer coefficient between the fluid and the solid and  $A_s$  is the surface area of the solid matrix.

- Energy transferred from the fluid:  $\dot{m}c_{pf}\left(\frac{\partial T_f}{\partial x}\right)dx$  (2.1b)

where  $\dot{m}$  is the mass flow rate of the fluid.

- Heat transferred through the solid by conduction:  $k_s(1-\alpha)A_c\left(\frac{\partial^2 T_s}{\partial x^2}\right)dx$  (2.1c)

where  $k_s$  is the thermal conductivity of the solid,  $A_c$  is the cross-sectional area of the regenerator container and  $\alpha$  is the porosity.

- Heat transferred through the fluid by conduction:  $k_f\alpha A_c\left(\frac{\partial^2 T_f}{\partial x^2}\right)dx$  (2.1d)

where  $k_f$  is the thermal conductivity of the fluid.

Therefore, an energy balance for the fluid gives:

$$\dot{m}_f c_{pf} \left( \frac{\partial T_f}{\partial x} \right) dx = h \frac{A_s}{L} (T_s - T_f) dx + k_f \alpha A_c \left( \frac{\partial^2 T_f}{\partial x^2} \right) dx \quad (2.2)$$

And for the solid:

$$\frac{\dot{m}_s}{L} c_{ps} \left( \frac{\partial T_s}{\partial t} \right) dx = h \frac{A_s}{L} (T_f - T_s) dx + k_s (1 - \alpha) A_c \left( \frac{\partial^2 T_s}{\partial x^2} \right) dx \quad (2.3)$$

Once the energy transfer mechanisms are known, there are a number of methods that are used to determine the regenerator effectiveness and help in the design process. Several of these are described in the next section.

## 2.1 Thermal Design Methods

### 2.1.1 $\epsilon$ -Ntu Method

This method was developed by Coppage and London [16] in 1953.

The regenerator effectiveness is defined as:

$$\epsilon = \frac{\dot{Q}}{\dot{Q}_{\max}} = \frac{\text{actual heat transfer}}{\text{maximum possible heat transfer}} \quad (2.4)$$

In the ideal case,  $T_{c,\text{out}} = T_{h,\text{in}}$  and  $T_{h,\text{out}} = T_{c,\text{in}}$ , as was shown in Figure 2.2. Therefore, the maximum possible temperature change for the fluid is  $(T_{h,\text{in}} - T_{c,\text{in}})$ . This temperature change will occur in the fluid with the minimum capacity rate ( $C_{\min} = \dot{m}c_p$ ).

The maximum possible heat transfer is:

$$\dot{Q}_{\max} = C_{\min} (T_{h,\text{in}} - T_{c,\text{in}}), \quad (2.5)$$

and the effectiveness can now be written as:

$$\epsilon = \frac{\dot{Q}}{C_{\min} (T_{h,\text{in}} - T_{c,\text{in}})} \quad (2.6)$$

where  $\dot{Q}$  = the average heat transfer rate in the regenerator.

The number of heat transfer units, Ntu, is a measure of the heat transfer in the bed and is defined as:

$$Ntu = \frac{hA_s}{C_{\min}} \quad (2.7)$$

In the case of a regenerator this can be rewritten as:

$$Ntu = \frac{1}{C_{\min}} \left( \frac{1}{h_h A_{s,h}} + \frac{1}{h_c A_{s,c}} \right)^{-1} \quad (2.7a)$$

For a regenerator  $A_{s,h} = A_{s,c}$  because the same bed is used for the heating and cooling portions of the cycle.

The ratio of the capacity rates is given as:

$$C_R = \frac{C_{\min}}{C_{\max}} = \frac{(\dot{m}c_p)_{\min}}{(\dot{m}c_p)_{\max}} \quad (2.8)$$

For a balanced regenerator,  $C_R=1$ .

Up to this point the analysis has been similar to that of a recuperative heat exchanger [8] [21]. To fully characterize a regenerator, an additional term, the matrix capacity rate, is necessary.

$$C_m = \frac{m_s c_{ps}}{P_o C_{\min}} \quad (2.9)$$

where  $P_o = P_c + P_h$ ; the total period of the regenerator.

Values for the regenerator effectiveness as a function of  $C_m$  and  $Ntu$  for  $C_R=1$  have been determined by Kays and London [21] and are given in Table 2.1.

**Table 2.1: Regenerator effectiveness as a function of  $C_m$  and  $Ntu$  with  $C_R=1$  [8]**

$N_{tu,0}$	Matrix Capacity Rate Ratio, $C_m$							
	0.8	1.0	1.25	1.5	2.0	3.0	5.0	$\infty$
0	0	0	0	0	0	0	0	0
0.5	0.315	0.322	0.326	0.328	0.330	0.332	0.333	0.3333
1.0	0.449	0.467	0.478	0.485	0.491	0.496	0.499	0.5000
1.5	0.521	0.548	0.566	0.576	0.586	0.594	0.598	0.6000
2.0	0.566	0.601	0.623	0.636	0.649	0.659	0.664	0.6667
2.5	0.599	0.639	0.664	0.679	0.694	0.705	0.711	0.7143
3.0	0.622	0.667	0.696	0.712	0.728	0.740	0.746	0.7500
3.5	0.642	0.690	0.721	0.738	0.755	0.767	0.774	0.7778
4.0	0.659	0.709	0.741	0.759	0.776	0.789	0.796	0.8000
4.5	0.673	0.724	0.758	0.776	0.794	0.807	0.814	0.8182
5.0	0.685	0.738	0.772	0.791	0.809	0.822	0.829	0.8333
5.5	0.696	0.749	0.785	0.803	0.821	0.834	0.842	0.8462
6.0	0.705	0.759	0.796	0.814	0.832	0.845	0.853	0.8571
6.5	0.713	0.768	0.805	0.824	0.842	0.855	0.862	0.8667
7.0	0.721	0.776	0.814	0.833	0.850	0.863	0.870	0.8750
7.5	0.728	0.784	0.822	0.840	0.858	0.871	0.878	0.8824
8.0	0.734	0.790	0.829	0.847	0.865	0.877	0.884	0.8889
8.5	0.740	0.796	0.835	0.854	0.871	0.883	0.890	0.8947
9.0	0.746	0.802	0.841	0.859	0.876	0.888	0.895	0.9000
9.5	0.751	0.807	0.846	0.864	0.881	0.893	0.900	0.9048
10.0	0.756	0.811	0.851	0.869	0.886	0.898	0.904	0.9091
20.0	0.796	0.865	0.906	0.922	0.935	0.943	0.948	0.9524
30.0	0.816	0.889	0.928	0.943	0.947	0.961	0.964	0.9677
40.0	0.826	0.903	0.942	0.955	0.963	0.971	0.974	0.9756
50.0	0.834	0.914	0.951	0.962	0.970	0.975	0.978	0.9804
60.0	0.844	0.920	0.957	0.968	0.974	0.980	0.982	0.9836
90.0	0.862	0.935	0.969	0.977	0.982	0.986	0.987	0.9890
100.0	0.867	0.939	0.971	0.979	0.984	0.987	0.989	0.9901
500.0	0.891	0.974	0.993	0.995	0.996	0.997	0.998	0.9980

For an unbalanced regenerator ( $C_R \neq 1$ ), the following procedure can be followed [8].

First the following equations are used to calculate “effective” values of  $Ntu$  and  $C_m$ .

$$Ntu_e = \frac{2Ntu_o C_R}{(1 + C_R)} \quad (2.10)$$

$$C_{m,e} = \frac{2C_m C_R}{(1 + C_R)} \quad (2.11)$$

These effective values can be used to find the effectiveness,  $\varepsilon_1$ , of a balanced regenerator in Table 2.1. Next the following parameter can be calculated:

$$X = \left( \frac{1 + C_R}{2C_R} \right) \left( \frac{\varepsilon_1}{1 - \varepsilon_1} \right) (1 - C_R) \quad (2.12)$$

Finally, the regenerator effectiveness for an unbalanced regenerator is given as:

$$\varepsilon = \frac{1 - \exp(-X)}{1 - C_R \exp(-X)} \quad (2.13)$$

The problem with using the  $\varepsilon$ -Ntu method as a design tool is that it doesn't provide a complete picture of the regenerator operation. The regenerator effectiveness given in Table 2.1 takes into account only the thermal effects. In a real regenerator however, there are other effects that will also contribute to the overall performance. The pressure drop, void volume effects, flow maldistributions, parasitic heat losses and longitudinal conduction are all losses which can seriously affect a regenerator; even one with an ideal thermal effectiveness. This method can be adapted to include longitudinal conduction but it does not allow for the incorporation of the other effects. Generally an iterative procedure is used. First, the effectiveness is calculated and then the pressure drop is checked. If the pressure drop is unacceptable then a new effectiveness is found and so on.

### 2.1.2 $\lambda$ - $\pi$ Method

Hausen developed the  $\lambda$ - $\pi$  method in 1976 [8]. It involves dimensionless parameters defined separately for the hot blow and the cold blow through the regenerator. The parameters are reduced length,  $\lambda$ , and reduced period,  $\pi$  and are defined as:

$$\lambda_h = \frac{h_h A_{s,h}}{\dot{m}_h c_h} \text{ and } \lambda_c = \frac{h_c A_{s,c}}{\dot{m}_c c_c} \quad (2.14)$$

$$\pi_h = \frac{h_h A_{s,h} P_h}{m_{sh} c_s} \text{ and } \pi_c = \frac{h_c A_{s,c} P_c}{m_{sc} c_s} \quad (2.15)$$

A regenerator is considered symmetric if  $\pi_h = \pi_c$  and balanced if  $\lambda_h/\pi_h = \lambda_c/\pi_c$ . A large reduced length and small reduced period is necessary for a highly effective regenerator. For an ideal regenerator,  $\pi=0$  and the effectiveness reduces to:

$$\varepsilon_{\text{reg}} = \frac{\lambda}{\lambda + 2} \quad (2.16)$$

This equation can be used as an estimate of the regenerator effectiveness. Table 2.2 gives the effectiveness of a balanced and symmetric regenerator as a function of  $\pi$  and  $\lambda$  as presented by Schmidt and Wilmott [25].

**Table 2.2: Regenerator effectiveness as a function of  $\pi$  and  $\lambda$  for a symmetric and balanced regenerator**

Reduced length, $\Lambda$	Reduced period, $\Pi$					
	0	10	20	30	40	50
5	0.714	0.469	0.250	0.167	0.125	0.100
10	0.833	0.738	0.494	0.333	0.250	0.200
15	0.882	0.840	0.693	0.498	0.375	0.300
20	0.909	0.886	0.811	0.651	0.400	0.400
25	0.926	0.911	0.871	0.770	0.620	0.500
30	0.936	0.927	0.903	0.845	0.727	0.598
35	0.946	0.939	0.922	0.888	0.810	0.692
40	0.952	0.947	0.935	0.912	0.865	0.773
45	0.957	0.953	0.944	0.928	0.898	0.835
50	0.962	0.958	0.951	0.939	0.909	0.875

For an unbalanced and unsymmetrical regenerator the following procedure can be used. First, the harmonic mean values for the reduced length and reduced period are calculated.

$$\frac{2}{\pi_m} = \frac{1}{\pi_h} + \frac{1}{\pi_c} \quad (2.17)$$

$$\frac{2}{\lambda_m} = \frac{1}{\pi_m} \left( \frac{\pi_h}{\lambda_h} + \frac{\pi_c}{\lambda_c} \right) \quad (2.18)$$

These values are used to find a value for the regenerator effectiveness in Table 2.2. The effectiveness of an unbalanced and unsymmetrical regenerator can then be found using equations (2.12) and (2.13). This method suffers from the same drawbacks as the  $\varepsilon$ -Ntu method.

### 2.1.3 2<sup>nd</sup> Law of Thermodynamics Method

The 2<sup>nd</sup> Law method examines the rate of entropy production within a regenerator [17]. For an ideal refrigerator, the amount of work required to produce a given amount of cooling,  $\dot{Q}_c$ , is given as:

$$\dot{W} = \dot{Q}_c \left( \frac{T_h}{T_c} - 1 \right) \quad (2.19)$$

In a real device, entropy will be produced, increasing the amount of work required to produce the same amount of cooling.

$$\dot{W} = \dot{Q}_c \left( \frac{T_h}{T_c} - 1 \right) + T_h \dot{S}_{\text{total}} \quad (2.20)$$

where  $\dot{S}$  is the rate of entropy production

Equations (2.19) and (2.20) can be used to define a figure of merit (FOM) for the regenerator. The FOM is a measure of the effectiveness of the regenerator with the minimum entropy generation rate corresponding to the highest FOM.

$$\text{FOM} = \frac{\dot{W}_{\text{ideal}}}{\dot{W}_{\text{real}}} = \frac{\dot{Q}_c \left( \frac{T_h}{T_c} - 1 \right)}{\dot{Q}_c \left( \frac{T_h}{T_c} - 1 \right) + T_h \dot{S}_{\text{total}}} \quad (2.21)$$

For a regenerator, some of the largest sources of entropy are as follows:

- Entropy generation due finite heat transfer between the fluid and solid:

$$\dot{S}_{\text{HT}} = \frac{\dot{m}c_p(T_h - T_c)}{Ntu + 1} \left( \frac{1}{T_c} - \frac{1}{T_h} \right) \quad (2.22)$$

- Entropy generation due to fluid pumping power:

$$\dot{S}_{\Delta P} = \frac{\dot{m}\Delta P}{\rho T_H} \quad (2.23)$$

where  $\Delta P$  is the pressure drop across the regenerator and  $\rho$  is the fluid density

- Entropy generation due to axial solid conduction:

$$\dot{S}_{\text{ks}} = \frac{(1 - \alpha)k_s A_c (T_h - T_c)}{L} \left( \frac{1}{T_c} - \frac{1}{T_h} \right) \quad (2.24)$$

- Entropy generation due to axial fluid conduction:

$$\dot{S}_{\text{kf}} = \frac{\alpha k_f A_c (T_h - T_c)}{L} \left( \frac{1}{T_c} - \frac{1}{T_h} \right) \quad (2.25)$$

In many cases, the entropy generated by axial fluid conduction is very small compared to the other terms and may be neglected.

The total entropy generation in the regenerator is then calculated as:

$$\dot{S}_{\text{total}} = \dot{S}_{\text{HT}} + \dot{S}_{\Delta P} + \dot{S}_{\text{ks}} + \dot{S}_{\text{kf}} \quad (2.26)$$

Minimizing the entropy production can optimize the regenerator design. This method has advantages over the  $\epsilon$ -Ntu and  $\lambda$ - $\pi$  method. First, it takes into account all of the loss mechanisms in the regenerator instead of concentrating on the thermal effects. Second, because the different losses are evaluated separately it is possible to determine which losses are dominant and concentrate on reducing them.

The difficulty in optimizing a regenerator lies in the fact that the different mechanisms tend to act against each other. For instance, shortening the bed will decrease  $\dot{S}_{\Delta P}$  but increase both  $\dot{S}_{\text{ks}}$  and  $\dot{S}_{\text{kf}}$ .

### 3. Relevant Porous Media Research

---

Use of the design methods described in Chapter 2 requires knowledge of the properties of the regenerator bed. In particular, it is necessary to know something about the heat transfer coefficient between the fluid and the solid, the thermal conductivity of the solid matrix, the thermal conductivity of the fluid and the pressure drop across the bed. There has been a lot of work done to determine semi-empirical correlations for these parameters in various regenerator geometries.

#### 3.1 Predictions for the Performance of Packed Beds

A regenerator that is made of many individual particles is referred to as a packed bed. Most of the previous work done on packed beds has concentrated on spherical particles. However, it is possible to apply the correlations developed for spheres to other particle geometries such as cylinders, rings or flakes by calculating an equivalent diameter. The equivalent diameter is usually calculated as:

$$D_{\text{eq}} = \frac{6V_p}{A_p} \quad (3.1)$$

where  $V_p$  is the volume of a particle and  $A_p$  is the surface area of a particle

For spherical particles  $D_{\text{eq}} = D_p$ . A variation on this is suggested by Perry [18] to better account for the difference in shapes.

$$D_{\text{eq}} = \frac{6V_p(1-\alpha)}{A_p\phi_s} \quad (3.2)$$

where  $\phi_s$  is a shape factor

Shape factors for a number of different geometries are shown in Table 3.1.

**Table 3.1: Shape factors for Nonspherical Particles [18]**

Material	Nature of grain	$\phi_s$
Arnould's wire spirals		0.2
Berl saddles		0.3
Coal dust, natural (up to 3/8 in.)		0.65
Coal dust, pulverized		0.73
Cork		0.69
Flue dust	Fused, spherical	0.89
Flue dust	Fused, aggregates	0.55
Fusain fibers		0.38
Glass, crushed	Jagged	0.65
Mica flakes		0.28
Raschig Rings		0.3
Sand:		
Average for various types		0.75
Flint sand	Jagged	0.65
Flind sand	Jagged flakes	0.43
Ottawa sand	Nearly spherical	0.95
Sand	Rounded	0.83
Sand	Angular	0.73
Wilcox sand	Jagged	0.60
Tungsten powder		0.89

Gamson also defines a shape factor for use with non-spherical particles. He defines the equivalent diameter as:

$$D_{eq} = \frac{6V_p}{A_p\phi_s} \quad (3.3)$$

where  $\phi_s$  is defined for various geometries in Table 3.2.

**Table 3.2: Gamson's shape factors for non-spherical particles [19]**

Shape	$\phi_s$
Spheres	1
Cylinders	0.91
Flakes	0.86
Raschig rings	0.79
Partition rings	0.67
Berl saddles	0.80

### 3.1.1 Heat Transfer Coefficient

Much research has been done investigating heat transfer in packed beds. The heat transfer modes involved include convection between the fluid and the particles, conduction between particles, axial fluid conduction, radiation between particles, and radiation between particles and the fluid. There are also thermal interactions with the regenerator wall. Heggs [20] reviewed some of the published data and attempted to explain why it was widely scattered over the entire Reynolds number range. He concluded that the different experimental methods used were partly to blame as well as the means used to interpret the data. The value of the heat transfer coefficient varied according to which modes of heat transfer were taken into account. In this reference, Heggs discussed the different experimental methods; both steady state and transient, and concluded that the steady state methods were not sufficiently reliable to be incorporated into a correlation. Heggs also presented a correlation by Wakao that was developed by reviewing published heat transfer data and correcting for the effects of axial thermal dispersion. It is valid for Reynolds numbers between 15 and 8500 and is given as:

$$\text{Nu} = \frac{hD_{\text{eq}}}{k_f} = 2 + 1.1\text{Pr}^{\frac{1}{3}} \text{Re}^{0.6} \quad (3.4)$$

where Nu is the Nusselt number, Pr is the Prandtl number, Re is the Reynolds number ( $GD_{\text{eq}}/\mu$ ), where G is the mass flow rate per unit area and  $\mu$  is the fluid viscosity.

Kays and London [21] present correlations for the heat transfer coefficient of spheres, screens and crossed-rod matrices based on experimental data. For spheres, they define the heat transfer coefficient as:

$$j = \frac{h}{Gc_p \text{Pr}^{-2/3}} = 0.23(\alpha \text{Re})^{-\frac{1}{3}} \quad (3.5)$$

where j is the Colburn j number

In an earlier article, Coppage and London [22] present correlations for spheres and screens and also suggest the possibility of a correlation based on porosity alone after the examination of published data on non-spherical granular porous media.

A commonly used correlation for the heat transfer coefficient in a packed bed was developed experimentally by Handley and Heggs [23]. The correlation for spherical particles is given as:

$$j = \frac{h}{Gc_p \text{Pr}^{-2/3}} = 0.255(\alpha \text{Re})^{-1/3} \quad (3.6)$$

Equation (3.6) can also be written in a general form:

$$j\alpha = c \text{Re}^{-m} \quad (3.7)$$

where  $c$  and  $m$  are empirical constants that are strongly dependent on the shape and orientation of the packing in the bed.

This invalidates the earlier suggestion from Coppage and London of a correlation based solely on porosity. Timmerhaus and Flynn [24], Barron [8], and Schmidt and Wilmott [25] all recommend equation (3.6) for estimation of the heat transfer coefficient correlation in a bed of packed spheres.

### 3.1.2 Pressure Drop

The only accurate method of determining the pressure drop across a packed bed is to measure it experimentally. There is a semi-empirical correlation however, which has been proven to represent, within 50%, the pressure drop for a wide variety of porous media. This correlation was developed by Ergun [27].

$$f \frac{\alpha^3}{(1-\alpha)} = \frac{\Delta P D_{eq}}{\rho v_o^2 L} = \left[ \frac{150(1-\alpha)}{Re_o} + 1.75 \right] \quad (3.8)$$

where  $f$  is a friction factor,  $v_o$  is the superficial velocity (the velocity if the bed was empty) and  $Re_o$  is the Reynolds number calculated using  $v_o$ .

Bird, Stewart and Lightfoot [26] give a detailed explanation of the origins of the Ergun equation. Prior to Ergun's work one equation was developed for laminar flow:

Blake-Kozeny equation:

$$f \frac{\alpha^3}{(1-\alpha)} = \frac{\Delta P D_{eq}}{\rho v_o^2 L} = \frac{150(1-\alpha)}{Re_o} \quad (3.9)$$

and another for highly turbulent flow:

Burke-Plummer equation

$$\Delta P = \frac{1.75 L \rho v_o^2 (1-\alpha)}{D_{eq} \alpha^3} \quad (3.10)$$

Ergun [27] examined the pressure drop results measured across various beds by other researchers, such as Morcom [28], and discovered that the pressure drop across a packed bed could be treated as the sum of the viscous and inertial effects. Therefore, he added equations (3.9) and (3.10) together to get equation (3.8). The coefficients in equation (3.9) and (3.10) are known as the Ergun factors. Experimental data are shown plotted against these three equations in Figure 3.1. The superficial Reynolds number divided by  $(1-\alpha)$  is plotted on the x-axis and on the y-axis is the friction factor multiplied by  $\alpha^3/(1-\alpha)$ .

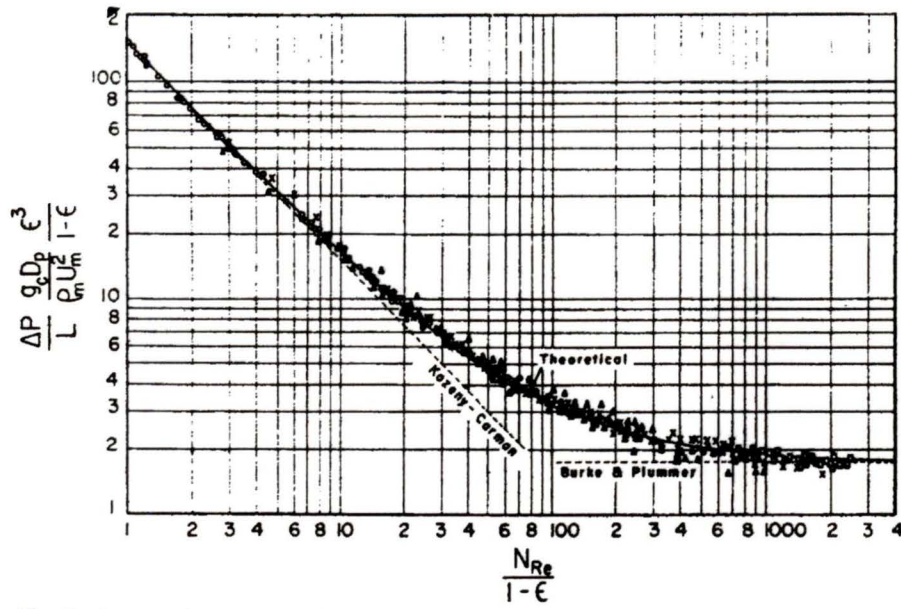


**Figure 3.1: Comparison of experimental data with the Ergun equation [27]**

Macdonald [29] evaluated the Ergun equation through comparison with a number of sets of experimental data with a wide variety of packing shapes. He modified equation (3.8) by changing the Ergun factors to 180 and 1.8 from 150 and 1.75. He also suggested that the 1.8 should be varied between 1.8 and 4 depending on the roughness of the particles with smooth particles using 1.8 and the roughest using 4.

Handley and Heggs [23] measured the pressure drop across packings of various size and shape. They concluded that no one single correlation for pressure drop can be applied to all porous media and suggest that to obtain a high degree of accuracy the Ergun-Macdonald factors should be determined empirically for each specific type and size of packing. They found that different correlations were needed not only for cylinders and spheres but also for different cylinder  $L/D$  ratios. Appel and Eder [30] performed experiments on various shapes to validate the Ergun model at very low Reynolds number. They also found that the pressure drop depended on the shape and roughness of the object. Experiments performed by Martin et al. [31] determined that the orientation of

the packing can also effect the pressure drop and should therefore be considered when evaluating correlations.

### **3.1.3 Longitudinal Conduction**

An assumption that is often made in regenerator analysis is that the longitudinal or axial conduction through the regenerator bed is zero. Although this does greatly simplify the analysis, in most cases it is not valid. In normal regenerator operation, a temperature gradient is created along the length of the bed. Any heat conducted from the hot to the cold end of the bed will degrade the performance. A number of researchers have studied this loss in performance. Bahnke and Howard [32] and Kroeger [33] were among the pioneers developing methods for calculating regenerator effectiveness taking into account the effects of longitudinal conduction. Romie [34] is a more recent reference that presents a method of including the effects of axial conduction in the regenerator analysis and also calculates the associated errors. Beveridge and Haughey [35] and Trevisan [36] have conducted experiments to measure the axial heat transfer in stagnant beds. Vortmeyer and Adam [37] measured the axial heat transfer in packed beds with gas flowing through them.

There are two contributors to longitudinal conduction in the bed: the conduction through the fluid and the conduction through the solid matrix.

#### **3.1.3.1 Thermal Conductivity of the Solid Matrix**

The thermal conductivity of the porous solid is needed to calculate the amount of longitudinal conduction occurring within the matrix. The upper limit is the conductivity of a solid block of the matrix material multiplied by (1-porosity). For a more accurate estimate, the conductivity must be further reduced to account for point contact between

the particles. Unfortunately most of the work done to determine the thermal conductivity of a porous bed has taken into account both the fluid and solid conductivity. One of the objectives of this thesis is to separate the loss mechanisms, and to quantitatively predict the thermal conductivity of the solid and the fluid independently. Because gases typically have very low molecular thermal conductivity it is reasonable to approximate the conductivity of the solid matrix by the effective conductivity in a stagnant bed. Determining the effective conductivity of a stagnant porous bed can be done either by experimentation to develop semi-empirical correlations, as is described by Yagi et al. [38] and Duncan et al. [39], or through application of an analytical expression. Tsotsas and Martin [40] have summarized the various types of experiments used to estimate the thermal conductivity in packed beds and also discussed some of the analytical expressions available. The first and simplest of these was presented by Maxwell in 1873. He considered a dilute dispersion of spheres in which the perturbation around each sphere is independent of the neighbouring spheres. The expression, given below, is valid for packed beds in the limit where the porosity approaches 1. Hsu, Cheng and Wong [41] suggest that it therefore provides a good lower limit of the thermal conductivity in packed beds. Tsotsas and Martin [40] state that equation (3.11) provides good results for packed beds as long as the value of  $k_s$  is not too high.

$$\frac{k_e}{k_f} = \frac{1 + 2\phi}{1 - \phi} \quad (3.11)$$

$$\text{where } \phi = (1 - \alpha) \frac{\lambda - 1}{\lambda + 2}, \quad (3.11a)$$

$$\lambda = \frac{k_s}{k_f}, \text{ and} \quad (3.11b)$$

$k_e$  is the effective stagnant thermal conductivity of the matrix.

Bauer [42] generalized Maxwell's approach to include pores of any concentration and shape through the addition of an empirical shape factor.

A slightly different approach developed by Krischer, which is also discussed in ref. [40], simulates a dispersed two-phase system by a combination of resistances that are connected partly in series and partly in parallel. The coefficient, in equation (3.12), denotes the relative proportion of the resistances in series with packed beds having  $a \approx 0.2$ . The case with the maximum resistance, where all the heat must pass through the poor conducting phase, corresponds to  $a=1$  whereas  $a=0$  corresponds to the case where all of the heat passes through the good conducting phase. The equations are given as:

$$\frac{1}{k_e} = \frac{1-a}{k_1} + \frac{a}{k_2} \quad (3.12)$$

$$\text{where } k_1 = \alpha + (1-\alpha)k_s, \quad (3.12a)$$

$$k_2 = \left( \alpha + \frac{1-\alpha}{k_s} \right)^{-1}, \text{ and} \quad (3.12b)$$

$a$  is approximately 0.2 for packed beds.

Zehner and Bauer developed the third model discussed in reference [40]. It uses a deformation factor,  $B$ , that allows finite-area contacts between particles in the bed to be taken into account. Often when a bed is under pressure the spheres will become slightly deformed, thereby creating finite-area contacts instead of point contacts. Also, this deformation factor can be useful when describing particles of shapes other than spherical.

$$\frac{k_e}{k_f} = 1 - \sqrt{(1-\alpha)} + \sqrt{(1-\alpha)}k_1 \quad (3.13)$$

$$\text{where } k_1 = \frac{2}{N} \left( \frac{B}{N^2} \frac{\lambda-1}{\lambda} \ln \left( \frac{\lambda}{B} \right) - \frac{B+1}{2} - \frac{B-1}{N} \right), \quad (3.13a)$$

$$B = 1.25 \left( \frac{1-\alpha}{\alpha} \right)^{\frac{10}{9}}, \quad (3.13b)$$

$$N = 1 - \frac{B}{\lambda}, \text{ and} \quad (3.13c)$$

$$\lambda = \frac{k_s}{k_f} \quad (3.13d)$$

Hsu et al. [41] also proposed models that take into account finite-area contacts between spheres in a bed and presented a variation of the Zehner and Bauer model described above, the Zehner-Schlunder model.

$$\frac{k_e}{k_f} = 1 - \sqrt{(1-\alpha)} + \frac{2\sqrt{(1-\alpha)}}{1-\lambda B} \left[ \frac{(1-\lambda)B}{(1-\lambda B)^2} \ln\left(\frac{1}{\lambda B}\right) - \frac{B+1}{2} - \frac{B-1}{1-\lambda B} \right] \quad (3.14)$$

where: the shape factor  $B = 1.364 \left( \frac{1-\alpha}{\alpha} \right)^{1.055}$  and (3.14a)

$$\lambda = \frac{k_f}{k_s} \quad (3.14b)$$

As with the heat transfer coefficient and the pressure drop, applying a single expression for thermal conductivity to all porous media may not give accurate results. Although the pressure drop and heat transfer coefficient have been investigated for a wide variety of shapes, most of the research available on thermal conductivity in packed beds is for spherical particles only. While some of the expressions are general in form, it is still necessary to determine the shape factors experimentally.

A comparison of the different correlations was performed to help decide which gives the best approximation. Determining the results as a function of porosity checked the limits of the equations. The results, with  $k_s/k_f = 100$ , are displayed in Figure 3.2. As expected, at zero porosity, the conductivity of the matrix becomes equal to the conductivity of a block of the solid material and at 100% porosity, the matrix conductivity becomes the fluid molecular conductivity.

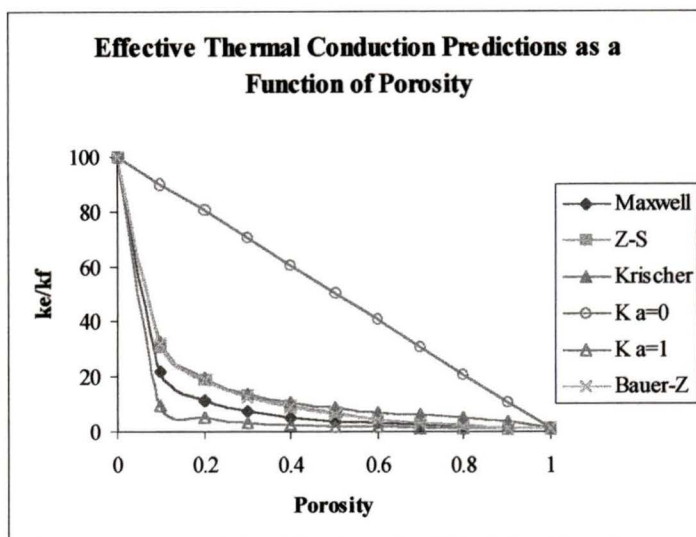


**Figure 3.2: Results of effective thermal conduction correlations as a function of porosity**

Next, the results for a range of fluid to solid conductivities were compared. In Figure 3.3 the range of values increases as  $k_s/k_f$  moves away from unity in either direction. The Krischer model does not seem to be very accurate at low values of  $k_s/k_f$ . For this thesis the range of interest is at high values of  $k_s/k_f$ . Here the spread is large and values vary by about  $\pm 50\%$ .

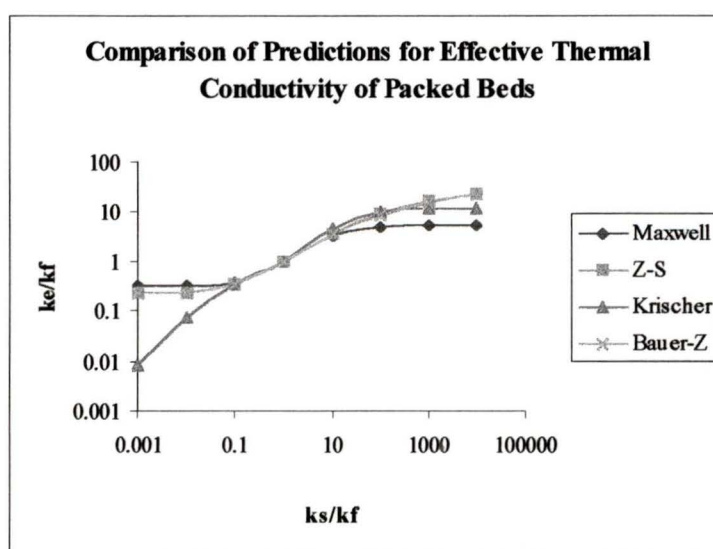


**Figure 3.3: Comparison of effective thermal conductivity correlations**

### 3.1.3.2 Fluid Thermal Conductivity including Eddy Diffusivity Effects

In many cases, even if the longitudinal conduction through the matrix is included in the regenerator analysis, it is assumed that the fluid conductivity can be ignored. For many geometries, this assumption is reasonable because of the low molecular conductivity of most gases. However, in the case of packed beds, the effects of the eddy diffusivity can be a significant effect, at all but quite low flow rates, and cannot be neglected. Eddy diffusivity is the physical mixing of the flow around particles in the axial direction of the bed. This causes thermal conduction in the axial direction through the fluid. The mass diffusivity,  $D$ , and the thermal diffusivity,  $\phi = k / \rho c_p$ , including both molecular and eddy components may be assumed to be the same quantity because heat and mass transfer occur through the same mechanism [43].

Edwards and Richardson [44] experimentally determined the relationship between the dispersion coefficient,  $D = k / (\rho c_p)$  and the Reynolds number in a packed bed. They found the following relationship:

$$Pe = \left[ \frac{0.38}{Re} + \frac{0.5 Re}{5 + Re} \right]^{-1} \quad (3.15)$$

where  $Pe = \text{Peclet number} = \frac{GD_p}{\alpha \rho D}$

Above a Reynolds number of 2, the Peclet number has an approximately constant value of 2. This relationship leads to the following correlation for the fluid conductivity of a packed bed including the eddy diffusivity:

$$k_f = \frac{Gc_p D_p}{2\alpha} \quad (3.16)$$

Sarangi and Baral [43] developed a model in which the effect of the fluid conductivity, as given by equation (3.16), is included. They compared the results to models where the

conduction through the fluid is neglected. The difference was found to be significant, as much as doubling the ineffectiveness in some cases.

### 3.2 Correlations for Wire Bundles

Because this is a new regenerator geometry, there are no semi-empirical correlations like those developed for packed beds. However, because of the precise nature of the geometry, it is possible to develop theoretical predictions for how the bed will behave. The orientation of the wires is assumed to be as shown in Figure 3.4.

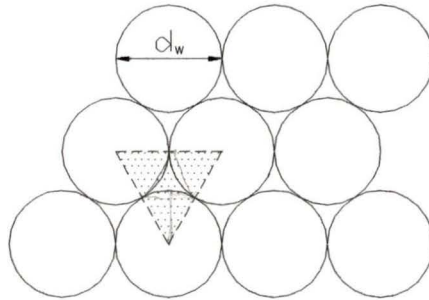


**Figure 3.4: Orientation of wires in a cross-section of the regenerator bed**

If the wires are the same length as the regenerator bed, then the behaviour of the flow in any channel can be approximated as flow through a triangular duct. This approximation can still be used if the wires are cut into smaller sections, however, it may become necessary to consider entrance effects. In this thesis, the hydraulic diameter of the void was much smaller than the length of the section and therefore fully developed flow was assumed in the analysis.

### 3.2.1 Pressure Drop

The area of the shaded triangle in Figure 3.4 is:

$$A_{\Delta} = \frac{1}{2} D_w \sqrt{D_w^2 - \left(\frac{1}{2} D_w\right)^2} = \frac{\sqrt{3}}{4} D_w^2 \quad (3.17)$$

where  $D_w$  is the wire diameter.

The area of the void is therefore:

$$A_{\text{void}} = \frac{\sqrt{3}}{4} D_w^2 - \frac{1}{6} (3) \frac{\pi}{4} D_w^2 = \frac{\sqrt{3}}{4} D_w^2 - \frac{\pi}{8} D_w^2 \quad (3.18)$$

This gives the porosity of the bed as:

$$\alpha = \frac{\frac{\sqrt{3}}{4} D_w^2 - \frac{\pi}{8} D_w^2}{\frac{\sqrt{3}}{4} D_w^2} = 1 - \frac{\pi}{2\sqrt{3}} = 0.093 \quad (3.19)$$

The number of wires and voids in the bed can then be calculated.

$$\# \text{ wires} = \frac{(1 - \alpha) A_{c, \text{reg}}}{A_{c, \text{wire}}} = \frac{(1 - 0.093) D_{\text{reg}}^2}{D_w^2} \quad (3.20)$$

$$\# \text{ voids} = \frac{\alpha A_{c, \text{reg}}}{A_{\text{void}}} \quad (3.21)$$

For flow through parallel channels, it is assumed that the total mass flow is divided equally among the channels. Therefore:

$$\dot{m}_{\text{void}} = \frac{\dot{m}}{\# \text{ voids}} \quad (3.22)$$

The hydraulic diameter is defined as:

$$D_h = \frac{4A_{\text{void}}}{P_{\text{void}}} = \frac{4A_{\text{void}}}{\frac{1}{2} \pi D_w} \quad (3.23)$$

This is used to calculate the Reynolds number as follows:

$$\text{Re} = \frac{GD_h}{\mu} \quad (3.24)$$

where  $G = \frac{\dot{m}_{\text{void}}}{A_v}$

If the flow channel is approximated as an equilateral triangle then according to White [45] the Fanning friction factor is given as:

$$f = \frac{12.8}{Re} \quad (3.25)$$

Kays and London [21] give the Fanning friction factor for a matrix of triangular tubes as:

$$f = \frac{13.33}{Re} \quad (3.26)$$

The pressure drop can then be found from:

$$\Delta P = \frac{2fG^2L}{\rho D_h} \quad (3.27)$$

### 3.2.2 Heat Transfer Coefficient

Ozisik [15] gives the Nusselt number for laminar flow in a triangular duct with “a uniform surface heat flux in both the flow direction and around the periphery” as:

$$Nu = 1.892 \quad (3.28)$$

The heat transfer coefficient can then be found using:

$$h = \frac{Nu k}{D_h} \quad (3.29)$$

### 3.2.3 Axial Conduction

Because the flow is able to follow a straight flow path through the wires, no mixing occurs and eddy diffusivity is not a concern. Therefore, the fluid conductivity in the bed is just the thermal conductivity of the fluid. For most gases this will be a very small number and therefore negligible.

The axial conduction through the solid though will be far from negligible. Because there is an uninterrupted conduction path along the length of the wire from the hot end to the cold end of the regenerator, the axial conduction will simply be the thermal conductivity of the solid reduced by the porosity.

This can be greatly reduced by slicing the wire bundle into cross-sections. The axial conduction can then be approximated as two thermal systems connected in series. Using this assumption allows the effective thermal conductivity of the bed to be calculated as:

$$k_e = \frac{k_s L}{\frac{Nt}{(1-\alpha)} + \frac{(N-1)sA_c}{A_{cs}}} \quad (3.30)$$

where  $N$  is the number of sections,  $t$  is the section thickness,  $s$  is the spacing between the sections and  $A_{cs}$  is the cross-sectional area of the spacers

Equation (3.30) assumes that the spacers are made of the same material as the wires.

## 4. Regenerator Testing Methods

---

The design methods described in Chapter 2 combined with the semi-empirical correlations discussed in Chapter 3 can provide a good estimate for the performance of a regenerator. However, it is only an estimate. For a better characterization of the performance of a given regenerator, it is necessary to actually test it. A number of different test methods have been developed and will be discussed in the following sections.

### 4.1 Integral Method

In the Integral test method, constant pressure flow is cycled between two regenerators. The ends of the beds are kept constant at  $T_{\text{hot}}$  and  $T_{\text{cold}}$ . A schematic of this method is shown in Figure 4.1.

Any ineffectiveness in the regenerators will create a flow of heat that will cause some of the cryogen to boil off. By measuring the amount of boil-off and using the following equation, the level of ineffectiveness can be determined:

$$1 - \text{eff} = \frac{\dot{Q}_{\text{boil-off}}}{(T_{\text{hot}} - T_{\text{cold}})\dot{m}c_p} = \frac{\dot{m}_{\text{LH}_2} h_{\text{fg}}(\text{H}_2)}{(T_{\text{hot}} - T_{\text{cold}})\dot{m}c_p} \quad (4.1)$$

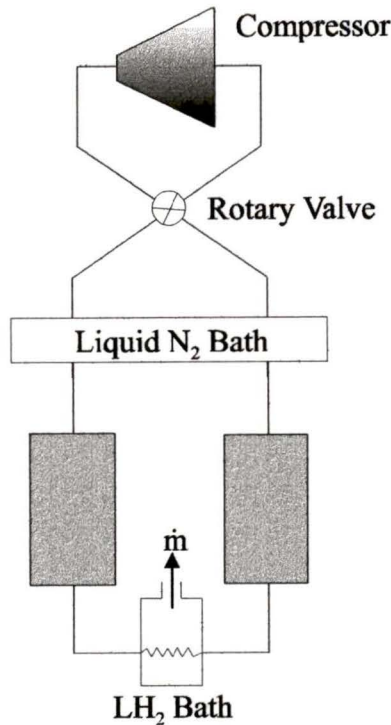


**Figure 4.1: Schematic of integral test method**

Chhatwal et al. [46] give a more detailed description of an integral test apparatus. One of the disadvantages of this method is that testing highly effective regenerators is difficult due to the small amount of boil-off produced. Perhaps more importantly in terms of the work in this thesis, it is not possible to separate the factors contributing to the regenerator ineffectiveness.

## 4.2 Actual Refrigerators

By using the regenerator in an actual refrigerator, the performance can be tested under practical conditions. There are a few disadvantages with this method. First, as with the integral method, it is not possible to separate the causes of ineffectiveness in the regenerator. Second, it can be very expensive to obtain a refrigeration cycle for use in testing. Third, it may not be easy to interpolate results from one refrigeration cycle to another. However, this is the best way to determine how a regenerator will perform in a

given refrigeration cycle. Kratschmar [47] and Yaron [48] both describe the testing of regenerators in actual devices.

### 4.3 Differential Method

The differential method is a relatively easy and inexpensive method for testing regenerators. It is useful for deciding whether a regenerator is worth going to the trouble and expense of testing in a real refrigerator. Also, it allows the different characteristics of the regenerator such as heat transfer, pressure drop, fluid and solid axial conduction to be separately determined. For these reasons it was chosen as the method for testing regenerators in this thesis.

In the differential method, also known as the single blow method, the regenerator bed starts out at some initial temperature. Then, the temperature the fluid flowing through the bed is suddenly and sharply changed. The temperature is measured at various locations along the bed as the thermal wave propagates through the matrix until steady state is reached i.e.  $T_{in} = T_{out}$ . A schematic of this method is shown in Figure 4.2.

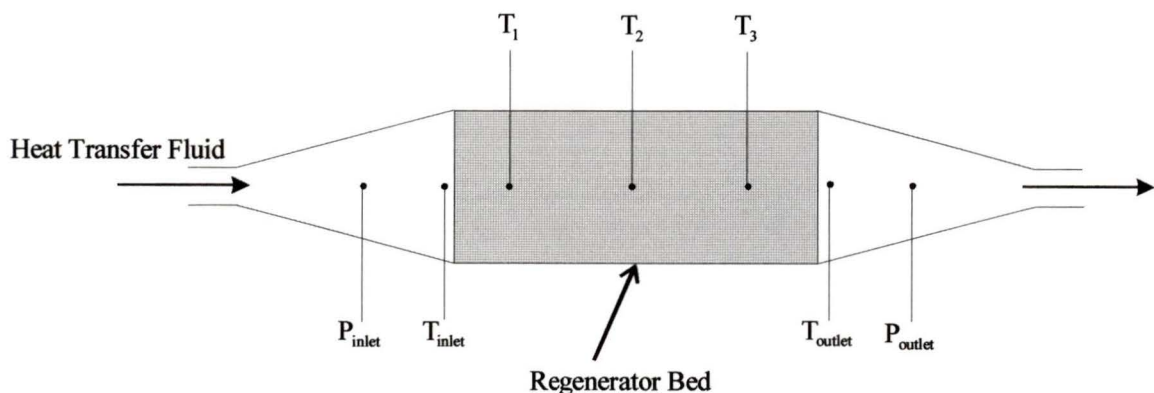


**Figure 4.2: Schematic of differential test apparatus**

In an ideal regenerator the thermal wave will propagate as a square wave, similar to the one in Figure 4.3. The temperatures  $T_{in}$ ,  $T_1$ ,  $T_2$ ,  $T_3$  and  $T_{out}$  are measured at various positions along the bed as shown in Figure 4.2. The fluid temperature measured at the exit of the regenerator ( $T_{out}$ ) will remain at the initial bed temperature ( $T_i$ ) until the square wave reaches the exit and will then jump suddenly to the inlet fluid temperature ( $T_i + \Delta T$ ).

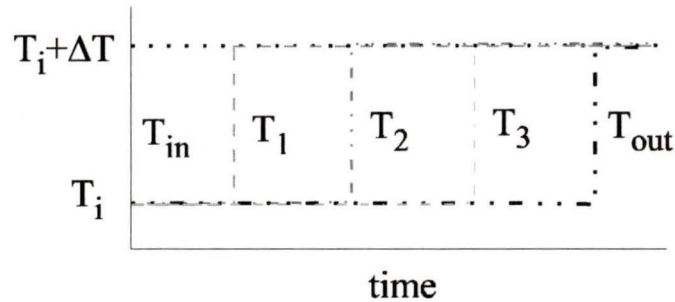


**Figure 4.3: Temperature profile during a single blow through an ideal regenerator**

In a real regenerator, the wave will be degraded by loss mechanisms such as longitudinal conduction and finite heat transfer, as illustrated in Figure 4.4. The slopes of the temperature-time profiles can be matched with theoretical predicted curves to determine various parameters such as the heat transfer coefficient and the thermal conductivity.

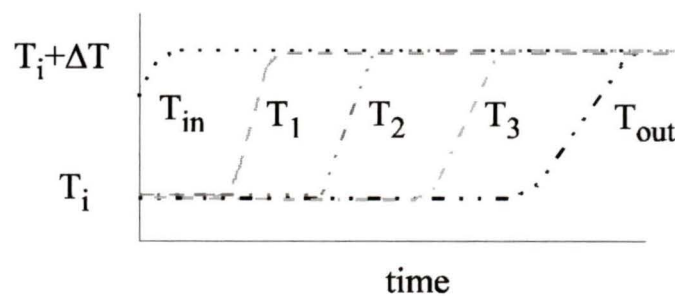


**Figure 4.4 : Temperature profile during a single blow through a real regenerator**

In Figure 4.4, the thermal wave doesn't reach the exit ( $T_{out}$ ) all at once. Instead the transition from  $T_i$  to  $T_i + \Delta T$  is gradual. In the extreme case of a very poor regenerator the sharpness of the wave would become so deteriorated that the exit temperature would begin rising at almost the same time as the temperature change occurred.

### 4.3.1 Temperature Change Generation

There are a number of methods that have been developed to produce the sudden input temperature change required for the differential test method. The more common are fast response heaters, using valves to switch between hot and cold flow loops, and moving the regenerator bed between a hot and cold stream. In this work, a combination of a fast response heater and flow switching was used.

It is important to generate a very sharp change temperature in the heat transfer fluid prior to entering the bed because otherwise the thermal wave will not start out as a square wave. This effect will propagate down the bed and the slope at each position along the bed will be less than if the temperature change had been instantaneous. The effectiveness of the bed will then be undervalued. Loehrke [49] determined the errors associated with a slower temperature change and demonstrated the importance of accurately representing the temperature change in the analysis.

Some researchers have used a variation of the single-blow test method. Oldson [50] uses a pulse of heat instead of a single step change in temperature. Stang [51] replaces the step temperature wave with a sinusoidal temperature wave. These methods claim to overcome some of the difficulties associated with generating a square wave. In the pulse method however, Oldson states that it becomes difficult to extract the heat transfer coefficient from the data obtained at  $Ntu \gg 1$ .

### 4.3.2 Analysis Techniques

The results of a differential test can be evaluated using the maximum slope method, area slope matching method and the full curve matching method.

#### 4.3.2.1 Maximum Slope Method

By measuring the temperature at the exit of the regenerator bed, a profile similar to the one labelled  $T_{\text{out}}$  in Figure 4.4 will be obtained. The maximum slope of this curve will be a unique function of the Ntu of the bed. This principle forms the basis of the maximum slope method. Anzelius, Nusselt, Hausen and Schumman in the late 1920's developed analytical solutions to determine the fluid and solid temperatures as a function of time and position in the bed after the introduction of a sudden temperature change. Furnas [52] was the first to evaluate test data using Schumann's solution [53]. In 1950, Locke differentiated Schumann's analytical expression to obtain an expression for the generalized heating curve. He observed that the maximum slope was a unique function of Ntu and thus developed the maximum slope method. Howard expanded these results to include the effects of longitudinal conduction. Table 4.1 presents values of Ntu as a function of maximum slope and axial conduction [54].

One problem with this method is that the numerical analytic results are difficult to obtain at high values of Ntu [54] and therefore it cannot be used to evaluate highly effective regenerators [55]. Also, to obtain the Ntu from Table 4.1, it is necessary to either assume zero longitudinal conduction or to be able to obtain a value for this parameter. Zero longitudinal conduction is an assumption that is often made but is never truly valid. For many geometries it is difficult to calculate the axial conduction to a reasonable degree of accuracy and correlations are not always available.

Li and Shah [56] used numerical techniques to compute a table similar Table 4.1 but which they claim is about 2% more accurate. Many other researchers have used the maximum slope method as a means of testing compact heat exchangers or regenerators [57][58][59].

**Table 4.1: Maximum slope as a function of  $Ntu$  and  $\lambda$** 

$Ntu \backslash \lambda$	0	0.005	0.01	0.015	0.02	0.025	0.03	0.035	0.04	0.06	0.08	0.1	0.5	1	10	Inf.
1.0	0.368	-	-	-	0.374	-	-	-	0.377	0.380	0.382	0.384	-	-	-	0.400
1.1	0.403	-	-	-	0.408	-	-	-	0.413	0.417	0.420	0.425	-	-	-	0.445
1.2	0.434	-	-	-	0.440	-	-	-	0.445	0.447	0.452	0.459	-	-	-	0.488
1.3	0.461	-	-	-	0.467	-	-	-	0.472	0.475	0.480	0.487	0.499	-	-	0.529
1.4	0.48	-	-	-	0.489	-	-	-	0.494	0.498	0.503	0.511	0.522	-	-	0.568
1.5	0.502	-	-	-	0.507	-	-	-	0.512	0.517	0.521	0.530	0.542	-	-	0.603
1.6	0.517	-	-	-	0.522	-	-	-	0.527	0.530	0.536	0.544	0.560	-	-	0.637
1.8	0.536	-	-	-	0.539	-	-	-	0.542	0.547	0.553	0.561	0.589	-	-	0.697
2.0	0.541	-	-	-	0.545	-	-	-	0.548	0.556	0.563	0.571	0.615	0.646	0.723	0.748
2.2	0.544	-	-	-	0.549	-	-	-	0.557	0.566	0.574	0.582	0.640	0.677	0.764	0.791
2.4	0.549	-	-	-	0.557	-	-	-	0.567	0.577	0.585	0.592	0.662	0.703	0.798	0.827
2.6	0.557	-	-	-	0.566	-	-	-	0.577	0.587	0.590	0.603	0.680	0.726	0.826	0.857
2.8	0.567	-	-	-	0.577	-	-	-	0.587	0.598	0.606	0.615	0.694	0.745	0.850	0.882
3.0	0.577	-	-	-	0.587	-	-	-	0.598	0.608	0.617	0.626	0.714	0.761	0.869	0.903
3.2	0.587	-	-	-	0.598	-	-	-	0.609	0.619	0.628	0.637	0.727	0.775	0.886	0.920
3.4	0.598	-	-	-	0.610	-	-	-	0.620	0.630	0.640	0.647	0.730	0.787	0.899	0.934
3.6	0.609	-	-	-	0.621	-	-	-	0.631	0.641	0.650	0.658	0.740	0.798	0.911	0.946
3.8	0.621	-	-	-	0.632	-	-	-	0.642	0.652	0.660	0.668	0.750	0.807	0.920	0.956
4.0	0.632	-	-	-	0.643	-	-	-	0.653	0.662	0.670	0.676	0.760	0.815	0.928	0.964
4.5	0.660	-	-	-	0.670	-	-	-	0.678	0.687	0.694	0.701	0.784	0.831	0.941	0.978
5.0	0.688	-	-	-	0.697	-	-	-	0.704	0.711	0.717	0.722	0.800	0.843	0.951	0.987
5.5	0.715	-	-	-	0.722	-	-	-	0.727	0.733	0.737	0.752	0.812	0.852	0.956	0.992
6.0	0.741	-	-	-	0.746	-	-	-	0.750	0.753	0.757	0.760	0.822	0.859	0.960	0.995
6.5	0.767	-	-	-	0.769	-	-	-	0.771	0.773	0.774	0.776	0.830	0.865	0.962	-
7.0	0.792	-	-	-	0.792	-	-	-	0.791	0.791	0.791	0.792	0.837	0.870	0.964	1.000
7.5	0.816	-	-	-	0.812	-	-	-	0.810	0.808	0.806	0.805	0.844	0.874	0.965	-
8.0	0.840	-	-	-	0.832	-	-	-	0.827	0.824	0.821	0.817	0.847	0.877	0.966	-
9.0	0.885	-	-	-	0.872	-	-	-	0.861	0.853	0.847	0.840	0.855	0.882	0.967	-
10.0	0.929	0.922	0.916	0.911	0.906	0.901	0.897	0.893	0.890	0.880	0.869	0.860	0.864	0.886	0.968	1.000
11.0	0.970	0.959	0.953	0.946	0.939	0.933	0.927	0.921	0.917	0.901	0.888	0.878	0.870	0.889	0.968	-
12.0	1.010	0.998	0.988	0.979	0.970	0.962	0.955	0.948	0.942	0.922	0.905	0.893	0.873	-	-	-
13.0	1.049	1.034	1.022	1.009	0.999	0.990	0.980	0.973	0.965	0.941	0.922	0.907	0.875	-	-	-
14.0	1.085	1.068	1.053	1.039	1.027	1.016	1.005	0.996	0.987	0.958	0.937	0.921	0.878	-	-	-
15.0	1.121	1.102	1.085	1.068	1.053	1.040	1.028	1.017	1.007	0.975	0.950	0.932	0.879	0.893	-	-
16.0	1.151	1.133	1.112	1.094	1.077	1.063	1.049	1.037	1.026	0.990	0.963	0.942	0.881	-	-	-
18.0	1.223	1.193	1.167	1.144	1.123	1.105	1.088	1.073	1.060	1.016	0.984	0.960	0.885	-	-	-
20.0	1.286	1.249	1.217	1.189	1.164	1.143	1.123	1.105	1.089	1.039	1.003	0.975	0.887	0.894	-	1.000
22.0	1.347	1.302	1.264	1.231	1.202	1.177	1.154	1.134	1.116	1.059	1.018	0.987	0.889	-	-	-
24.0	1.404	1.352	1.308	1.269	1.237	1.208	1.182	1.160	1.140	1.077	1.032	0.997	0.891	-	-	-
26.0	1.460	1.399	1.348	1.305	1.268	1.236	1.208	1.183	1.161	1.092	1.043	1.005	0.893	-	-	-
28.0	1.515	1.444	1.387	1.339	1.298	1.262	1.231	1.204	1.180	1.106	1.053	1.013	0.894	-	-	-
30.0	1.565	1.487	1.423	1.370	1.325	1.286	1.253	1.224	1.198	1.118	1.061	1.019	0.895	0.895	-	1.000
32.0	1.617	1.528	1.458	1.399	1.351	1.309	1.273	1.241	1.214	-	-	-	-	-	-	-
34.0	1.665	1.568	1.490	1.427	1.374	1.330	1.291	1.258	1.228	-	-	-	-	-	-	-
36.0	1.712	1.605	1.521	1.453	1.397	1.349	1.308	1.273	1.242	-	-	-	-	-	-	-
38.0	1.770	1.641	1.551	1.478	1.418	1.367	1.324	1.287	1.254	-	-	-	-	-	-	-
40.0	1.801	1.676	1.579	1.501	1.437	1.384	1.339	1.300	1.266	-	-	-	-	-	-	1.000
45.0	1.908	1.757	1.643	1.554	1.481	1.422	1.372	1.328	1.292	-	-	-	-	-	-	-
50.0	2.010	1.833	1.702	1.601	1.520	1.455	1.400	1.353	1.313	-	-	-	-	-	-	1.000
55.0	2.107	1.902	1.756	1.644	1.555	1.483	1.425	1.375	1.332	-	-	-	-	-	-	-
60.0	2.199	1.967	1.803	1.680	1.585	1.508	1.445	1.392	1.347	-	-	-	-	-	-	1.000

#### 4.3.2.2 Average Slope Matching Method

Another technique which has been used by some researchers, including Heggs [20] and Barclay [60], is the average slope method. This is very similar to the maximum slope method. However instead of using the maximum slope to compare the theoretical and experimental data an average slope is calculated over the time interval where the

temperature profile is between 20 and 80% of the final temperature. Kohlmayer [61] has shown this to overcome some of the difficulties associated with the maximum slope method.

#### 4.3.2.3 Full Curve Matching Method

The full curve matching method is employed in this thesis and was also used by Elliott and Rapley [62]. Instead of just measuring the temperature at the end of the bed as in the maximum slope method, the temperature is monitored at various locations along the bed, as illustrated in Figure 4.2. These measurements are then plotted against time to generate temperature profiles similar to those in Figure 4.4.

The experimental curves are matched to theoretical curves to determine the heat transfer coefficient, the fluid thermal conductivity and the solid thermal conductivity. The heat transfer coefficient can then be used to calculate the Ntu and subsequently the effectiveness of the test bed. The theoretical curves are generated by a computer program that solves equations (2.2) and (2.3), through numerical techniques. The particulars of this program are outlined in Chapter 5.

The sophistication of today's computers allows equations (2.2) and (2.3) to be accurately solved with relatively little computing time. Therefore it is unnecessary to use analytical solutions such as those described in the maximum slope method. This eliminates the restrictions imposed on the degree of regenerator effectiveness in the test beds. Also, it allows the separate analysis of the heat transfer coefficient and the axial thermal conduction.

## 5. Regenerator Modeling Program

---

A Fortran computer program was written to solve the energy equations for the propagation of a thermal wave in a single-shot regenerator test. After being validated, the model was used to analyze the experimental data as described in section 4.3.2.3.

### 5.1 System to be Modelled

The objective of the model was to simulate the conditions found in the experiments. The system therefore is the one shown in Figure 4.2. The regenerator starts out at steady state at some initial temperature and then a step temperature change is introduced. The model simulates the propagation of the thermal wave down the bed.

The equations to be solved are the regenerator energy equations, (2.2) and (2.3). They can be written in the following forms:

for the fluid

$$\rho_f u \left( \frac{\partial T_f}{\partial x} \right) = \frac{hA_s}{c_{pf} \alpha V_{reg}} (T_s - T_f) + \frac{k_f}{c_{pf}} \left( \frac{\partial^2 T_f}{\partial x^2} \right) \quad (5.1)$$

and for the solid:

$$\rho_s c_s \left( \frac{\partial T_s}{\partial t} \right) = \frac{hA_s}{(1 - \alpha) V_{reg}} (T_f - T_s) + k_s \left( \frac{\partial^2 T_s}{\partial x^2} \right) \quad (5.2)$$

### 5.1.1 Assumptions

The assumptions in the computer model are outlined below:

- The conduction in the radial direction is infinite. The thermal wave moves as plug flow and the temperature is constant across the diameter of the bed. This allows the analysis of the bed to be taken as 1-dimensional and greatly simplifies the solution.
- The packing in the bed is uniform (i.e. no channeling). The validity of this assumption depends on the amount of care used in the construction of the regenerator bed. If a large discrepancy between predicted and actual results occurs, it could be because this assumption is inaccurate.
- The fluid properties are independent of temperature. Because the experiments are being performed at room temperature and using a temperature difference of only 10°C, this is a reasonable assumption. It is possible to account for the variation of the fluid properties with temperature but the computation time is increased drastically for only a slight increase in accuracy.
- The input temperature change is a step function. If the time taken for the temperature change is much less than the time it takes the thermal wave to propagate down the bed, then this will be an acceptable assumption. The use of a fast response heater at the entrance to the bed and relatively low flow rates will assure a large difference in the relative times. This assumption can be avoided by fitting an equation to the input curve and using this as  $T_{inlet}$  in the model. This equation is of the form:

$$T_{\text{initial}} = T_{\text{initial}} + (T_{\text{final}} - T_{\text{initial}})(1 - \exp(-\text{time} * \text{heater time constant})) \quad (5.3)$$

where the heater time constant is the temperature change per second and is a function of the mass flow rate

An assumption that is not made is that the longitudinal conduction in the bed is zero. This is an assumption that has been made by a lot of researchers but is not accurate. Both the conduction through the solid and through the fluid have been taken into account. For many geometries, assuming zero fluid axial conduction is reasonable because of the low molecular thermal conductivity of most gases. However, in packed beds, the eddy diffusivity caused by the mixing of the fluid around the particles greatly increases the fluid conduction and can not be ignored.

### 5.1.2 Input Variables

There are a number of parameters that must be entered by the user. They allow a wide range of parameters to be modelled. The necessary input variables are:

- the geometry to be modelled (i.e. spheres, flakes, wires),
- the porosity,
- the dimensions of the regenerator bed (diameter and length),
- the material properties (density and specific heat of the solid, thermal conductivity),
- the fluid properties (density, specific heat, viscosity, thermal conductivity and Prandtl number),
- the mass flow rate of the fluid.

The choice of geometry is currently limited to those that were used in the experiments. It is possible to model other geometries by adding subroutines to calculate the total heat transfer area, the heat transfer coefficient, and the eddy diffusivity, if applicable.

### 5.1.3 Output Variables

The program writes the fluid and solid temperature profiles to output files. The temperature at  $x=0$ ,  $x=0.25L$ ,  $0.5L$ ,  $0.75L$  and  $L$ , where  $L$  is the length of the bed, are written to the file at time increments of 0.1 seconds. However, the program is easily altered to provide the temperature at any location and time. To allow easier comparison between simulations with different parameters, the time,  $t$ , and temperature,  $T$ , can both be written in non-dimensional form as follows:

$$t_{\text{non-dim}} = \frac{\dot{m}_f c_{pf} t}{m_s c_{ps}} \quad (5.4)$$

$$T_{\text{non-dim}} = \frac{T - T_{\text{initial}}}{T_{\text{inlet}} - T_{\text{initial}}} \quad (5.5)$$

The files are written in a format that is compatible with the computer-graphing program TecPlot [63]. The total heat transfer area, the heat transfer coefficient, and the Ntu (number of heat transfer units) are also provided as output.

## 5.2 Solution Techniques

### 5.2.1 Discretization of Solid Equation

The differential equation for the solid, equation (5.2), follows the general form for unsteady one-dimensional conduction as given by Patankar [64].

$$\rho c \frac{\partial T}{\partial t} = \frac{\partial}{\partial x} \left( k \frac{\partial T}{\partial x} \right) + S \quad (5.6)$$

where  $S = S_C + S_P T_p$  is the source term.

Patankar also describes a finite volume method for discretizing the unsteady one-dimensional heat conduction.

### 5.2.1.1 Fully Implicit Finite Volume Technique

In the fully implicit finite volume technique, the regenerator bed is divided into a number of nodes and control volumes as shown in Figure 5.1. In actual simulations there will be far more divisions.

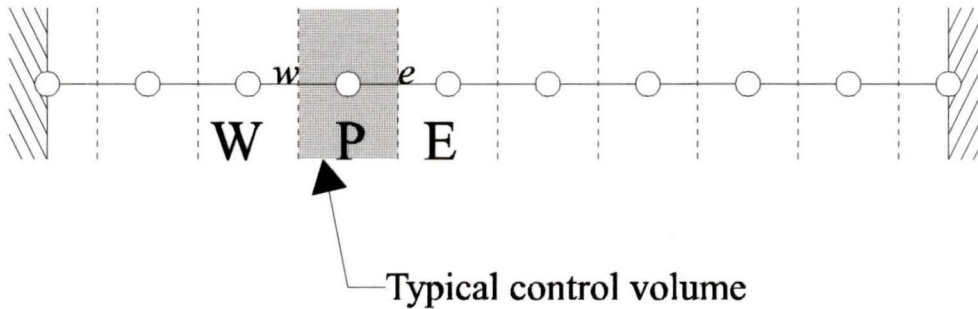


**Figure 5.1: Nodes and corresponding control volumes along regenerator bed**

P, E, and W are all nodes with E and W referring to the points east and west of the point being evaluated, P. The control volume faces are similarly designated  $e$  and  $w$  for the faces on the east and west side of point P. To find the value of the temperature at point P, equation (5.2) is integrated over the control volume with respect to both time and space.

$$\rho_s c_{ps} \int_w^e \int_t^{t+\Delta t} \frac{\partial T_p}{\partial t} dt dx = \int_w^e \int_t^{t+\Delta t} \frac{\partial}{\partial x} \left( k_s \frac{\partial T_p}{\partial x} \right) dt dx + \int_w^e \int_t^{t+\Delta t} S dt dx \quad (5.7)$$

$T_p$  is the temperature of the solid at point P. For the integration of  $\partial T/\partial t$ , it is assumed that the temperature  $T$  prevails over the entire control volume. The integration with respect to  $x$  is done differently. A step-wise profile such as that used for the time step could be applied but it is more accurate to use a piecewise-linear approach in which the temperature is averaged over the control volume.

A fully implicit solution assumes that at time  $t$ ,  $T$  changes suddenly to its new value and remains at that value for the whole time step. This means that  $T_p$  is related to the unknown temperatures  $T_E$  and  $T_W$  and a set of simultaneous equations is necessary. The advantage to the implicit formulation is that the solution is unconditionally stable and therefore the solution will always be physically realistic.

The general form of the discretized equation for a fully implicit solution is as follows [64]:

$$a_p T_p = a_E T_E + a_W T_W + b \quad (5.8)$$

$$a_E = a_W = \frac{k}{\Delta x} \quad (5.8a)$$

$$a_p^o = \frac{\rho c \Delta x}{\Delta t} \quad (5.8b)$$

$$b = S_C \Delta x + a_p^o T_p^o; \text{ where } ^o \text{ denotes the previous time step} \quad (5.8c)$$

$$a_p = a_E + a_W + a_p^o - S_p \Delta x \quad (5.8d)$$

This formula can then be used to solve equation (5.2) as follows:

$$a_p T_p = a_E T_E + a_W T_W + b \quad (5.9)$$

$$a_E = a_W = \frac{k_s}{\Delta x} \quad (5.9a)$$

$$a_p^o = \frac{\rho_s c_s \Delta x}{\Delta t} \quad (5.9b)$$

$$b = \frac{hA_s}{(1-\alpha)V_{\text{reg}}} T_{f,p} \Delta x + a_p^{\circ} T_p^{\circ} \quad (5.9c)$$

$$a_p = a_E + a_w + a_p^{\circ} + \frac{hA_s}{(1-\alpha)V_{\text{reg}}} \Delta x \quad (5.9d)$$

This set of equations is applied to all of the internal nodes.

It is now necessary to consider the boundary conditions. At the entrance to the bed, node 1, there is a heat flux between the fluid and the solid as is shown in Figure 5.2.

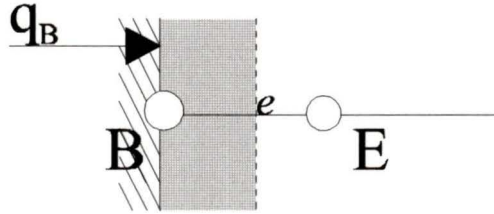


**Figure 5.2: Heat flux at boundary node**

The general form for determining the temperature at point B is:

$$a_B T_B = a_E T_E + b \quad (5.10)$$

$$a_E = \frac{k}{\Delta x} \quad (5.10a)$$

$$b = S_C \frac{\Delta x}{2} + \frac{a_B^{\circ}}{2} T_B^{\circ} + h T_{f,B} \quad (5.10b)$$

$$a_B = a_E - S_P \frac{\Delta x}{2} + \frac{a_B^{\circ}}{2} T_B^{\circ} + h \quad (5.10c)$$

where for the specific equation given in (5.2)

$$S_C = \frac{hA_s}{(1-\alpha)V_{\text{reg}}} T_f \quad \text{and} \quad S_P = -\frac{hA_s}{(1-\alpha)V_{\text{reg}}} \quad (5.11)$$

Similarly, for node n

$$a_n T_n = a_w T_w + b \quad (5.12)$$

$$a_w = \frac{k}{\Delta x} \quad (5.12a)$$

$$b = S_C \frac{\Delta x}{2} + \frac{a_n^o}{2} T_n^o + h T_{f,n} \quad (5.12b)$$

$$a_n = a_w - S_P \frac{\Delta x}{2} + \frac{a_n^o}{2} T_n^o + h \quad (5.12c)$$

Because the implicit equations are written in terms of the unknown temperatures at the current time step, a set of simultaneous equations for nodes 1 through n must be solved. The equations form a tri-diagonal matrix that must be evaluated at each time step. An algorithm for solving a tri-diagonal matrix was obtained from reference [65].

## 5.2.2 Discretization of Fluid Equations

The addition of a flow field in equation (5.2) makes the discretization of the fluid equations a little more complex than the solid equations because the conduction and convection terms are inseparable. If a piece-wise linear profile, such as was used for the conduction terms in the previous section, is used for the convective term as well, it is possible for the solution to become unstable. To overcome this problem, other solution techniques have been developed. One of the most common is the upwind scheme, also known as the upwind-difference scheme, or the donor cell method.

### 5.2.2.1 Upwind Scheme

In the upwind scheme the diffusion term is calculated in the same manner as in the previous section. The convective term is determined by assuming that the value of  $\rho u$  at a control volume face is equal to the value of  $\rho u$  at the grid point on the upwind side of

the face. Therefore integrating over the control volume  $w-e$  and gives the general discretized form [64]:

$$a_p T_p = a_E T_E + a_W T_W + b \quad (5.13)$$

$$a_E = \frac{k}{c\Delta x} \quad (5.13a)$$

$$a_W = \frac{k}{c\Delta x} + \rho u \quad (5.13b)$$

$$b = S_C \Delta x \quad (5.13c)$$

$$a_p = a_E + a_W + S_P \Delta x \quad (5.13d)$$

For equation (5.1),

$$S_C = \frac{hA_s}{\alpha V_{reg} c_{pf}} T_s \quad \text{and} \quad S_P = \frac{hA_s}{\alpha V_{reg} c_{pf}} \quad (5.14)$$

From these equations a set of equations for nodes 2 to n-1 can be written.

For nodes 1 and n the boundary conditions must be considered. The temperature to the west of node 1,  $T_{inlet}$ , is known. The temperature to the east of the node n is assumed to be the same as the temperature at node n. This allows a set of simultaneous equations to be written for nodes 1 through n. As with the solid equations, this set of equations form a tri-diagonal matrix which is solved using the TDM algorithm from reference [65].

### 5.3 Model Validation

Elliot [62] gives tables of results from model simulations for various Ntu and  $\lambda$  from previous works and these have been used to validate the model developed for this thesis.  $T_f^*$  and  $t^*$  are the non-dimensional fluid temperature and non-dimensional time respectively.  $\lambda$  is defined as  $k_s A_{cs} L / \dot{m} c_{ps}$ .

**Table 5.1: Comparison of model results with previous works [62]**

$T_r^*$	$t^*/Ntu$			
	Creswick	Handley & Heggs	Elliott	This Work
<b>Ntu=8, <math>\lambda=0.1</math></b>				
0.1	2.773	2.770	2.768	2.763
0.2	3.897	3.884	3.890	3.886
0.5	6.902	6.839	6.889	6.888
0.8	11.450	11.286	11.427	11.436
0.9	14.629	14.380	14.547	14.615
<b>Ntu=8, <math>\lambda=1.0</math></b>				
0.1	1.588	1.527	1.588	1.561
0.2	2.519	2.380	2.464	2.475
0.5	5.450	5.438	5.785	5.836
0.8	12.566	11.312	12.198	12.332
0.9	14.575	15.755	17.048	17.244
<b>Ntu=16, <math>\lambda=0.1</math></b>				
0.1	7.091	7.010	7.027	7.023
0.2	9.056	8.929	8.985	8.989
0.5	14.244	13.953	14.143	14.171
0.8	21.949	21.403	21.818	21.887
0.9	27.290	26.538	27.121	27.210
<b>Ntu=16, <math>\lambda=1.0</math></b>				
0.1	3.669	3.206	3.394	3.426
0.2	5.609	4.739	5.138	5.212
0.5	12.851	10.162	11.504	11.757
0.8	26.885	20.522	23.783	24.394
0.9	37.484	28.357	33.070	33.952

As can be seen from Table 5.1, the model results lie within the results from other researchers and all the results correlate closely.

## 6. Experimental Apparatus

---

An apparatus was constructed for testing regenerators using the differential test method described in section 4.3. The specifications were that the apparatus have the ability to:

- produce a sudden, sharp change in temperature of the gas entering the regenerator bed
- monitor the temperature change at various positions along the apparatus at intervals no greater than one second
- measure the pressure drop across the regenerator
- have control over the pressure and mass flow rate of the gas

The final apparatus is shown in Figure 6.1.

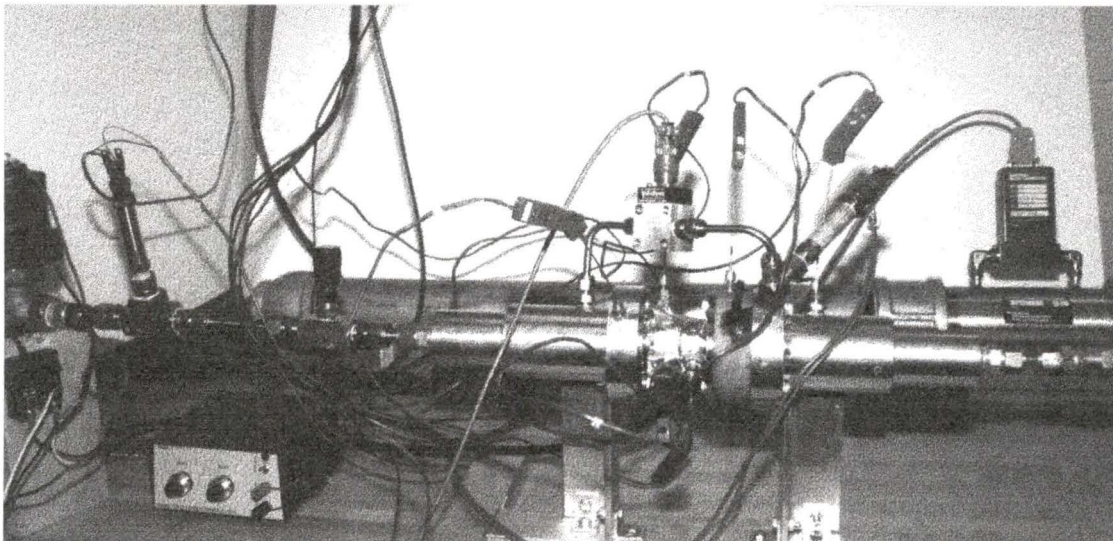


**Figure 6.1: Photograph of completed test apparatus**

The main components, which are labelled in Figure 6.2 and will be described in detail in the following sections, are the regenerator housing, the flow system, the temperature control and the data acquisition system.

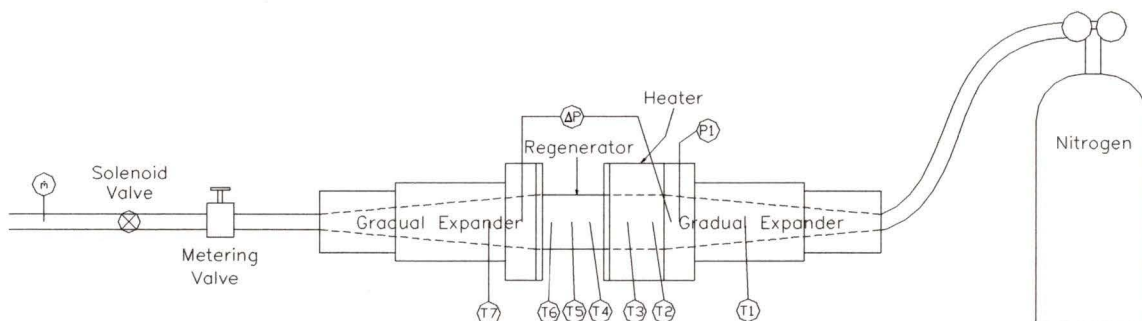


**Figure 6.2: Process instrumentation diagram**

## 6.1 Regenerator Housing

The housing for the regenerator bed is shown in Figure 6.3.

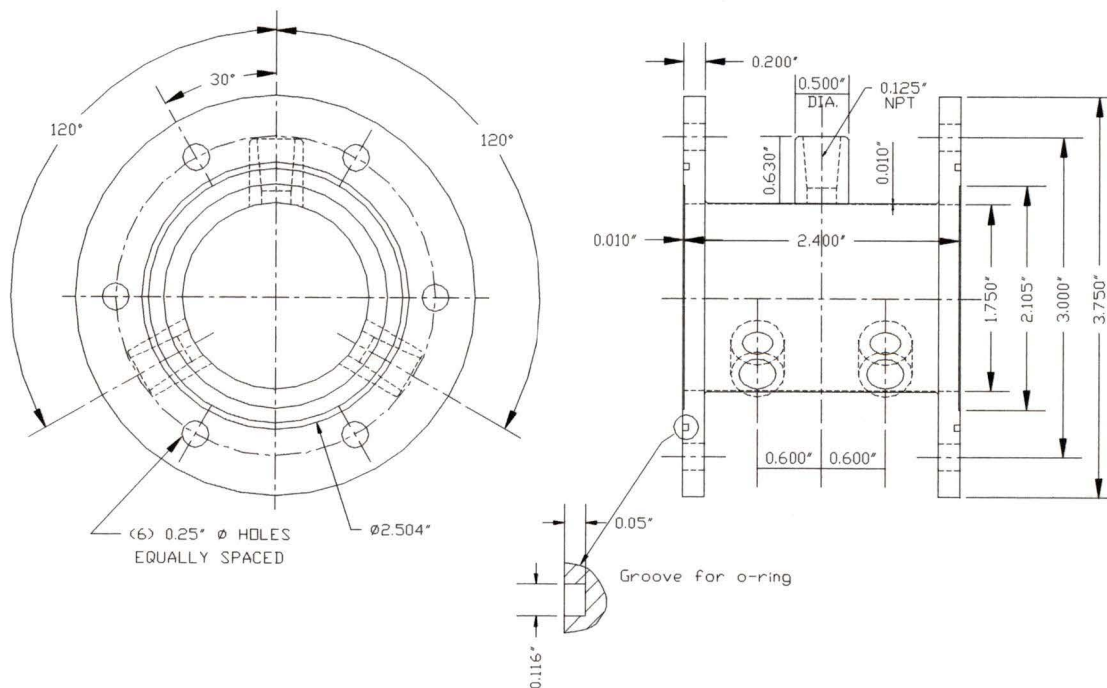


**Figure 6.3: Front and side views of the titanium regenerator housing**

The container is made of thin-walled titanium to reduce the amount of thermal conduction down the walls and to limit thermal mass considerations. The bed has a diameter of 4.37cm (1.75”) and a length of 6.1cm (2.4”). There are three ports welded to the side of the housing for inserting thermocouples into the test bed.

## 6.2 Flow System

The flow system provides a steady, even flow of pressurized gas to the regenerator bed and controlled both the pressure and the flow rate during the experiments. Nitrogen was used as the working fluid and was supplied to the apparatus from a pressurized cylinder. A two-stage regulator (BC Welding Supplies model#R77-500-580) was used to control the gas pressure. In a two-stage regulator, the first stage decreases in pressure as the cylinder empties. This maintains a more constant pressure at the exit of the second stage than would be possible with a single stage regulator. This regulator has an output range of 0-500 psi.

It was necessary to ensure that the regulator would not restrict the flow rate of the system. Figure 6.4 shows the maximum flow rate at a given delivery pressure. The operating pressure of the experiments was 1380 kPa (200 psi), which corresponds to a maximum flow rate of 2000 CFH (cubic feet/hour) or approximately 0.24 kg/s. This is much larger than the maximum flow rate used in the experiments.

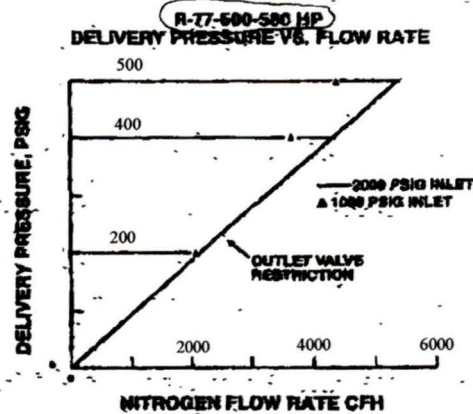


**Figure 6.4: The maximum possible flow rate from the pressure regulator at various delivery pressures**

The flow rate was controlled by a metering valve (HOKE model #2331 F4B) with a twenty turn micrometer handle (model #2300 K1). This metering valve has a cv factor of 0.69 cm (0.27") in the fully open position. The relationship between cv, operating pressure and flow rate is given by:

$$SCFH = 1360cv \sqrt{\frac{\Delta P}{(460 + T)} \frac{P_1}{SG}} \quad (6.1)$$

where: SG is the specific gravity (= 1.09 for nitrogen), T is the operating temperature in Fahrenheit and the pressure is in psi.

As the metering valve is closed, the cv factor decreases, thereby restricting the amount of flow that can move through the apparatus in a given amount of time. The relationship between cv and number of turns is given in Figure 6.5. After 20 turns of the handle, the metering valve is fully open.

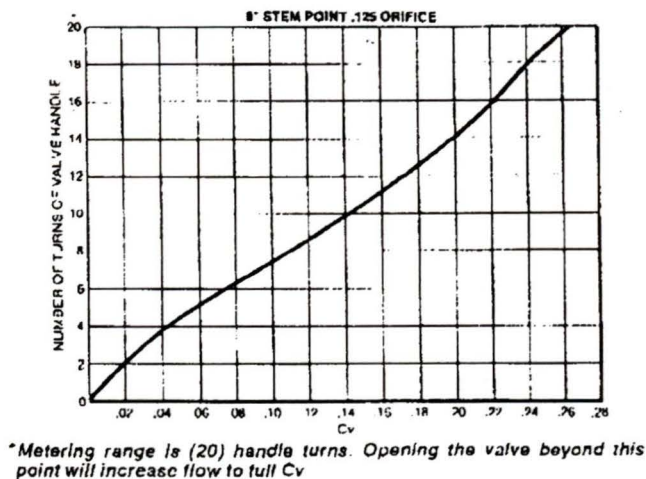


**Figure 6.5 : cv factor as a function of the number of turns of the metering valve**

The metering valve is located downstream of the regenerator bed because of the large pressure drop across the valve.

The pressure regulator and metering valve combination control the pressure and flow rate of the gas. However it is still necessary to ensure that the gas entering the regenerator is as free as possible of recirculation eddies or other flow maldistributions. The major potential source of flow disruption is the sudden expansion from the half-inch diameter pipe leading from the pressurized cylinder to the 1.75-inch diameter heater. To provide a more gradual expansion, conical expanders were placed before and after the regenerator/heater assembly. However, during preliminary testing of the apparatus, some strange results were generated. It was suspected that the angle of the gradual expansion was still too steep and that some flow recirculation was occurring. To solve this problem, fifteen 100 mesh stainless steel screens were placed after the expansion and before the heater. These screens helped to cut down any eddy effects in the flow and ensured a more uniform radial distribution of heat after the heater.

### 6.3 Temperature Control

A key aspect of the experimental apparatus is the need for a sudden change in temperature. The different ways in which this has been accomplished in the past were discussed in section 4.3.1. A combination of flow switching and a fast response heater was used in this apparatus.

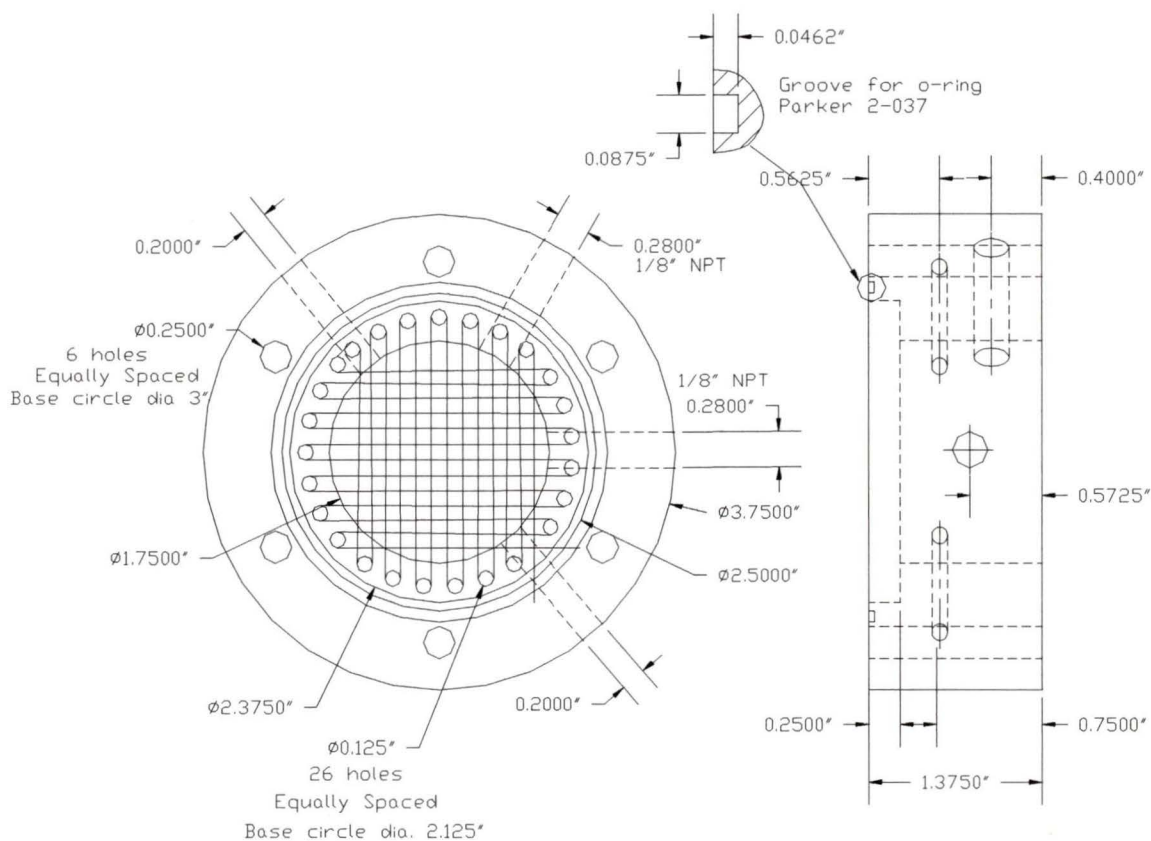


**Figure 6.6: Schematic of the front and side views of the fast response heater**

A schematic of the heater is shown in Figure 6.6. The housing is constructed of G10, which is a fiberglass epoxy composite and therefore has a low thermal conductivity. This was used to reduce the amount of heat being conducted into the heater walls instead of transferred to the gas flow. 0.25 mm (0.01") diameter nichrome wire was wrapped around a series of phenolic posts in a cross-wise pattern as can be seen in Figure 6.6. Five twisted pairs were used for a total of ten wires connected in parallel. Connecting the

wires in parallel reduced the amount of current carried by each wire and therefore, because there is a limit to the amount of current a wire can safely carry, the maximum power output of the heater was increased. The ends of the nichrome wires were soldered to two 14 gauge copper wires that were used as the power supply leads. The lead holes were then sealed with epoxy. A Powerstat variable autotransformer (variac) #3PN136B (0-140V, 0-20A) was used to provide power to the heater. This variac can provide a power range of 0 to 100% of the voltage from the wall outlet. This corresponds to 0-144VAC.

The heater power is related to the mass flow rate as follows:

$$P_{\text{flow}} = \dot{m}c_p\Delta T_f \quad (6.2)$$

$$i_{\text{required}} = \sqrt{\frac{P_{\text{flow}}}{R_{\text{heater}}}} \quad (6.3)$$

$$V_{\text{required}} = i_{\text{required}} (R_{\text{heater}} + R_{\text{leads}}) \quad (6.4)$$

$$V_{\text{variac}} = \frac{V_{\text{required}}}{1.44} \quad (6.5)$$

If a fluid is moving over the wires and cooling them down, it takes longer for the wires to heat up enough to cause a 10° change in the temperature of the gas. To decrease this response time, a normally closed solenoid valve (Magnatrol model #18A52G) was inserted downstream of the metering valve. This valve made it possible to pressurize the system, turn the heater on and then quickly start the flow. By allowing the heater wires to heat up before turning on the flow, a very sharp change in temperature was introduced at the entrance to the bed. The valve is rated for a maximum upstream to downstream pressure difference of 300 psi and does not require a minimum pressure difference to operate. It also has a high cv factor to ensure that the metering valve is the only place where the flow is restricted. It is activated using an on/off switch wired to a Potter & Brumfield solid-state relay (model #SSR-240D25R).

The response time of the heater was measured at various mass flow rates. The curves can be represented by:

$$T(t) = T_{\text{initial}} + (T_{\text{final}} - T_{\text{initial}})(1 - \exp(-t_h t)) \quad (6.6)$$

where  $t_h$  is the change in temperature per second and varies with the mass flow rate as follows:

$$t_h = 1.23 + 5.33e10 * m^{5.95} \quad (6.7)$$

Figure 6.7 shows the temperature change that is introduced into the flow at various mass flow rates. The curve is more gradual at low flow rates, however at low flow rates the bed takes longer to reach steady state and therefore the ratio of the time for the initial temperature change to the total time of the run is not much different.

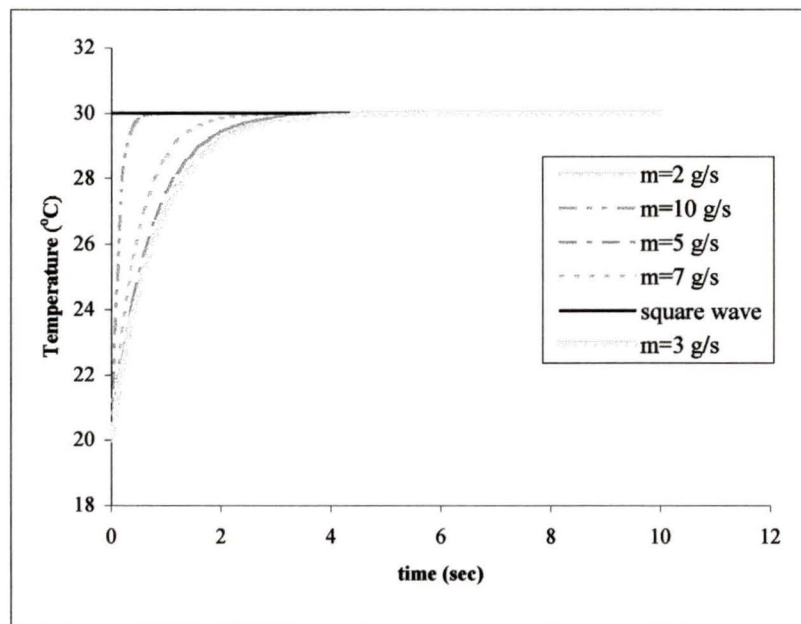


**Figure 6.7: Heater response time at various mass flow rates**

## 6.4 Instrumentation

### 6.4.1 Mass Flow Meter

The mass flow was measured downstream of the bed using a Hastings (model #HFM-200B) flow meter with a laminar flow element (model # LS-3B). In this meter, a known percentage of the gas is removed from the flow and passed over a heater. The temperature of the fluid is measured before and after this heater and the difference used to calculate the mass flow rate of the sample.

$$\dot{m} = \frac{\dot{Q}}{c_p \Delta T} \quad (6.8)$$

Because equation (6.8) depends on the specific heat of the fluid being used, it is necessary to calibrate the meter with the same type of fluid as it will be measuring. The flow meter was calibrated using Nitrogen by Hastings. It has a range of 0-1125 SLM which for Nitrogen corresponds to a range of 0-21 g/s, provides an accuracy of  $\pm 0.4\%$  of full scale and has a linear output of 0-10 VDC.

Because the laminar flow element is 3" in diameter, it was necessary to provide a straight section of 3" diameter pipe both before and after the flow meter. This was to ensure that flow had returned to laminar after the expansion from the half-inch pipe. The manufacturer recommended a length of pipe 3 times the pipe diameter before the meter and 1.5 times the pipe diameter after. The flow was measured downstream of the regenerator because of the large pressure drop across this part of the apparatus.

### 6.4.2 Pressure Transducer

The pressure drop across the regenerator was measured using a Validyne differential pressure transducer (model #DP15-46-N-1-S-4-A). This transducer has a range of 0-50 psi with an accuracy of 0.25% of full scale. Because the output of the transducer is an ac

voltage, a carrier demodulator (model #CD15-A-1-A-1), which converts the ac voltage to a linear 0-10V dc output was also purchased. The combined transducer and demodulator system was calibrated by Validyne.

The absolute pressure upstream of the regenerator bed was measured using an OMEGA absolute pressure transducer (model #PX613). This transducer has a range of 0-500 psia with an accuracy of 0.4% full scale. It would have been possible, and less expensive, to measure the pressure drop across the regenerator bed by installing a second absolute pressure transducer downstream of the bed. However this decreases the accuracy of the measurements significantly. Instead of the  $\pm 0.125$  psi precision given by the Validyne transducer, a precision of only  $\pm 4$  psi would be obtained by taking the difference of two absolute pressure measurements.

#### **6.4.3 Temperature Sensors**

The most important requirements for the temperature sensors were an accuracy of less than 0.3 °C and more importantly a high level of repeatability, as well as a response time of less than a second. Exposed junction thermocouples were used because they are self-exciting, easy to use, relatively durable and have acceptable performance. There are seven type E exposed junction probes (OMEGA model #GEMQSS-062E-6) located along the apparatus as shown in Figure 6.2.

- T1 measures the temperature of the gas prior to entering the heater.
- T2 monitors the temperature of the heater wires. This is a safety check to ensure that the maximum allowable wire temperature is not exceeded.
- T3 records the temperature of the gas immediately after the heater.
- T4, T5 and T6 measure the temperature inside the regenerator bed at intervals of approximately a quarter of the length of the bed.
- T7 monitors the temperature of the gas after it has left the bed.

All of the thermocouple junctions are located in the centre of the gas flow. The thermocouples were calibrated by placing them in sequentially an ice bath and a boiling water bath and comparing the temperatures measured. Because it is the temperature change over time at various positions in the bed that is being measured, it is more important that all the thermocouples are reading the same temperature repeatedly than that the absolute temperature is correct. It was found that for both the ice bath and the boiling water bath the thermocouple readings were consistently within  $\pm 0.2^\circ\text{C}$  of each other for a series of trials.

Thermocouples produce a non-linear voltage. The National Institute for Standards and Technology (NIST) has produced curves and tables for converting this voltage output into units of temperature for each thermocouple type [66]. From the table for type E thermocouples, a curve for temperature vs. voltage was produced for a range of  $10\text{-}60^\circ\text{C}$ . Because the experiments were performed at room temperature, the temperature never exceeded this range. A commercial curve-fitting program, TableCurve 2D [67] was used to determine the equation of the temperature-voltage curve.

The temperature readings from T7, downstream of the regenerator housing, were found to take much longer than expected to reach the steady state temperature achieved at the positions within the regenerator bed. Thermocouple T7 is located inside the aluminum gradual contractor. This piece has a very high thermal mass and it is suspected that too much heat is being lost to the aluminum for accurate readings to be obtained from T7. Therefore, only the thermocouple readings at the three positions within the regenerator bed were considered when analyzing the results. It is theoretically possible to obtain information about the heat transfer in the bed by measuring the temperature at only one location, therefore measuring the temperature at three positions in the bed is more than sufficient.

#### 6.4.4 Data Acquisition System

All of the transducers discussed in the above sections are connected to the Labview 4.0 [68] data acquisition system. A schematic of this set-up is shown in Figure 6.8.

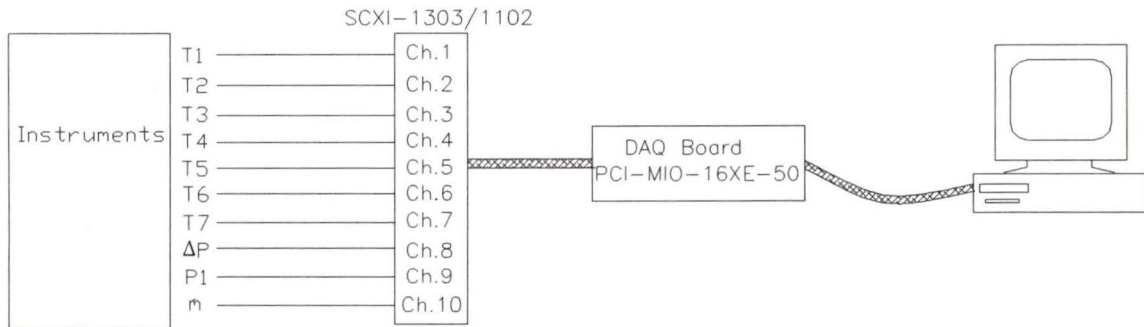


**Figure 6.8: Schematic of data acquisition system**

The outputs of the instruments discussed in the previous sections are connected to separate channels in the SCXI-1303 terminal block. This is in turn connected to the SCXI-1102 module. The amplified signals are then sent to the data acquisition board. The data are converted to the appropriate engineering units and written to both the screen and a specified file.

The SCXI-1303 terminal block was designed specifically for thermocouples. It is isothermal which allows the same reference temperature to be used for all the channels. It also contains a thermistor to measure the reference temperature of the block.

Labview allows gains to be set for the DAQ board and also for each channel. The maximum allowable gain for the PCI-MIO-16XE-50 board is found as follows:

$$\text{Gain} = \frac{20\text{V}}{\text{maximum voltage to be measured}} \quad (6.9)$$

where 20V is the range of the board.

For the pressure transducers and the mass flow meter the output voltage range is 0-10V. Therefore the maximum allowable gain is 2. For the thermocouples however, the voltage being measured is on the order of  $\mu\text{V}$ . Therefore it is possible to set the gain to 200, which is the maximum possible for the equipment being used. The gain of the board was therefore set to 2 and the gain for the thermocouple channels set to 100. The other channels were left at the default gain of 1. The resolution of the readings can be calculated as:

$$\text{resolution} = \frac{20\text{V}}{\text{Gain} \times 2^{16}} \quad (6.10)$$

The resolution of the board is  $1/2^{16}$ . For a gain of 1, the resolution would be 0.3mV. Since the average voltage change/degree is  $59\mu\text{V}$  for E-type thermocouples, this would not provide very precise results. However by setting the gain to 200, the resolution becomes  $1.5\mu\text{V}$  and the results become much more precise. For a gain of one, the error in the readings would be approximately 23% while with a gain of 200, the error would be only 0.027%. To reduce the effects of noise each channel is read 50 times at each reading interval and the results averaged. A reading is taken every 0.5 seconds.

Labview 4.0 [68] was used to write a program to read the different channels, convert the readings into the appropriate engineering units and then record them as a function of time. The results from the experiment are written both to a display window on the computer screen and to a specified file. The display window also acts as a control panel and allows the user to vary the frequency of the readings, the number of readings to be taken and averaged and the name of the output file.

## 6.5 Regenerator Bed Fabrication

### 6.5.1 Spheres

Manufacturing spheres can be a complicated and expensive process. Therefore, commercially available stainless steel and copper spheres were purchased. The particle diameter range was narrowed down to 212  $\mu\text{m}$  – 250  $\mu\text{m}$  by pouring the spheres into a series of sieves and then vibrating them on a shaker table.

The next step was to pack the spheres into the regenerator bed. One end of the regenerator housing was blocked by a 100 mesh copper screen. The screen had been soldered to a flat brass ring and this piece was bolted between the housing and the heater. Next, the spheres were poured into the open end of the housing. The bed was constantly vibrated during the pouring process to reduce the chance of channeling or vacancies within the bed. Because the housing was filled in a vertical position but tested in a horizontal position it was important for the bed to be completely full. Otherwise the particles would redistribute themselves and open a flow channel along the top of the regenerator. By filling until the bed was slightly overflowing, this problem was avoided. A second copper screen was bolted between the housing and expander to keep the bed in place. The pressure applied when the pieces were bolted together caused the overflow to be packed down into the bed.

Two regenerator beds were constructed using the method described above. One contained stainless steel spheres with an average particle diameter of 231 $\mu\text{m}$ . The other consisted of the same size of copper particles. The porosity of these beds was calculated as follows:

$$(1 - \alpha) = \frac{m_{\text{particles}}}{\rho_{\text{particles}} V_{\text{reg}}} \quad (6.11)$$

The density of the particles and the volume of the regenerator are both known. The mass of the particles in the bed was measured. The porosity was found to be approximately 0.35 for both the copper and stainless steel beds. This is in agreement with the literature, which predicts a porosity of 0.35 to 0.4 for spherical particles [18].

### 6.5.2 Flakes

The flakes were constructed from ribbons of amorphous materials, specifically a combination of gadolinium and cobalt,  $Gd_{65}Co_{35}$ . These materials were developed as part of a CFS research project on magnetic materials sponsored by Natural Resources, Canada. The normal manufacturing procedure for these materials produces thin strips or ribbons of the material. The ribbons were manufactured into a regenerator bed by crushing the ribbons into flakes and then packing the flakes into the regenerator housing.

The flakes were crushed using the ball mill shown in Figure 6.9. Ribbons and ceramic balls were inserted into the container shown.

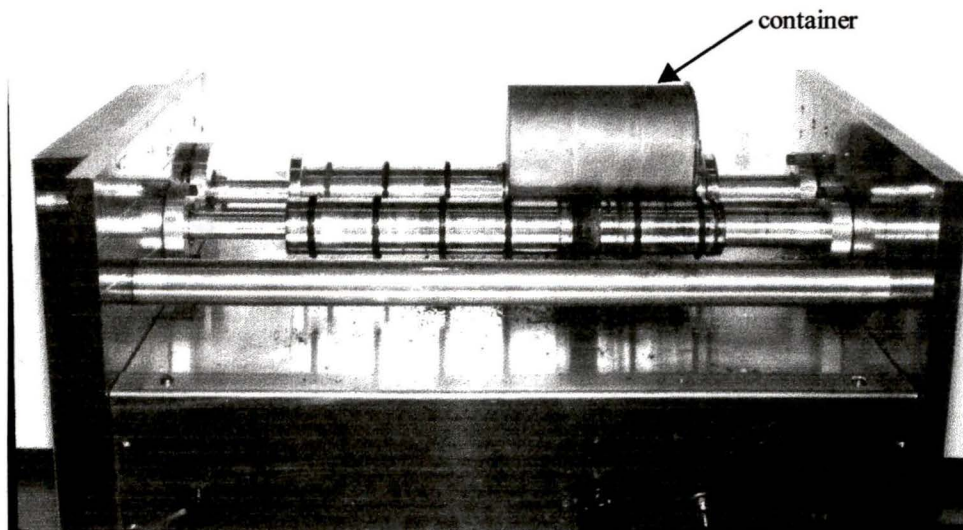


**Figure 6.9: Ball mill for producing metallic flakes**

The ball mill rotated the container and the balls pounded the ribbons into flakes. The flakes were then sorted using a series of sieves on a shaker table. To get enough material to fill the regenerator housing, a particle size range of 212-450  $\mu\text{m}$  was used.

The flakes were packed into the regenerator housing in the same manner as described above for the spheres. Vibrating the bed in a vertical position as it was being filled most likely caused the particles to settle so that generally the largest face was perpendicular to the flow.

Because the flakes are not constructed from well-characterized materials, it was necessary to determine the density before using equation (6.11) to calculate the porosity of the bed. A known mass of flakes was put into a graduated cylinder containing a known volume of acetone. Then the displacement of the acetone was read on the graduated cylinder. Dividing the mass of flakes by the displacement volume gave a value for the density. This test was conducted five times and the results averaged to provide a more accurate estimate. The density was found to be approximately  $8.2 \text{ g/cm}^3$ . The porosity of the flake bed was calculated, using equation (6.11), and found to be approximately 0.62. This is much higher than that of the sphere bed.

### 6.5.3 Wires

To achieve a very low porosity regenerator, it was necessary to find a way to pack the wires into the bed with a fair amount of precision. For example, in Figure 6.10 the porosity of configuration a) is approximately twice that of configuration b).

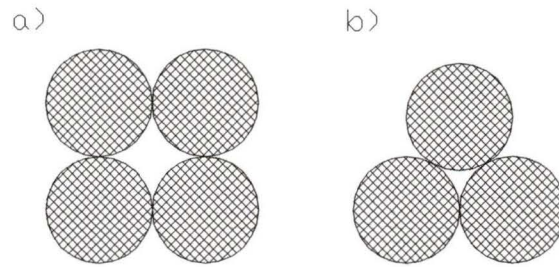


**Figure 6.10: Possible configurations for cross-section of wire bed: a) box wire configuration b) triangle wire configuration**

Through some trial and error it was discovered that it was much easier to obtain the configuration shown in Figure 6.10b when the wires were packed into a container with straight sides as opposed to a cylinder. Therefore, a plastic container with a hexagonal inner cross-section and a circular outer cross-section was made. It was not easy to buy a plastic tube with this configuration so a mould was constructed according to Figure 6.11 and the plastic piece cast using a polyester resin.

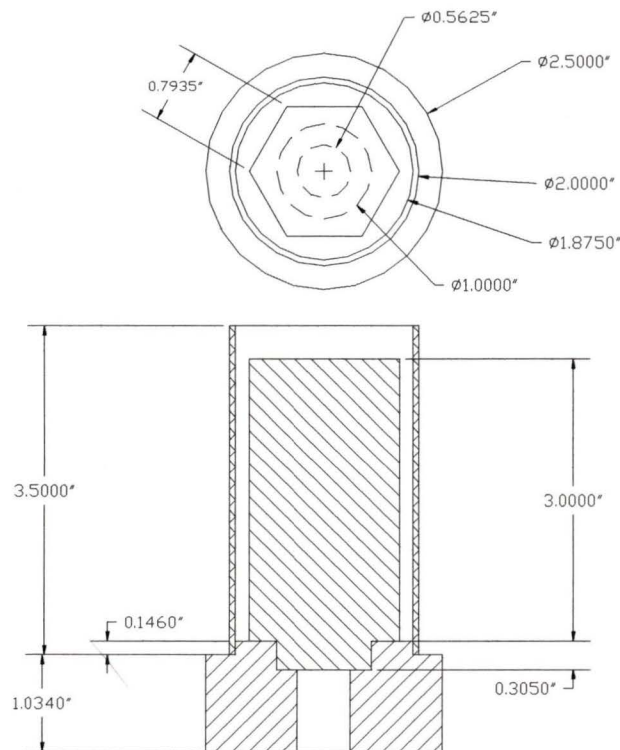


**Figure 6.11: Stainless steel mould for casting plastic tube**

The polyester by itself was found to be too brittle to withstand any machining. A much stronger piece was cast by adding continuous strands of fibreglass to the mould while pouring in the resin.

Initially, 0.027" (686  $\mu\text{m}$ ) diameter wire was purchased on a 1.5 foot spool. Even though a fairly large diameter spool was used, the radius of curvature of the wire when cut into 10cm (4 inch) long pieces was still too large for the wires to be packed tightly into the plastic piece. Therefore straightened wires were purchased. The wires were cut into approximately 3500 10cm (4 inch) long pieces and carefully arranged in the plastic container. The container was then cut into four sections using a Buehler Isomet 2000 precision saw. The ends of the sections were lapped using a Buehler Minimet Polisher to ensure that the flow channels were unblocked. The vibration of the polishing process helped to identify any holes or irregularities in the bed. More wires were added to the bed to fill these holes. The pieces were arranged in the titanium regenerator housing as shown in Figure 6.12. Stainless steel, 0.16cm (1/16") diameter wires formed into semi-circular spacers were used to separate the wire sections. The spacers create room for the three thermocouples located between the wire sections. A layer of liquid tape was spread around the edge of each section to force the gas to flow through the wires and not along the walls of the container.

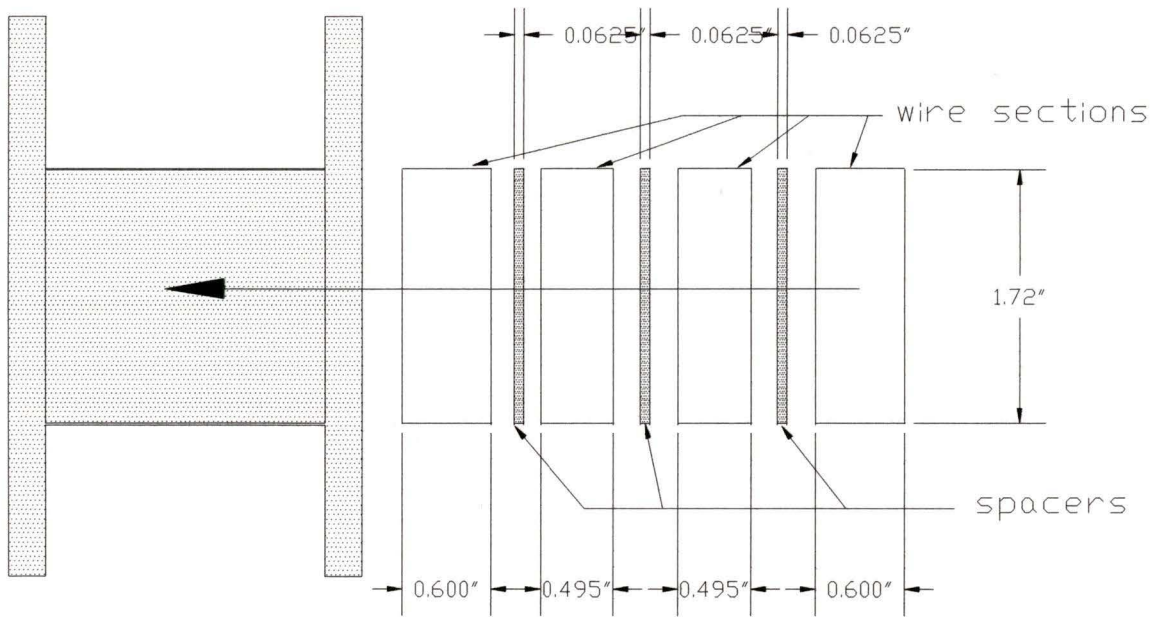


**Figure 6.12: Arrangement of wire sections and spacers in wire regenerator bed**

## 7. Test Results: Analysis and Discussion

---

A set of experiments was conducted for each of the three geometries discussed in the previous sections. For each set of experiments the operating pressure was held constant at 1380 kPa (200 psi) and the mass flow rate varied between approximately 2 and 15 g/s.

The analysis of the pressure drop data was fairly straight forward because the pressure drop across the bed was measured directly during the experiments. A friction factor was calculated from the pressure drop measurements and the results compared to theoretical predictions.

Analyzing the heat transfer data was more complicated because it involved matching the temperature-time profiles recorded during the experiments with similar profiles generated by the model. Figure 7.1 demonstrates the matching process. The temperature-time profiles are a function of the heat transfer coefficient, the fluid thermal conductivity and the solid thermal conductivity. Therefore varying these parameters changes the slope of the curves. Excluding the cases where one of the parameters is zero, there is a single set of values that matches each set of curves. Figure 7.1 shows that for stainless steel spheres with a flow rate of 2 g/s and an operating pressure of 1380 kPa (200 psi), setting  $h=1045\text{ W/m}^2\text{K}$ ,  $k_s=0.4\text{ W/mK}$ ,  $k_f=0.45\text{ W/mK}$  in the model matches the experimental data. If the heat transfer coefficient is too high and/or the conduction too low as in the second case, then the curves will be too steep. Conversely, if the heat transfer coefficient is too low and/or the conduction too high, then the curves will be too flat.

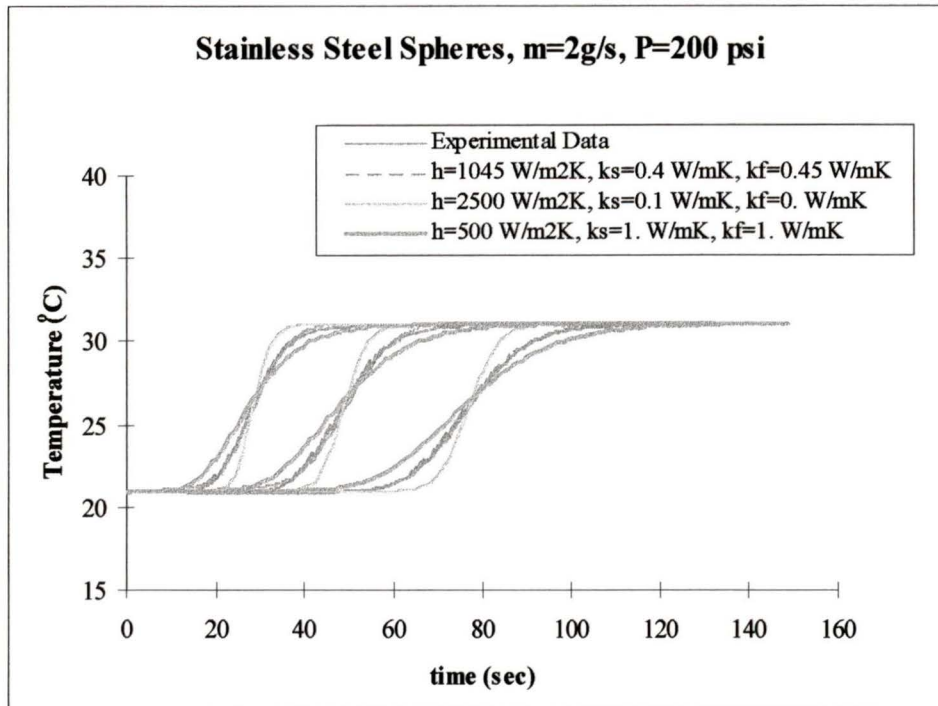


**Figure 7.1: Example of heat transfer data analysis**

An error analysis determined that for an error in the temperature measurements of  $\pm 0.2^\circ\text{C}$ , the heat transfer coefficient, fluid and solid thermal conductivity have an approximate error of  $\pm 15\%$ . The error of the pressure transducer is 0.25% of full scale. This corresponds to an error in the pressure drop data of 0.86 kPa (0.125 psi). A possible source of error in the measurements is the response time of the heater. If the initial temperature change is not steep than the slope of the downstream temperature profiles will decrease and effect the results. As discussed in Section 6.3, the initial temperature profile can be approximated as:

$$T(t) = T_{\text{initial}} + (T_{\text{final}} - T_{\text{initial}})(1 - \exp(-t_h t)) \quad (7.1)$$

where  $t_h$  is:

$$t_h = 1.23 + 5.33e + 10 * m^{5.95} \quad (7.2)$$

It was observed that using this relationship as the inlet curve in the model instead of a square wave did significantly effect the downstream temperature profiles. The slope of the curves remained within the  $\pm 15\%$  error limits.

## 7.1 Spherical Particle Bed

### 7.1.1 Pressure Drop across Sphere Bed

As was discussed in previous chapters, there has been a significant amount of research directed towards characterizing spherical particle beds. Therefore, the spherical particle bed experiments served as a means of validating the test apparatus. If all the systematic errors have been eliminated from the apparatus then the measured results should correspond with the correlations presented in the literature. The pressure drop across the bed is a good indication of whether channeling or other flow maldistributions are occurring within the flow. If the pressure drop is much lower than expected there are most likely channels present in the bed.

The fanning friction factor is often used as a convenient means of comparing pressure drop data. As discussed in Section 3.1.2, the Ergun-Macdonald [29] correlation gives:

$$f \frac{\alpha^3}{(1-\alpha)} = \frac{\Delta PD_{eq}}{\rho v_o^2 L} = \frac{180(1-\alpha)}{Re_o} + 1.8 \quad (7.3)$$

In Figure 7.2 and Figure 7.3 the pressure drop measured across the stainless steel and copper beds respectively is plotted against that calculated using equation (7.3). For both cases, there is close agreement between the measured and theoretical pressure drop even at different operating pressures.

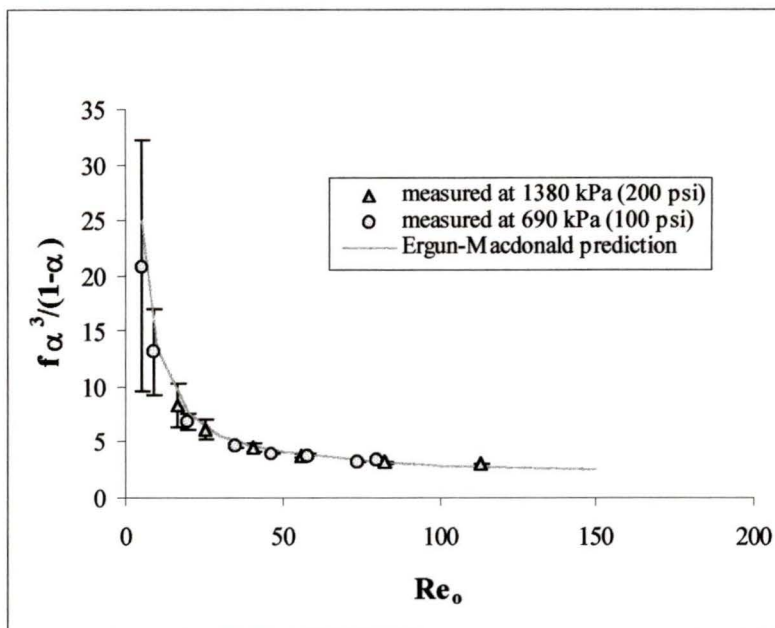


**Figure 7.2: Comparison of experimental results with the Ergun-Macdonald equation for the pressure drop across a bed of stainless steel spheres**

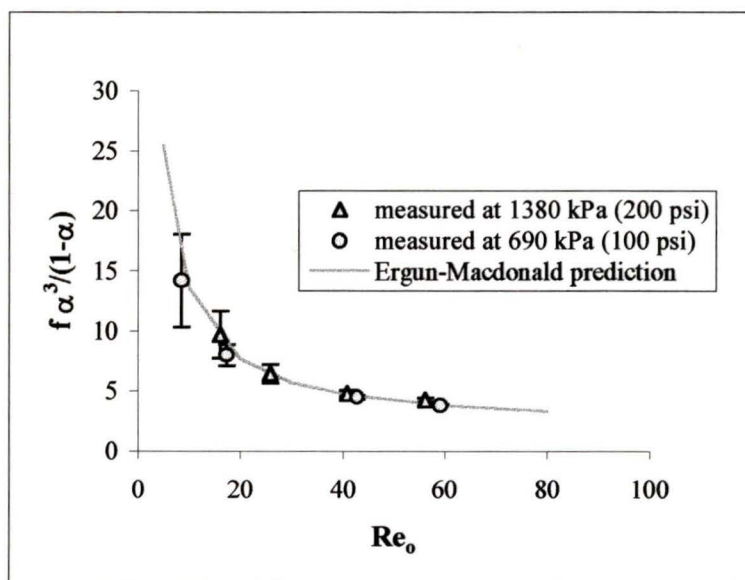


**Figure 7.3: Comparison of the Ergun-Macdonald equation with experimental results for the pressure drop across a bed of copper spheres.**

This agreement means that the bed is free of any significant channeling or other systematic errors that would affect the pressure drop.

### 7.1.2 Heat Transfer Coefficient in Sphere Bed

Figure 7.4 compares the heat transfer coefficient predicted from the Kays and London [21] correlation with the results found from the experimental data. The Kays and London correlation is given as:

$$h = 0.23G_{cp}(\alpha Re)^{-0.33} Pr^{-0.667} \quad (7.4)$$

To match the experimental data using equation (7.4), it was necessary to set the fluid conductivity to zero. Kays and London assumed that the fluid conductivity in the bed was zero and therefore the corresponding loss in effectiveness was attributed to the heat transfer coefficient.

Also plotted in Figure 7.4 is the Wakao correlation, equation (3.3). Wakao [20] adjusted the heat transfer coefficient for the effects of axial thermal conductivity and Figure 7.4 shows that this correlation is fairly close to the experimental data.

A new correlation, which includes the fluid conductivity effects, was found by fitting an equation to the true experimental data:

$$h = 0.5G_{cp}(\alpha Re)^{-0.33} Pr^{-0.667} \quad (7.5)$$

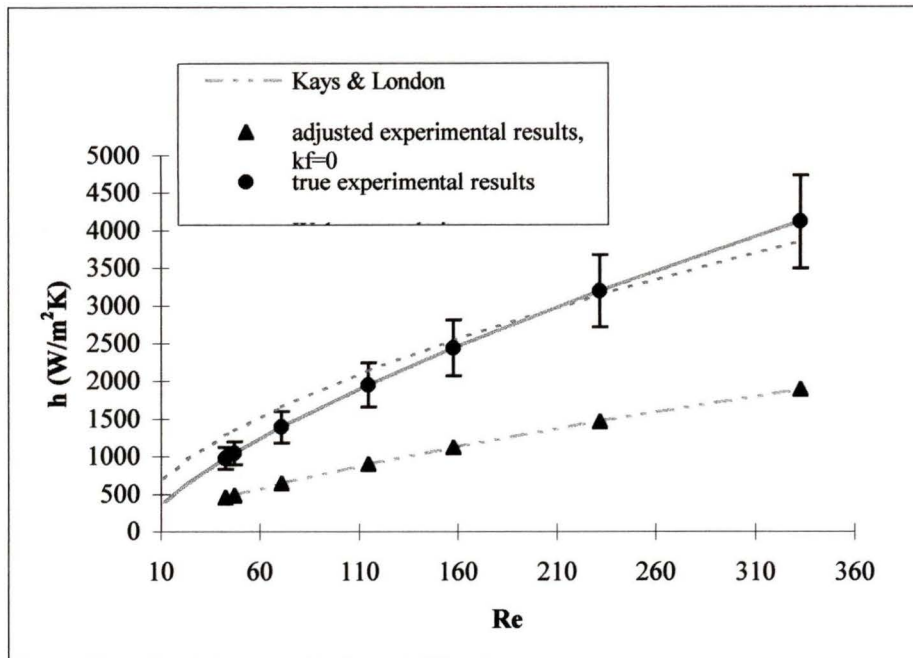


**Figure 7.4: Comparison of Kays and London correlation [21] with experimental data for stainless steel spheres**

Most researchers follow the Kays and London example and do not separate out the fluid conductivity effects. The danger in that method is that the fluid conductivity effects may be accounted for twice in the design process. For example, consider the case where the 2<sup>nd</sup> law analysis method described in Section 2.1.3 is being used as a design tool. If the heat transfer coefficient is calculated from equation (7.4) and the fluid conduction term is not neglected, then the entropy generation due to axial fluid conduction will be included in both the fluid conduction and the finite heat transfer term. The predicted entropy generation will be much higher than in an actual bed and therefore the predicted performance of the bed will be lower. This would be a problem if the objective of the exercise were to compare different geometries.

The results for the copper sphere experiments are shown in Figure 7.5. As would be expected the heat transfer coefficient can be predicted from equation (7.4) or (7.5) depending on whether or not the fluid conductivity is taken into account separately.

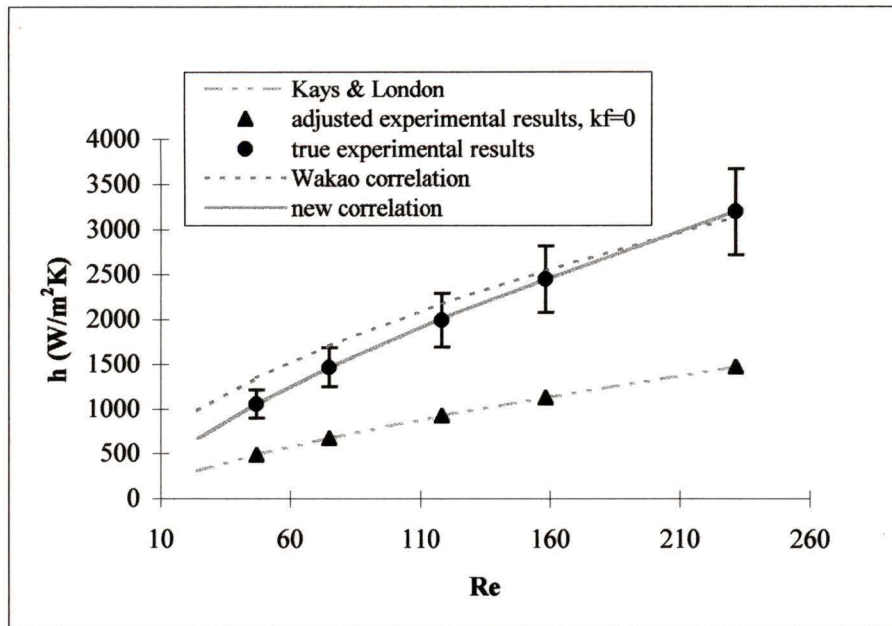


**Figure 7.5: Comparison of Kays and London correlation with experimental results for copper spheres**

### 7.1.3 Thermal Conductivity of the Spheres

The effective solid conductivity was found to be 0.4 W/mK in both the stainless steel and copper beds. The Zehner-Schlunder model predicts 0.45 W/mK for the stainless steel spheres and 0.83 W/mK for the copper spheres. Because copper has a much higher material thermal conductivity than stainless steel, it was surprising that the conductivity of the different particle beds would be the same. However, the point contact between particles acts as a large resistance to heat transfer and may dominate over the thermal conductivity of the material. The presence of oxide layers around the spheres may also reduce the thermal conductivity of the bed. This effect could be further explored by experimenting with other types of spheres to see if the solid conductivity remains constant or else by measuring the thermal conductivity of the beds using an independent experiment.

### 7.1.4 Fluid Thermal Conductivity in the Sphere Bed

The fluid conductivity followed the Edwards-Richardson correlation:

$$k_f = \frac{\rho c_p D_p v_o}{2\alpha} \quad (7.6)$$

The molecular thermal conductivity of nitrogen is 0.026 W/mK. This is much smaller than the eddy diffusivity term for all but very small flow rates and the fluid conductivity can therefore be represented solely by the eddy diffusivity contribution.

## 7.2 Flake Bed

### 7.2.1 Pressure Drop across the Flake Bed

Theoretically, it should be possible to predict the pressure drop across a bed of flakes within about 50% using the Ergun-Macdonald equation and an equivalent diameter calculated from equation (3.2) [29]. To find the equivalent diameter, it was first necessary to know the average flake size. A random sample of fifty flakes was measured under a microscope. The average characteristic lengths were found to be 421  $\mu\text{m}$  and 245  $\mu\text{m}$ . The thickness of the flakes is approximately 40  $\mu\text{m}$ . Using an equivalent diameter of 42  $\mu\text{m}$  was found to give the closest approximation to the Ergun-Macdonald equation. This corresponds to a shape factor of 0.86 as defined by:

$$D_{eq} = \frac{6V_p(1-\alpha)}{A_p\phi_s} \quad (7.7)$$

The small equivalent diameter is an indication that the flakes are mostly aligned perpendicular to the flow as suspected. If the flakes were parallel to the flow then a pressure drop would be expected and therefore a larger equivalent diameter would be necessary to approach the Ergun-Macdonald correlation. The equivalent diameter would

likely be closer to the average of the two large sides. For rough particles, the Ergun-Macdonald correlation is as follows:

$$f \frac{\alpha^3}{(1-\alpha)} = \frac{\Delta P_{D_{eq}}}{\rho v_o^2 L} = \frac{180(1-\alpha)}{Re_o} + 4 \quad (7.8)$$

Figure 7.6 plots friction factor calculated from the experimental results with the values predicted by equation (7.8). The experimental results are within 30% of the Ergun-Macdonald equation. However, a better custom approximation was found to be:

$$f \frac{\alpha^3}{(1-\alpha)} = \frac{110(1-\alpha)}{Re_o} + 8.5 \quad (7.9)$$

This approximation was found by fitting a curve through the experimental data using the TableCurve 2D [67] curve fitting program.

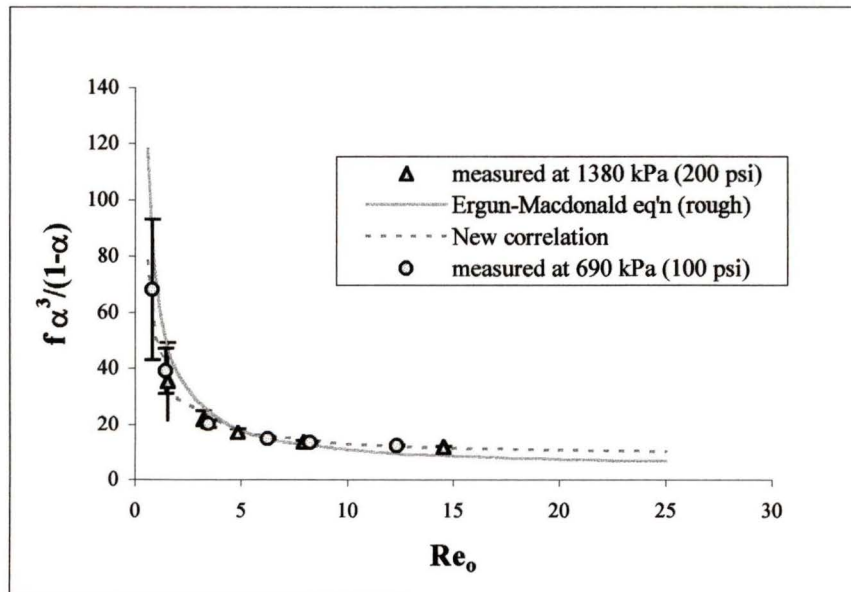


**Figure 7.6: Comparison of the Ergun-Macdonald equation with the experimental results for the pressure drop across a bed of flakes.**

### 7.2.2 Heat Transfer Coefficient in the Flake Bed

For the flake bed, the heat transfer coefficient corresponded with the new heat transfer coefficient correlation, equation (7.5), if the equivalent diameter was taken to be the average of the two large dimensions (333  $\mu\text{m}$ ). This also suggests that the flakes are generally aligned perpendicular to the flow. It is interesting to note that it is necessary to define the equivalent diameter differently for the heat transfer coefficient and the pressure drop. The most probable cause for the discrepancy in equivalent diameters is that the geometry of a flake is too different from that of a sphere for it to be a good approximation. The experimental data are plotted against the theoretical predictions in Figure 7.7.

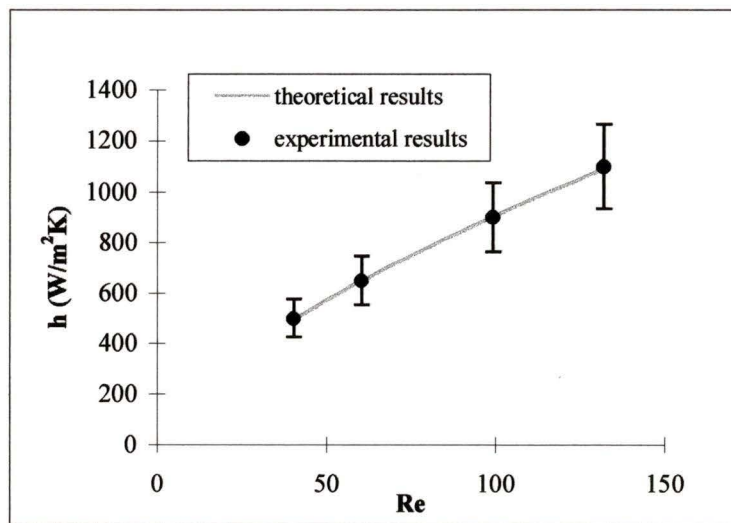


**Figure 7.7: Comparison of experimental and theoretical heat transfer coefficient in flake regenerator bed**

### 7.2.3 Thermal Conductivity of the Flakes

The thermal conduction through the solid matrix was measured as 2 W/mK. The axial conduction through the flakes is higher than through the spheres because the contact area between the flakes is much larger than the point contact present in sphere beds.

### 7.2.4 Fluid Thermal Conductivity in the Flake Bed

There will be eddy diffusivity effects present in the flake bed. If the flakes are mostly oriented perpendicular to the flow as is indicated by the heat transfer coefficient and pressure drop results, then the eddy effects could be quite significant. The experimental results support this. Figure 7.8 compares the experimental data with the Edwards and Richardson correlation, equation (7.6). As with the heat transfer coefficient, an equivalent diameter of 330  $\mu\text{m}$  was used.

At high Reynolds numbers, the experimental results do not agree with the correlation. A new correlation for thermal conductivity in a bed of flakes was fitted to the experimental data.

$$k_f = 0.13 + 7.4E^{-5} \text{Re}^{2.27} \quad (7.10)$$

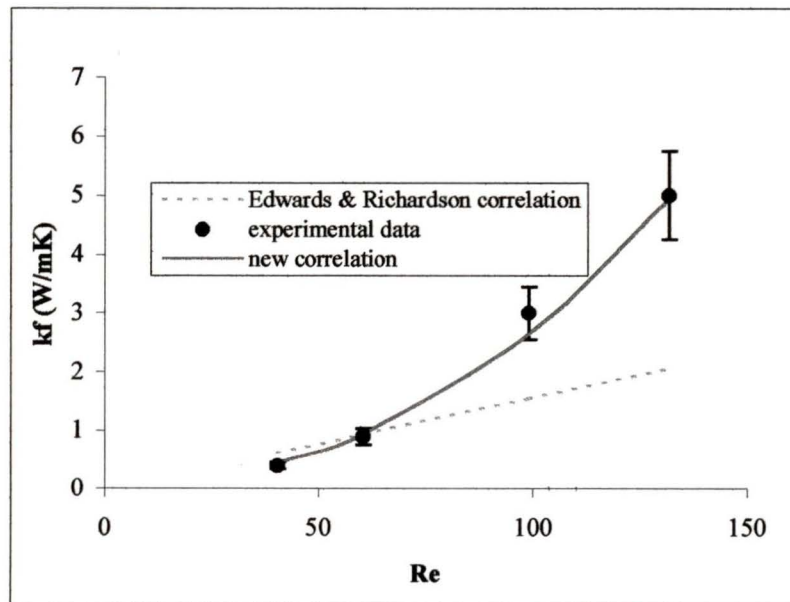


**Figure 7.8: Thermal conduction in the flake bed**

## 7.3 Wire Bed

### 7.3.1 Pressure Drop across the Wire Bed

As was discussed in Section 3.2.1, if the void space between the wires is approximated as an equilateral triangle then according to Kays & London [21] the friction factor can be predicted by:

$$f = \frac{13.33}{Re} \quad (7.11)$$

Figure 7.9 compares the experimental results with this prediction.

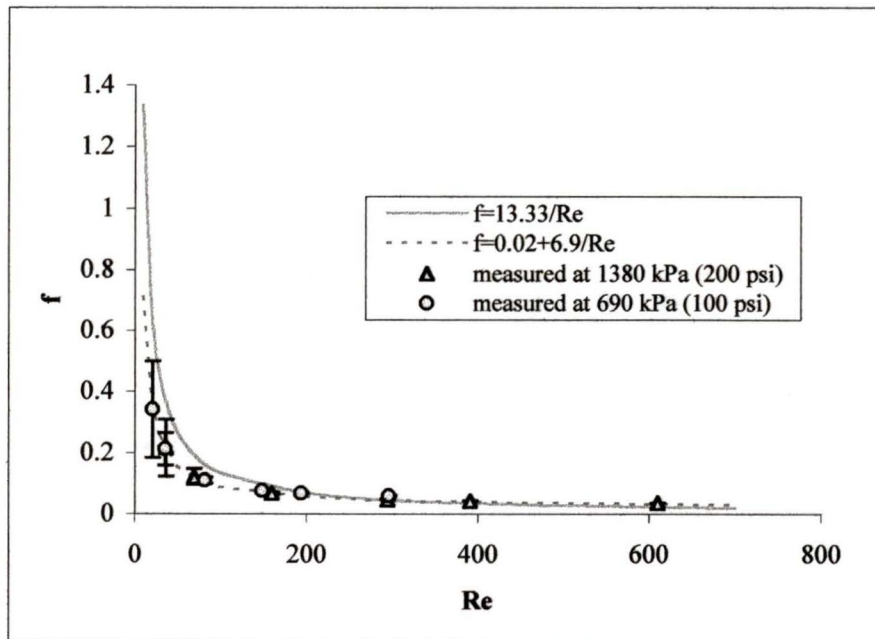


**Figure 7.9: Comparison of theoretical predictions with experimental results for the pressure drop across a bed of wires.**

At high Reynolds numbers, equation (7.11) is a close approximation. However, as the Reynolds number decrease below approximately 200, the fit is no longer close. A better custom approximation was found using Table Curve 2D [67]:

$$f = 0.02 + \frac{6.9}{Re} \quad (7.12)$$

### 7.3.2 Heat Transfer Coefficient in the Wire Bed

As discussed in Section 3.2.2, the heat transfer coefficient in the wire bed is not dependent on the Reynolds number because the flow is well within the laminar region. The predicted heat transfer coefficient is given by:

$$h = \frac{1.892k_f}{D_h} \quad (7.13)$$

The experimental data agrees with the theoretical predictions as is shown in Figure 7.10.

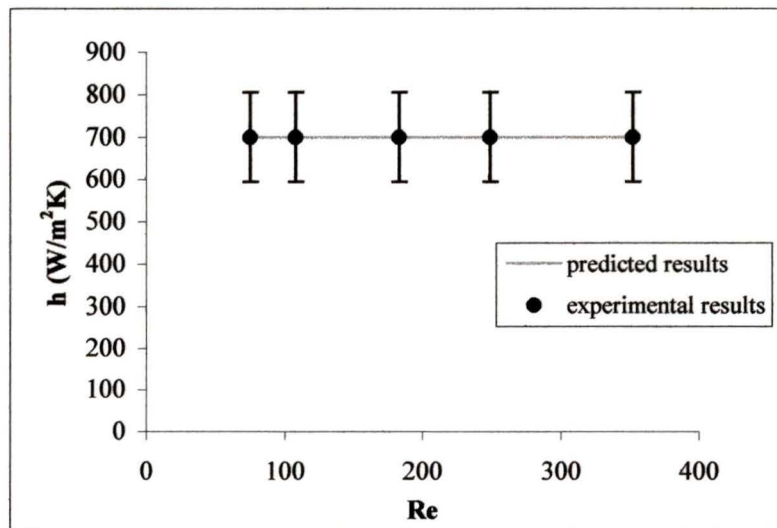


**Figure 7.10: Comparison of theoretical prediction with experimental results for the heat transfer coefficient in a wire bed**

### **7.3.3 Thermal Conductivity of the Wires**

The thermal conductivity through the wires was measured as 13 W/mK. Therefore, since the thermal conductivity of stainless steel is 14.9 W/mK at room temperature, dividing the bed into four sections was not sufficient to significantly reduce the conduction through the bed. To effectively reduce the solid conduction it would be necessary to divide the wires into many thin sections. This would require modifying the manufacturing process. Before being sliced, the wires would need to be made into a monolithic bed to prevent the wires from falling out. This could be done in a number of ways including sintering the wires together, or by adding wax or some other substance that could be removed after completion of the cutting process.

### **7.3.4 Fluid Thermal Conductivity in the Wire Bed**

Because the flow path between the wires is straight, no mixing will occur and therefore eddy diffusivity will not contribute to the fluid thermal conductivity. The thermal conduction in the bed will then be simply the molecular fluid conductivity. For nitrogen this is only 0.026 W/mK and can be neglected. If the wire bed is divided into many small sections than the eddy effects may become more important.

## 7.4 Comparison of the Performance of the Different Geometries

A summary of the experiments conducted for each of the regenerator beds is given in Table 7.1.

**Table 7.1: Summary of Test Results**

Flow rate g/s	$\Delta P$ kPa (psi)	$h$ W/m <sup>2</sup> K	$K_s$ W/mK	$k_f$ W/mK
<b>Stainless Steel Spheres: D=231 <math>\mu</math>m, <math>\alpha=0.345</math></b>				
1.8	3.03 (0.44)	976	0.4	0.41
1.99	3.50 (0.51)	1046	0.4	0.45
3	6.00 (0.87)	1394	0.4	0.68
4.86	11.30 (1.64)	1951	0.4	1.1
6.66	17.86 (2.59)	2442	0.4	1.5
9.86	33.03 (4.79)	3191	0.4	2.2
13.4	58.81 (8.53)	4114	0.4	3.2
<b>Copper Spheres: D=231 <math>\mu</math>m, <math>\alpha=0.345</math></b>				
1.93	4.27 (0.62)	1053	0.4	0.45
3.08	7.24 (1.05)	1464	0.4	0.72
4.87	13.45 (1.95)	1994	0.4	1.14
6.7	22.75 (3.30)	2449	0.4	1.5
9.84	39.16 (5.68)	3149	0.4	2.2
<b>Flakes: H=40 <math>\mu</math>m, L=421 <math>\mu</math>m, W=245 <math>\mu</math>m, <math>\alpha=0.62</math></b>				
2.07	5.93 (0.86)	500	2	0.4
3.1	10.34 (1.50)	650	2	0.9
5.09	21.93 (3.18)	900	2	3.0
6.77	36.82 (5.34)	1100	2	5.0
<b>Wires: D=686 <math>\mu</math>m, <math>\alpha=0.1</math></b>				
2.09	4.83 (0.70)	700	13	0
3	7.93 (1.15)	700	13	0
5.09	16.34 (2.37)	700	13	0
6.9	26.75 (3.88)	700	13	0
9.77	45.50 (6.60)	700	13	0

In Figure 7.11, the pressure drop across the different beds is plotted against the Reynolds number. The flakes have the highest pressure drop, followed by the spheres, with the wires exhibiting the lowest pressure drop.

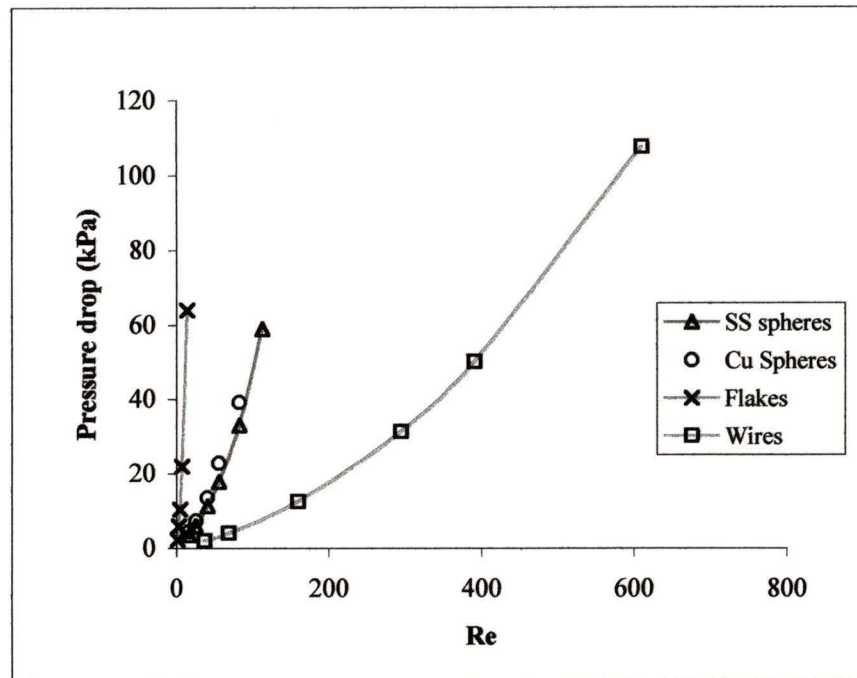


**Figure 7.11: Comparison of the pressure drop across different geometries**

However, this comparison does not give a true indication of the best geometry. It is expected that as the equivalent diameter increases the pressure drop decreases. The wires used in the experiments have a diameter about 2.5 times that of the spheres and would therefore be expected to have a much lower pressure drop. A better indication of the relative performance of the different geometries would be to compare the pressure drop across beds of equal surface area.

An equivalent diameter corresponding to a surface area of  $1.5 \text{ m}^2$  was calculated for each geometry. The equivalent diameters,  $231 \text{ }\mu\text{m}$  for spheres and wires and  $60 \text{ }\mu\text{m}$  for flakes, were then used in equations (7.3), (7.9), and (7.12) to predict the pressure drop. These pressure drops are plotted against the Reynolds number in Figure 7.12. The flake bed still has the largest pressure drop but the wire bed now has a much larger pressure drop than the spheres.

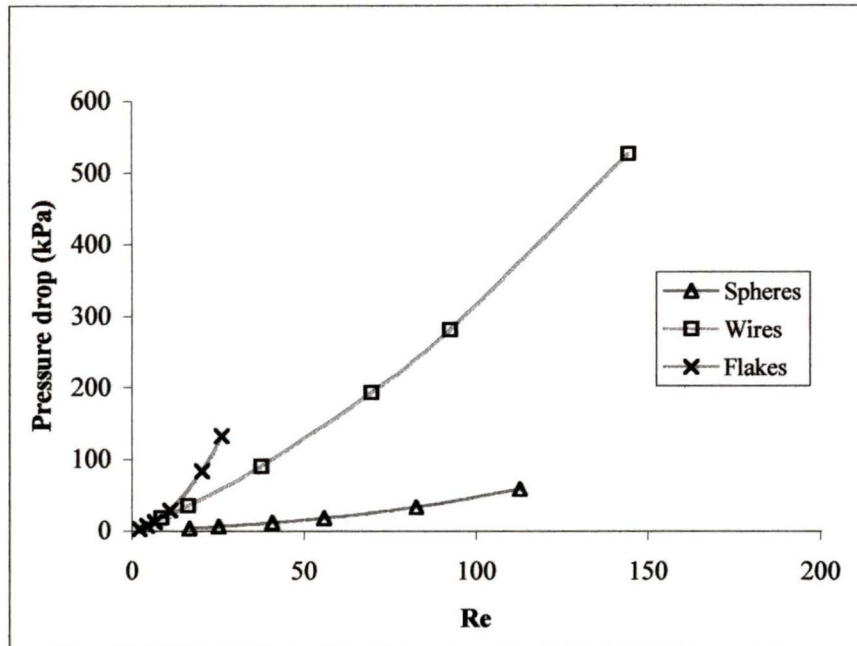


**Figure 7.12: Comparison of the pressure drop across different geometries the surface area set to  $1.5 \text{ m}^2$**

Another factor that affects the pressure drop across the bed is the porosity of the bed. In Figure 7.12, the pressure drop across the wire bed is much larger than that across the sphere bed in part because the wire bed has a very low porosity of about 0.1 compared to 0.355 porosity in the sphere bed. In Figure 7.13, the surface area is still  $1.5 \text{ m}^2$  but now the porosity has been changed to 0.355 in all of the beds. The pressure drops calculated in this manner do not have any practical meaning since it is not easy to vary the porosity in the actual beds. However, it does verify that the correlations behave according to expectations. The pressure drop across the wire bed decreases below that of the sphere bed as would be expected. The pressure drop across the flake bed becomes very large and has been plotted on the secondary axis.

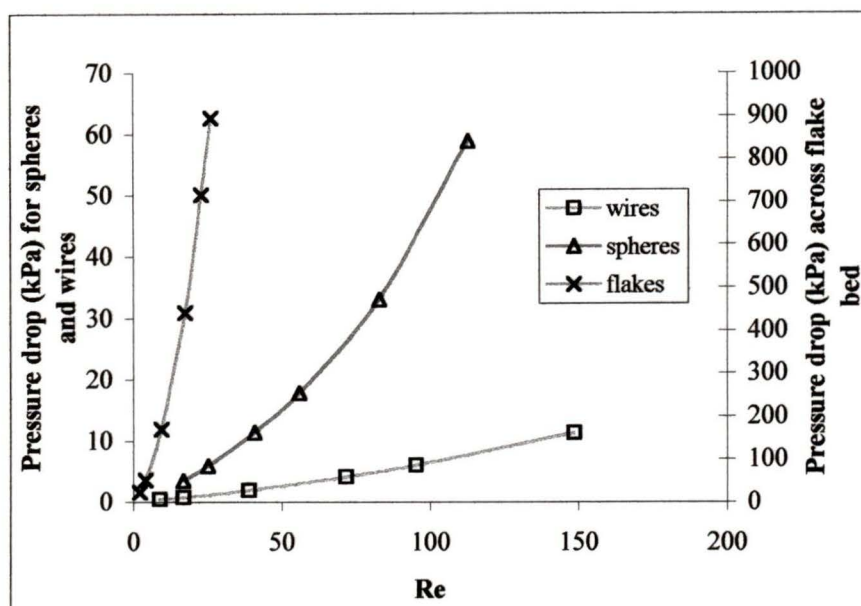


**Figure 7.13: Comparison of the pressure drop across different geometries with a surface area of  $1.5 \text{ m}^2$  and a porosity of 0.355**

The heat transfer coefficients measured in each of the different regenerator beds are compared in Figure 7.14. The heat transfer coefficient is slightly higher in the flake bed than in the spheres. The performance of the wire bed is much lower than the other two except at very low Reynolds numbers.

However, as with the pressure drop, straight comparison of the heat transfer coefficient of the different experiments is not a fair comparison. To get a better indication of how the performance of the different geometries compares, the correlations discussed above were used to predict what values of  $h$  could be expected if all of the geometries had the same surface area. The surface area of the flakes and the wires was set to equal that of the spheres. The results are plotted in Figure 7.15.

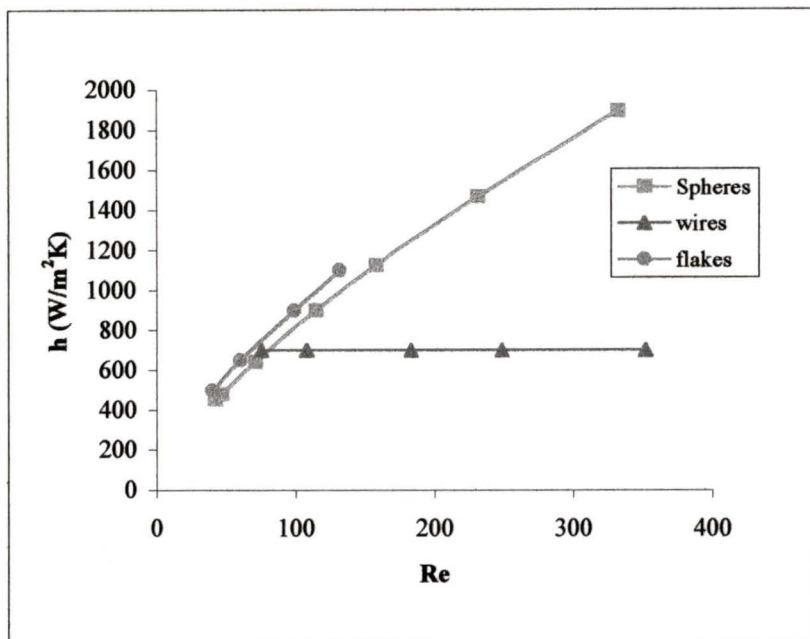


**Figure 7.14: Comparison of the heat transfer coefficient measured in the different geometries**

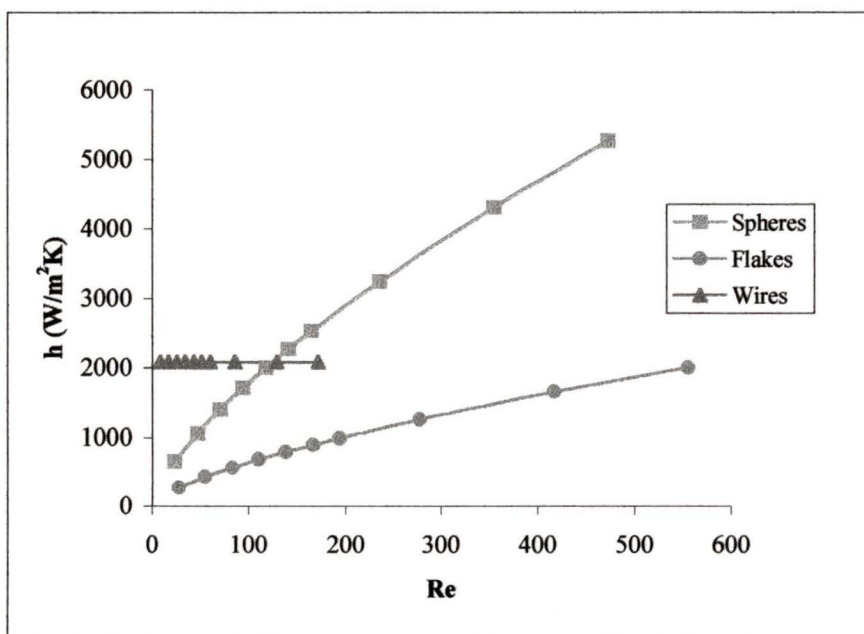


**Figure 7.15: Comparison of the predicted heat transfer coefficient in the different beds with a surface area of 1.5 m<sup>2</sup>.**

In this case, the wires have the highest heat transfer coefficient below a Reynolds number of about 100. The performance of the flake bed is well below that of the sphere bed and will only surpass the performance of the wire bed at very high Reynolds numbers.

The heat transfer coefficient that was predicted for regenerators with a surface area of  $1.5 \text{ m}^2$  was used to calculate the Ntu. The results are plotted in Figure 7.16. The trends are the same as those found in the heat transfer coefficient comparison. At low flow rates, the wire bed has a much higher Ntu than the other two beds. However, it is surpassed by the sphere bed at Reynolds numbers higher than about 35.

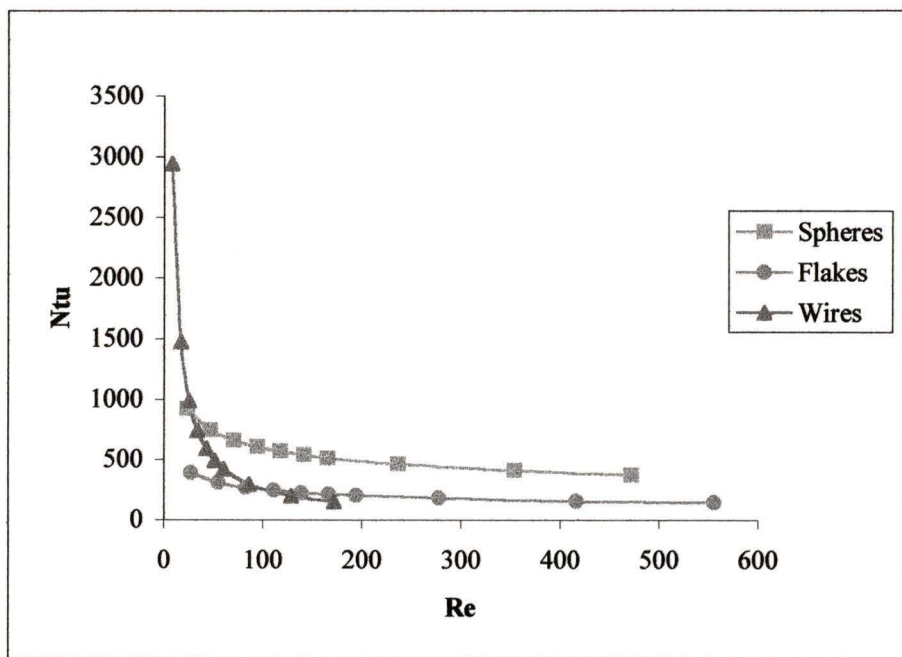


**Figure 7.16: Comparison of the Ntu predicted if all the geometries had a surface area of  $1.5 \text{ m}^2$ .**

The thermal conduction through both the fluid and the solid in the different geometries is compared in Figure 7.17. The solid conduction in the wire bed is much higher than in the other beds. However, as discussed above, this could be reduced with improved manufacturing techniques. The solid conduction in the flake bed is higher than that in the sphere beds because of a contact area much greater than a point. It is also important to

note that for both the sphere and flake beds, the fluid conduction is dominant at high flow rates but becomes less important at low flow rates.

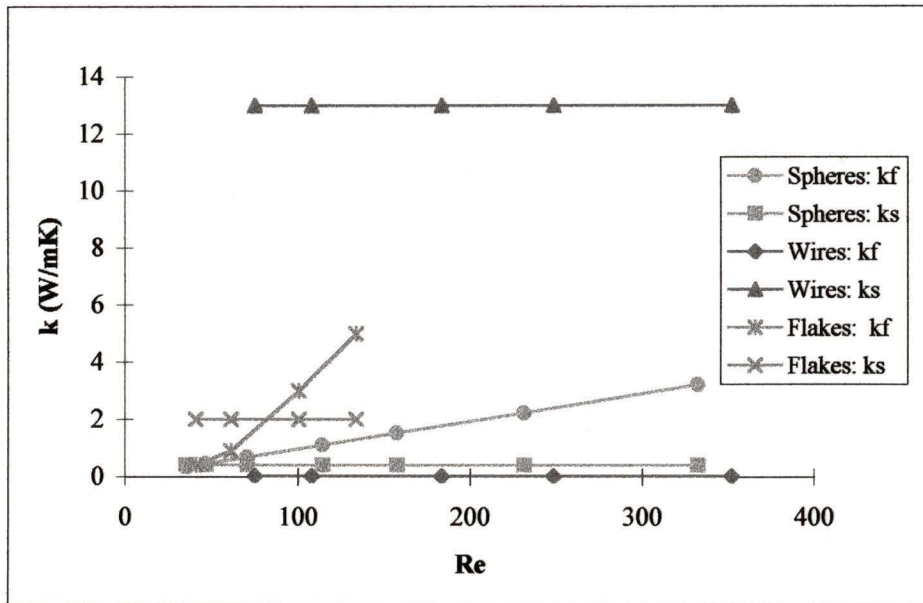


**Figure 7.17: Comparison of the fluid and solid conductivity for the different geometries**

## 8. Conclusions and Recommendations

---

### 8.1 Conclusions

A computer program to simulate regenerator performance was written and validated. It was then used to analyze the experimental data. A test apparatus was designed and built to evaluate regenerators using the differential test method. Three different geometries were formed into regenerator beds and their performance evaluated.

The results from the sphere regenerator bed agreed with the semi-empirical correlations found in the literature and therefore validated the test apparatus. These tests also emphasized the importance of stating explicitly the assumptions made in the development of the correlations. A significant difference in the heat transfer coefficient was observed depending on whether or not the fluid thermal conductivity was accounted for separately.

The performances of the flake and wire regenerator beds were characterized. There are a few references to flake regenerators in the literature but not that include correlations developed specifically for flakes. The wire regenerator bed is a new regenerator geometry that has not previously been tested.

To fairly compare the different geometries, they should have the same surface area. The correlations developed from the experimental data were used to predict the performance in such a case. With equal surface areas, the wires would experience the largest pressure drop across the bed, followed by the flakes and then the spheres. The heat transfer would be better in the wire bed at low Reynolds numbers but would be surpassed by the heat transfer in the sphere bed above a Reynolds number of about 35. The worst heat transfer would be in the flake bed.

For overall performance, there are some cases, especially at low Reynolds numbers, where the wires would be preferred over the spheres. The high thermal mass of the wire bed, due to the very low porosity makes it very desirable for some cryogenic applications where the specific heat drops off at very low temperatures. The flake bed did not perform as well as had been hoped, mostly because they were expected to have a much lower porosity than 60%. Other packing methods should be investigated, including different orientation of the flakes.

In combination, the test apparatus and computer model provide an excellent means for testing various regenerator beds. The apparatus can also be easily altered to test regenerators of different lengths simply by replacing the regenerator housing. The computer model can be used as a powerful tool in designing future regenerator beds as well.

## **8.2 Recommendations**

The following are some recommendations for the direction future work:

- One of the limitations on the test apparatus is that at low flow rates, much more heat is lost to the surroundings and to the container walls than at high flow rates. This means that the assumption that the bed is isolated is invalid. This problem should be addressed by improving the insulation on the exterior of the regenerator housing and perhaps even adding an insulating layer to the inside of the container. Also, a start has been made on improving the computer model to account for these effects but it needs to be improved and validated.
- Further testing should be conducted on the flake regenerator bed. The bed tested in this thesis was constructed so that the flakes were mostly orientated with the

largest face perpendicular to the flow. One would expect the results to be quite different if the flakes were aligned parallel to the flow. It could also be that the optimum orientation is a random one. These different cases should be examined further. Also, smaller flakes should be tested.

- A new wire regenerator bed should be constructed with many smaller sections. This would reduce the conduction down the bed. A new construction technique would be required because it would be imperative to form the wires into a monolithic block before attempting to cut them. This could be accomplished either by sintering the wires together or by filling the holes with wax or some other substance that could be removed after the cutting process. Sintering might be the better option because with a very thin section it may be difficult to keep the wires in place after removal of the wax.
- Another wire regenerator bed should also be built using much smaller diameter wires. At this point it may become desirable to develop a new, less labour intensive means of aligning the wires in the bed.
- It would be advantageous to have the ability to measure the solid thermal conduction in the regenerator bed. However, this is not a simple task because the conduction is very small and because the amount of force applied when packing the particles into the bed will change the contact area between particles and therefore the thermal conductivity in the bed.

## 9. References

---

1. Program Brochure, "Institute for Integrated Energy Systems", University of Victoria, Victoria, BC, (1993).
2. Barclay, J.A., "Cryofuels, Now and in the Future", Plenary Talk CEC/ICMC (1995), Columbus, OH.
3. Corless, A.J., A Thermo-economic Approach to the Integration of Fleet-Sized LNG and CNG Refuelling Systems, M.A.Sc. Thesis, University of Victoria, Victoria, BC, (1995).
4. Barclay, J.A., Goudie, D.W., and Reid, C.E.J., "Comparison of natural gas liquefiers for fleet-size LNG/CNG refuelling systems", Proceedings of the Eleventh Windsor Workshop on Alternative Fuels, Toronto, ON (1995).
5. Barclay, J.A., Corless, A., "Cost Analysis of a Magnetic Liquefier in a Fleet-Sized Cryofuel Refuelling System", Solar Energy Technology, vol. 13, p. 43, (1992).
6. Reid, C.E.J., Development of Magnetic Refrigerants for Active Magnetic Regenerative Refrigerators, M.A.Sc. Thesis, University of Victoria, Victoria, BC, (1995).
7. Spearing, I. A Numerical Model for a Rotary Active Magnetic Regenerative Refrigerator, M.A.Sc. Thesis, University of Victoria, Victoria, BC. (1995).
8. Barron, R.F., Cryogenic Systems, Oxford University Press, New York, p. 272, (1985).
9. Vonk, G., "A New Type of Compact Heat Exchanger with a High Thermal Efficiency", Advances in Cryogenic Engineering, vol. 13, p. 582, (1968).
10. Steyert, W.A., "Heat Transfer and Flow Friction in Fine Porous Media", Los Alamos Report No. LA-6912-MS, (1977).
11. Miyabe, H., Takahashi, S., and Hamaguchi, K. "An Approach to the Design of Stirling Engine Regenerator Matrix using Packs of Wire Gauzes", Proceedings of the 17<sup>th</sup> IECEC, p. 1839, (1982).
12. Fleming, R.B., "A Compact Perforated-Plate Heat Exchanger", Advances in Cryogenic Engineering, vol. 14, p. 197, (1969).

13. Hendricks, J.B., "A New Method for Producing Perforated Plate Recuperators", *Advances in Cryogenic Engineering*, vol. 41, p. 1329, (1996).
14. Lins, R.C., and Elkan, M.A., "Design and Fabrication of Compact, High Effectiveness Cryogenic Heat Exchangers using Wire Mesh Surfaces", *Advances in Cryogenic Engineering*, vol. 20, p. 283, (1975).
15. Ozisik, M.N., Heat Transfer: A Basic Approach, McGraw-Hill, New York, p. 524, (1985).
16. Coppage, J.E., and London, A.L., "The Periodic-Flow Regenerator - A Summary of Design Theory", *Transactions of the ASME*, vol. 75, p. 779, (1953).
17. Barclay, J.A., and Sarangi, S., "Selection of regenerator geometry for magnetic refrigerator applications", *Cryogenic Processes and Equipment*, Proceedings of the Cryogenic Engineering Symposium held in conjunction with the ASME/AICHE Annual Meeting, p. 51-58, (1984).
18. Perry, R.H., Green, D.W., Maloney, J.O., Perry's Chemical Engineering Handbook, McGraw-Hill, New York, (1984).
19. Gamson, B.W., "Heat and Mass Transfer: Fluid Solid Systems", *Chemical Engineering Progress*, p. 19, (January 1951).
20. Heggs, P.J., "Experimental Techniques and Correlations for Heat Exchanger Surfaces: Packed Beds", *Low Reynolds Number Flow Heat Exchangers*, p. 341, Hemisphere Publishing Corp., (1983).
21. Kays, W.M., and London, A.L., Compact Heat Exchangers, McGraw-Hill, New York, (1984).
22. Coppage, J.E., and London, A.L., "Heat Transfer and Flow Friction Characteristics of Porous Media", *Chemical Engineering Progress*, vol. 52, no. 2, p. 57-F, (1956).
23. Handley, D., and Heggs, P.J., "Momentum and Heat Transfer Mechanisms in Regular Shaped Packings", *Transactions of the Institute of Chemical Engineers*, vol. 46, p.T251, (1968).
24. Timmerhaus, K.D., and Flynn, T.M., Cryogenic Process Engineering, Plenum Press, New York, (1989).
25. Schmidt, F.W., and Willmott, A.J., Thermal Energy Storage and Regeneration, Hemisphere Publishing Corporation, New York, (1981).

26. Bird, R.B., Stewart, W.E., and Lightfoot, E.N., Transport Phenomena, John Wiley & Sons, New York, (1960).
27. Ergun, S., "Fluid Flow through Packed Columns", *Chemical Engineering Progress*, vol. 48, p. 89, (1952).
28. Morcom, A.R., "Fluid Flow through Granular Materials", *Transactions of the Institute of Chemical Engineers*, vol. 24, p. 30, (1946).
29. Macdonald, I.F., El-Sayed, M.S., Mow, K., and Dullien, F.A.L., "Flow through Porous Media-the Ergun Equation Revisited", *Industrial and Engineering Chemistry Fundamentals*, vol. 18, no.3, (1979)
30. Appel, H. and Eder, F.X., "Pressure drop in selected porous materials used for thermal regenerators", *Cryogenics*, vol. 20, p. 587, (1980).
31. Martin, J.J., McCabe, W.I., and Monrad, C.C., "Pressure Drop through Stacked Spheres: Effect of Orientation", *Chemical Engineering Progress*, vol. 47, p. 91, (1951).
32. Bahnke, G.D., and Howard, C.P., "The Effect of Longitudinal Heat Conduction on Periodic-Flow Heat Exchanger Performance", *Journal of Engineering for Power*, vol. 86, (April 1964).
33. Kroeger, P.G., "Performance Deterioration in High Effectiveness Heat Exchangers due to Axial Heat Conduction Effects", *Advances in Cryogenic Engineering*, vol. 12, p. 363, (1967).
34. Romie, F.E., "Treatment of Transverse and Longitudinal Heat Conduction in Regenerators", *Journal of Heat Transfer*, vol. 113, p. 247, (Feb 1991).
35. Beveridge, G.S.G., and Haughey, D.P., "Axial Heat Transfer in Packed Beds. Stagnant Beds Between 20 and 750°C", *International Journal of Heat and Mass Transfer*, vol. 14, p. 1093, (1971).
36. Trevisan, O.V., "Transient method for measuring the thermal properties of saturated porous media", *International Journal of Heat and Mass Transfer*, vol. 36, no. 10, p. 2565, (1993).
37. Vortmeyer, D., and Adam, W., "Steady-state measurements and analytical correlations of axial effective thermal conductivities in packed beds at low gas flow rates", *International Journal of Heat and Mass Transfer*, vol. 27, no. 9, p. 1465, (1984).
38. Yagi, S., Kunii, D., and Wakao, N., "Studies on Axial Effective Thermal Conductivities in Packed Beds", *A.I.Ch.E. Journal*, vol. 6, no. 4, p. 543, (1960).

39. Duncan, A.B., Peterson, G.P., and Fletcher, L.S., "Effective Thermal Conductivity within Packed Beds", ASME Publication HTD, vol. 104, pt.3, (1988).
40. Tsotsas, E., and Martin, H., "Thermal Conductivity of Packed Beds: A Review", Chemical Engineering Processes, vol. 22, p. 19-37, (1987).
41. Hsu, C.T., Cheng, P., and Wong, K.W., "Modified Zehner-Schlunder Models for Stagnant Thermal Conductivity of Porous Media", International Journal of Heat and Mass Transfer, vol. 37, no. 17, p. 2751, (1994).
42. Bauer, T.H., "A General Analytical Approach Toward the Thermal Conductivity of Porous Media", International Journal of Heat and Mass Transfer, vol. 36, no. 17, p. 4181-4191, (1993).
43. Sarangi, S., and Baral, H.S., "Effects of Axial Conduction in the Fluid on Cryogenic Regenerator Performance", Cryogenics, vol. 27, p. 505, (Sept. 1987).
44. Edwards, M.F., and Richardson, J.F., "Gas Dispersion in Packed Beds", Chemical Engineering Science, vol. 1968, p. 109, (1968).
45. White, F.M., Fluid Mechanics., McGraw-Hill, p. 331, New York, (1986).
46. Chhatwal, H.L., Goswami, T.R., and Diwakar, R.K., "A Simple Regenerator Test Apparatus for Testing Regenerators for Miniature Cryocoolers", Indian Journal of Pure and Applied Physics, vol. 30, p. 414, (August 1992).
47. Kratschmar, K. The Development of a Cryogenic Regenerator Test Apparatus., M.A.Sc. Thesis, University of Victoria, Victoria BC, (1995).
48. Yaron, R., Shokralla, S., Yuan, J., Bradley, P.E., and Radebaugh, R., "Etched Foil Regenerator", Advances in Cryogenic Engineering, vol. 41, p. 1339, (1996).
49. Loehrke, R.I., "Evaluating the Results of the Single-Blow Transient Heat Exchanger Test", Experimental Thermal and Fluid Science, vol. 3, p. 574, (1990).
50. Oldson, J.C., Knowles, T.R., and Rauch, J., "Pulsed Single-Blow Regenerator Testing", Proceedings of the Intersociety Energy Conversion Conference, vol. 5, p. 5.399, (1992).
51. Stang, J.H., Bush, J.E., and London, A.L., "The Periodic Technique for Testing Compact Heat Exchanger Surfaces", Technical Report no. 67, U.S. Office of Naval Research, Stanford University, (1968).
52. Furnas, C.C., "Heat Transfer from a Gas Stream to a Bed of Broken Solids", Industrial and Engineering Chemistry, vol. 22, no. 7, p. 721, (July 1930).

53. Schumann, T.E.W., "Heat Transfer: A Liquid flowing through a Porous Prism", *Journal of the Franklin Institute*, vol. 208, p. 405, (1929).
54. Pucci, P.F., Howard, C.P., "The Single-Blow Transient Testing Technique for Compact Heat Exchanger Surfaces", *Journal of Engineering for Power*, p. 29, (1967).
55. Kohlmayer, G.F., "Exact Maximum Slopes for Transient matrix Heat Transfer Testing", *International Journal of Heat and Mass Transfer*, vol. 9, p. 671, (1965).
56. Li, Chung-Hsiung, and Shah, R.K., "The Maximum Slope of Single-Blow Transient Testing for Compact Heat Exchanger Surfaces", *Journal of Heat Transfer*, vol. 107, p. 264, (Feb. 1985).
57. Luna, J., Simanjuntak, H., Kim, G., and Frederking, T.H.K., "Modified Regenerator Blow Test: Compact Screen Heat Exchanger Phenomena at Small Flow Rates", *Advances in Cryogenic Engineering*, vol. 37, p. 255, (1992).
58. Rodriguez, J., and Mills, A., "Analysis of the Single-Blow Transient Testing Technique for Perforated Plate Heat Exchangers", *International Journal of Heat and Mass Transfer*, vol. 33, no. 9, p. 1969, (1990).
59. Wiese, J.L., and Bowman, W.J., "Experimental Analysis of Heat Transfer Characteristics and Pressure Drop through Screen Regenerative Heat Exchangers", 8<sup>th</sup> *International Cryocooler Conference*, (1994).
60. Barclay, J.A., Overton, W.C., Stewart, W.F., and Sarangi, S., "Experiment to Determine Properties of Packed Particle Beds and Regenerators at Cryogenic Temperatures", *Advances in Cryogenic Engineering*, vol. 29, p. 605, (1984).
61. Kohlmayer, G.F., "Exact Maximum Slopes for Transient Matrix Heat Transfer Testing", *International Journal of Heat and Mass Transfer*, vol. 9, p. 671, (1966).
62. Elliott, M.P., and Rapley, C.W., "The Effect of Solid Conduction on the 'Single Blow' Experimental Method", 2<sup>nd</sup> *UK National Conference on Heat Transfer*, p. 1623, (Sept. 14-16, 1988).
63. TecPlot, version 6.05, Amtec Engineering Inc., Bellevue, Washington, copyright 1987-1993.
64. Patankar, S.V., Numerical Heat Transfer and Fluid Flow., Hemisphere Publishing Corp., New York, (1980).

65. Press, W.H., Flannery, B.P., Teukolsky, S.A., and Vetterling, W.T., Numerical Recipes: The Art of Scientific Computing (Fortran Version), p. 40, Cambridge University Press, New York, (1989).
66. Omega Temperature Handbook., vol. 28, p. Z-122, (1992).
67. Table Curve 2D, Jandel Scientific Software, AISN Software Inc. (1996).
68. Labview 4.0: Graphical Programming for Instrumentation, National Instruments Corporation (1996).

## Appendix A

# Computer Program to Model Regenerator Thermal Performance

---

This is a copy of the fortran code for the computer model described in Chapter 5.

c	Variable List	
c	a, b, c, const	- coefficients of tri-diagonal matrix
c	acreg	- cross-sectional area of the regenerator
c	ae, aw, ap, apo	- constant for transient profile calculation
c	apart	- surface area of a particle
c	as	- total heat transfer area (surface area)
c	av	- area of void space in wire regenerator
c	bfluid	- constant in transient profile calculation
c	bsolid	- constant in transient profile calculation
c	cond	- material conductivity
c	condf	- fluid conductivity
c	cp	- specific heat of fluid
c	cps	- specific heat of material
c	deq	- equivalent diameter
c	dp	- diameter of particles
c	dreg	- diameter of regenerator
c	etime	- time elapsed
c	flow	- mass flow rate of fluid through regenerator
c	geom	- index to determine which geometry to evaluate
c	h	- heat transfer coefficient
c	htarea	- ratio of surface area of matrix to volume of matrix
c	infile	- user entered input file name

```

c      n          -      number of nodes along regenerator
c      ntu        -      Nusselt number
c      outfile1, outfile2 -      fluid and solid output files respectively
c      poros      -      porosity of regenerator matrix
c      pr         -      Prandtl number of fluid
c      re        -      Reynolds number
c      rho        -      density of fluid
c      rhos       -      density of matrix material
c      rlength    -      regenerator length
c      tf         -      fluid temperature
c      tfo        -      fluid temperature at previous time step
c      timend     -      non-dimensional tim
c      tinit      -      initial fluid and solid temperature
c      tinlet     -      inlet fluid temperature
c      tn         -      temperature values for tri-diag matrix solver
c      ts         -      solid temperature
c      tso        -      solid temperature at previous time step
c      tstep      -      size of time step
c      u          -      velocity of fluid
c      visc       -      viscosity of fluid
c      vpart      -      volume of a particle
c      vreg       -      volume of regenerator
c      x, y, z    -      flake width, length and height respectively
c      xstep      -      size of step in x-direction
c      zonetitle  -      title for output (used in TecPlot)

```

```

c *****

```

```

PROGRAM MAIN

```

```

implicit real*8 (a-h,o-z)

```

```

real*8 ntu

```

```

character*8 infile,outfile1,outfile2

```

```

character*15 zonetitle

```

```

common/blk1/dreg,flow,rho,rhos,cp,cps,visc,pr
common/blk2/poros,re,htarea,h,ntu
common/blk3/dp,vreg,rlength,x,y,z
common/blk4/as,acreg,condf,cond,G,coburnj
common/blk5/xstep,u,bfluid,bsolid,apo,n
common/blk7/etime,timend,tstep,tinlet,tinit,j
common/blk9/tp,geom
common/blk25/infile,outfile1,outfile2,zonetitle

```

c

c prompt for names of input and output files

c

```

print *, 'Enter name of input file'
read *, infile
print *, 'Enter name of output file for fluid data'
read *, outfile1
print *, 'Enter name of output file for solid data'
read *, outfile2
print *, 'Enter title for tecplot zone'
read *, zonetitle

```

c

c read in values from input file

c

```

open (1,file=infile)
read(1,*) geom,dreg,rlength,dp,x,y,z,poros,tinit,tinlet
read(1,*) flow,rho,rhos,cp,cps,visc,pr,condf,cond
read(1,*) tstep,n,h

```

c

c calculate cross-sectional area and volume of regenerator

c

```

pi=3.141592654
acreg=pi/4*dreg**2

```

```

vreg=acreg*rlength
xstep=rlength/n
c
c call subroutine appropriate for regenerator geometry
c
  if (geom .eq. 1) then
    call particle
  elseif (geom .eq. 2) then
    call flake
  elseif (geom .eq. 3) then
    call wires
  endif
c
c call subroutine to calculate temperature profiles
c
  call profile
  end
c
c This subroutine calculates spherical particle regenerator properties
c
  SUBROUTINE PARTICLE
  implicit real*8 (a-h,o-z)
  real*8 ntu
  common/blk1/dreg,flow,rho,rhos,cp,cps,visc,pr
  common/blk2/poros,re,htarea,h,ntu
  common/blk3/dp,vreg,rlength,x,y,z
  common/blk4/as,acreg,condf,cond,G,coburnj
  common/blk5/xstep,u,bfluid,bsolid,apo,n
c
c calculate surface area (m**2)
c

```

```
as=6*(1-poros)*vreg/dp
```

```
c
```

```
c calculate eddy diffusivity/fluid conductivity
```

```
c
```

```
Go=flow/(acreg)
```

```
reo=dp*Go/visc
```

```
if (reo .gt. 2*poros/pr) then
```

```
    condf=Go*cp*dp/(2*poros)
```

```
endif
```

```
c
```

```
c calculate h Denton's correlation (Kay's and London)
```

```
c
```

```
G=flow/(acreg*poros)
```

```
re=dp*G/visc
```

```
if (h .eq. 0) then
```

```
h=(G*cp*.5*(re)**-0.3)/pr**(2.0/3.0)
```

```
endif
```

```
c
```

```
c calculate ntu
```

```
c
```

```
ntu=h*as/(flow*cp)
```

```
return
```

```
end
```

```
c
```

```
c subroutine to calculate flake regenerator properties
```

```
c
```

```
SUBROUTINE FLAKE
```

```
implicit real*8 (a-h,o-z)
```

```
real*8 ntu
```

```

common/blk1/dreg,flow,rho,rhos,cp,cps,visc,pr
common/blk2/poros,re,htarea,h,ntu
common/blk3/dp,vreg,rlength,x,y,z
common/blk4/as,acreg,condf,cond,G,coburnj
common/blk5/xstep,u,bfluid,bsolid,apo,n
common/blk9/tp,geom

```

c

c calculate the total heat transfer area (m\*\*2)

c

```

vpart=x*y*z
apart=2*x*y+2*x*z+2*y*z
htarea=apart/vpart
as=htarea*(1-poros)*vreg

```

c

c guess for heat transfer coefficient using d equivalent

c

```

deq=(x+y)/2
G=flow/(poros*acreg)
re=deq*G/visc
if (h .eq. 0) then
  h=(G*cp*.5*(re*poros)**-0.3)/pr**(2.0/3.0)
endif

```

c

c calculate ntu

c

```

ntu=h*as/(flow*cp)

```

c

c determine eddy diffusivity

c

```

Go=flow/acreg
reo=deq*Go/visc

```

```

if (reo .gt. 2*poros/pr) then
  condF=Go*cp*deq/(2*poros)
endif

return
end

c
c subroutine to calculate wire regenerator properties
c

SUBROUTINE WIRES
implicit real*8 (a-h,o-z)
real*8 ntu,deq,kf
common/blk1/dreg,flow,rho,rhos,cp,cps,visc,pr
common/blk2/poros,re,htarea,h,ntu
common/blk3/dp,vreg,rlength,x,y,z
common/blk4/as,acreg,condF,cond,G,coburnj
common/blk5/xstep,u,bfluid,bsolid,apo,n

c
c calculate the total heat transfer area (m**2)
c

pi=3.141592654
acreg=1.07e-3
vreg=acreg*rlength
av=sqrt(3.)/4.*dp**2-pi/8.*dp**2
deq=4.*av/(0.5*pi*dp)
as=0.5*pi*dp*rlength*poros*acreg/av

c
c heat transfer coefficient correlation
c

kf=0.026
G=flow/(poros*acreg)

```

```

re=G*deq/visc
if (h .eq. 0) then
  h=1.892*kf/deq
endif

c
c calculate ntu
c
  ntu=h*as/(flow*cp)

  return
end

c
c subroutine to calculate transient temp profiles
c
  SUBROUTINE PROFILE
  implicit real*8 (a-h,o-z)
  real*8 ntu
  common/blk1/dreg,flow,rho,rhos,cp,cps,visc,pr
  common/blk2/poros,re,htarea,h,ntu
  common/blk3/dp,vreg,rlength,x,y,z
  common/blk4/as,acreg,condf,cond,G,coburnj
  common/blk5/xstep,u,bfluid,bsolid,apo,n
  common/blk6/tfo(5000),tso(5000),tf(5000),ts(5000),tn(5000)
  common/blk7/etime,timend,tstep,tinlet,tinit,j
  common/blk9/tp,geom

c
c set time and space steps
c
  u=flow/(rho*poros*acreg)
  etime=0.
  timend=0.

```

```
        diff=1000
c
c initialize grid
c
        do 10 i=1,n
            tfo(i)=tinit
            tso(i)=tinit
            tf(i)=tinit
            ts(i)=tinit
        10 continue
c
c set up iteration loop
c
        do while ((diff .gt. 0.1) .or. (etime .lt. 1))
            call fluid
            call solid
c
c check tolerance
c
            diff=abs(tf(1)-tf(n))
c
c increment the elapsed time and write it in non-dimensional form
c
            etime=etime+tstep
            timend=etime*flow*cp/(vreg*(1-poros)*rhos*cps)
c
c store old temperature values
c
        do 40 i=1,n
            tfo(i)=tf(i)
            tso(i)=ts(i)
```

40 continue

call output

c

c write results at final time step to output files

c

j=199

call output

return

end

c

c subroutine solid will calculate the fluid temperature profile

c at individual time steps

c

SUBROUTINE SOLID

implicit real\*8 (a-h,o-z)

real\*8 ntu

common/blk1/dreg,flow,rho,rhos,cp,cps,visc,pr

common/blk2/poros,re,htarea,h,ntu

common/blk3/dp,vreg,rlength,x,y,z

common/blk4/as,acreg,condf,cond,G,coburnj

common/blk5/xstep,u,bfluid,bsolid,apo,n

common/blk6/tfo(5000),tso(5000),tf(5000),ts(5000),tn(5000)

common/blk7/etime,timend,tstep,tinlet,tinit,j

common/blk8/const(5000),a(5000),b(5000),c(5000)

c

c calculate coefficients

c

bsolid=h\*as/(vreg\*(1-poros))

apo=rhos\*cps\*xstep/tstep

```

aw=cond/xstep
ae=cond/xstep
ap=ae+aw+apo+bsolid*xstep

if (cond .eq. 0) then
  do 5 i=1,n
    ts(i)=(bsolid*xstep*tf(i)+apo*tso(i))/(apo+bsolid*xstep)
5   continue
return
endif

const(1)=bsolid*tf(1)*xstep/2.0+apo/2.0*tso(1)
&      +h*tinlet
b(1)=ae+apo/2.0+bsolid*xstep/2.0+h
c(1)=-ae
do 10 i=2,n-1
  a(i)=-aw
  b(i)=ap
  c(i)=-ae
  const(i)=bsolid*tf(i)*xstep+apo*tso(i)
10  continue
const(n)=bsolid*tf(n)*xstep/2.0+apo/2.0*tso(n)+h*tf(n)
a(n)=-aw
b(n)=aw+apo/2.0+bsolid*xstep/2.0+h
c
c call subroutine to solve the tri-diagonal matrix
c
  call tdm
c
c transfer data from tri-diagonal matrix solver to solid temps
c

```

```

do 30 i=1,n
  ts(i)=tn(i)
30 continue

return
end

c
c subroutine fluid will calculate the fluid temperature profile
c at individual time steps
c
SUBROUTINE FLUID
implicit real*8 (a-h,o-z)
real*8 ntu
common/blk1/dreg,flow,rho,rhos,cp,cps,visc,pr
common/blk2/poros,re,htarea,h,ntu
common/blk3/dp,vreg,rlength,x,y,z
common/blk4/as,acreg,condf,cond,G,coburnj
common/blk5/xstep,u,bfluid,bsolid,apo,n
common/blk6/tfo(5000),tso(5000),tf(5000),ts(5000),tn(5000)
common/blk7/etime,timend,tstep,tinlet,tinit,j
common/blk8/const(5000),a(5000),b(5000),c(5000)

c
c use upwind scheme to solve diffusion
c determine coefficients for matrix
c
bfluid=h*as/(vreg*poros*cp)
aw=condf/(cp*xstep)+rho*u
ae=condf/(cp*xstep)
ap=ae+aw+bfluid*xstep

if (condf .eq. 0) then

```

```

    tf(1)=(aw*tinlet+bfluid*xstep*ts(1))/ap
    do 5 i=2,n
        tf(i)=(aw*tf(i-1)+bfluid*xstep*ts(i))/ap
5    continue
    return
endif

const(1)=aw*tinlet+bfluid*ts(1)*xstep
b(1)=ap
c(1)=-ae
do 10 i=2,n-1
    a(i)=-aw
    b(i)=ap
    c(i)=-ae
    const(i)=bfluid*ts(i)*xstep
10 continue
const(n)=bfluid*ts(n)*xstep
a(n)=-aw
b(n)=aw+bfluid*xstep

c
c call subroutine to solve tri-diagonal matrix
c
    call tdm
c
c transfer data from tri-diagonal matrix solver to fluid temps
c
    do 20 i=1,n
        tf(i)=tn(i)
20 continue

return

```

```

        end

c
c subroutine tdm uses a tridiagonal matrix solver to solve
c for temperature arrays imported from other subroutines.
c
        SUBROUTINE TDM

        implicit real*8 (a-h,o-z)
        common/blk5/xstep,u,bfluid,bsolid,apo,n
        common/blk6/tfo(5000),tso(5000),tf(5000),ts(5000),tn(5000)
        common/blk8/const(5000),a(5000),b(5000),c(5000)
        dimension gam(5000)

c
c begin matrix solving (tridiagonal matrix solver from Numerical
c Recipes)
c
        bet=b(1)
        tn(1)=const(1)/bet
        do 10 i=2,n
            gam(i)=c(i-1)/bet
            bet=b(i)-a(i)*gam(i)
            tn(i)=(const(i)-a(i)*tn(i-1))/bet
10      continue
        do 20 i=n-1,1,-1
            tn(i)=tn(i)-gam(i+1)*tn(i+1)
20      continue
        return
        end

c
c subroutine output will write the data to files
c

```

## SUBROUTINE OUTPUT

```
implicit real*8 (a-h,o-z)
```

```
real*8 ntu
```

```
character*8 infile,outfile1,outfile2
```

```
character*15 zonetitle
```

```
common/blk1/dreg,flow,rho,rhos,cp,cps,visc,pr
```

```
common/blk2/poros,re,htarea,h,ntu
```

```
common/blk3/dp,vreg,rlength,x,y,z
```

```
common/blk4/as,acreg,condf,cond,G,coburnj
```

```
common/blk5/xstep,u,bfluid,bsolid,apo,n
```

```
common/blk6/tfo(5000),tso(5000),tf(5000),ts(5000),tn(5000)
```

```
common/blk7/etime,timend,tstep,tinlet,tinit,j
```

```
common/blk9/tp,geom
```

```
common/blk25/infile,outfile1,outfile2,zonetitle
```

```
open(1,file=outfile1,access='append')
```

```
open(2,file=outfile2,access='append')
```

```
c
```

```
c set up file for use in tecplot and write results from first time step
```

```
c
```

```
if (etime .eq. tstep) then
```

```
  write(1,40) dp,flow,as,h,ntu,condf,cond
```

```
  write(2,40) dp,flow,as,h,ntu,condf,cond
```

```
  write(1,50)
```

```
  write(2,50)
```

```
  write(1,60) zonetitle
```

```
  write(2,60) zonetitle
```

```
40  format('TITLE ="', dp',e7.2,' flow',e7.2,' as',f5.2,' h',f7.2,
```

```
&      ' ntu',f9.2,' kf',e7.2,' ke',f5.2,'"')
```

```
50  format('VARIABLES ="Etime","1/4","1/2","3/4","ColdEnd"')
```

```
60  format('ZONE T=',a15,'"')
```

```
write(1,100) etime,tf(1),tf(0.25*n),tf(0.5*n),tf(0.75*n),tf(n)
write(2,100) etime, ts(1),ts(0.25*n),ts(0.5*n),ts(0.75*n),ts(n)
end if
```

c

c write profile results after every 200 time steps

c

```
if (j .eq. 1999) then
  write(1,100)etime,tf(1),tf(0.25*n),tf(0.5*n),tf(0.75*n),tf(n)
  write(2,100) etime, ts(1),ts(0.25*n),ts(0.5*n),ts(0.75*n),ts(n)
  j=-1
endif
```

```
j=j+1
```

```
100 format(f9.3,1x,4f13.9)
```

```
return
```

```
end
```

VITA

Surname: Caudle

Given Names: Kimberley Jane

Place of Birth: Stouffville, Ontario, Canada

Educational Institutions Attended:

University of Victoria

1994-1997

Queen's University

1990-1994

Degrees Awarded:

B.Sc. (Honours)

Queen's University

1994

## PARTIAL COPYRIGHT LICENSE

I hereby grant the right to lend my thesis to users of the University of Victoria library, and to make single copies only for such users or in response to a request from the Library of any other university, or similar institution, on its behalf or for one of its users. I further agree that permission for extensive copying of this thesis for scholarly purposes may be granted by me or a member of the University designated by me. It is understood that copying or publication of this thesis for financial gain shall not be allowed without my written permission.

Title of Thesis:

Characterization of Regenerator Geometries through Modeling and Experimentation

Author



Kimberley Jane Caudle

July 22, 1997.